7 Tropical Weather on Time Scales of Days to Months

7.1 Introduction

Compared to the weather in middle and high latitudes, tropical weather on subseasonal time scales is subtler and has so far proven less predictable. We have already seen, in Chapter 5, that the Indian monsoon exhibits striking variability on times scales on the order of 10 days, with active and break cycles associated with profound changes in rainfall and wind. In this chapter we will explore observations of tropical weather variability on time scales of days to months and review what is currently known about the mechanisms involved. We begin with an exploration of weather associated with a rich spectrum of equatorially trapped disturbances and end with an exposition of African easterly waves, which are sometimes associated with North Atlantic tropical cyclones.

7.2 Disturbances of the equatorial waveguide

In much of the equatorial region, rain showers can occur at any time of day and year. Nevertheless, the probabilities of rain are modulated by a fascinating variety of disturbances with time scales ranging from a few days to a few months. While much of this modulation can be characterized as random noise with a red spectrum in space and time, some of it appears to be an excitation of equatorial waves of the kind we discussed in connection with ENSO ocean dynamics, and yet some of it, while clearly organized, is not part of the Matsuno spectrum of neutral linear modes.

Figure 7.1 displays two time-longitude sections (often referred to as Hovmöller[1] plots) of satellite-derived precipitation and outgoing longwave radiation for the first five months of 2005. The horizontal axis of these plots spans the equatorial Pacific. In the precipitation plot (left panel), the eye naturally picks out crisscrossing diagonal lines, and the phases speeds corresponding to two of these sets of lines are indicated. There is a prominent set of disturbances traveling eastward at about 12 ms^{-1}, and another traveling west at around 4 ms^{-1}. The latter may simply be disturbances drifting west with the trade winds. But other sets are discernible, including disturbances propagating westward much faster. The sharp transition at around 97^{o} longitude marks the western boundary of the chain of islands that constitute Indonesia, showing the strong effect of land-sea contrasts on convective precipitation.

Curiously, the OLR plot (right panel of Figure 7.1), though it is for exactly the same period of time and span of longitude, shows somewhat different patterns, including a broad envelope (marked by an ellipse in the figure) traveling east, against the trade winds, at about 4 ms^{-1}. Some of the faster eastward moving disturbances we saw in the precipitation fields are also evident in the OLR.

[1] Named after the Danish meteorologist Ernest Hovmöller, who introduced them in 1949

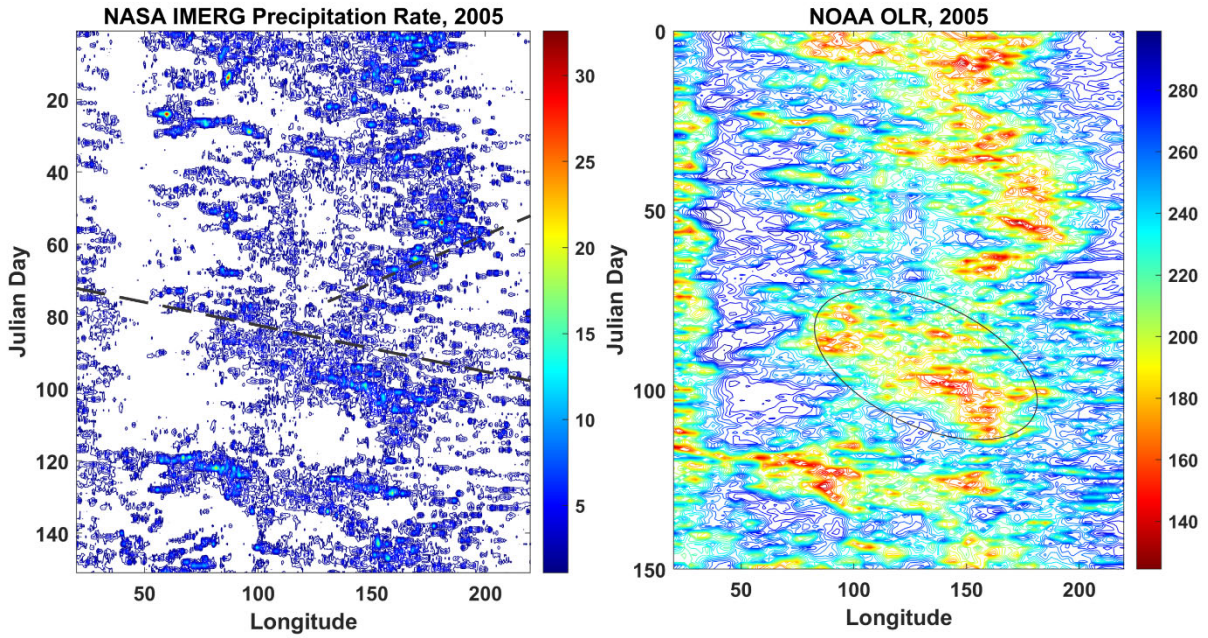

Figure 7.1: Hovmöller diagrams spanning the period January 1 – May 31, 2005 (vertical axis) and longitudes from 20°E to 220°E (horizontal axis). Left: Precipitation with longitudinal resolution of 0.1 degree; right: Outgoing Longwave Radiation (OLR) with horizontal resolution of 2.5 degrees. Both data sets have a temporal resolution of 1 day. In the left panel, the upper and lower dashed lines have slopes of -5 ms^{-1} and 10 ms^{-1}, respectively, and in the right panel the ellipse has a slope of 4 ms^{-1}

An observer on the equator at 50° east longitude would experience some rain nearly every day, but greatly enhanced rain every third or fourth day associated with the fast, eastward-propagating disturbances. Note also that there is much more rain after about day 70 (mid-March) than before.

The variability evident in Hovmöller plots such as those shown in Figure 7.1 can be further quantified by spectral decomposition of the fields, as pioneered by Hayashi (1982) and further refined by Wheeler and Kiladis (1999, 2020). The first step in their procedure is to take a long record of observations, typically satellite-derived OLR or brightness temperature, and remove the first three annual harmonics at each grid point. They then break the record into segments of 96 days each, with this time scale being approximately the largest period oscillation they expect to find in the de-seasonalized series. Then, for each segment, the time series is detrended and the field ϕ is divided into equatorially symmetric and anti-symmetric parts:

$$\phi_{sym} = \frac{1}{2}\left(\phi(\theta)+\phi(-\theta)\right),$$
$$\phi_{antisym} = \frac{1}{2}\left(\phi(\theta)-\phi(-\theta)\right), \tag{7.1}$$

where θ is the latitude. For each component, a fast Fourier transform is applied in the time and longitude dimensions at each latitude, and the resulting spectral power is summed over a band of latitude centered at the equator and averaged over all the 96-day segments of the record.

Figure 7.2 shows the base-10 logarithm of the average of the symmetric and anti-symmetric spectral power (which, from (7.1), is just half the total spectral power) of the Cloud Archive User Data Service (CLAUS) record of brightness temperature (10.5-12.5-micron radiances) from a collection of operational meteorological satellites, from 1984 to 2008. These have been averaged from 15°S to 15°N latitude.

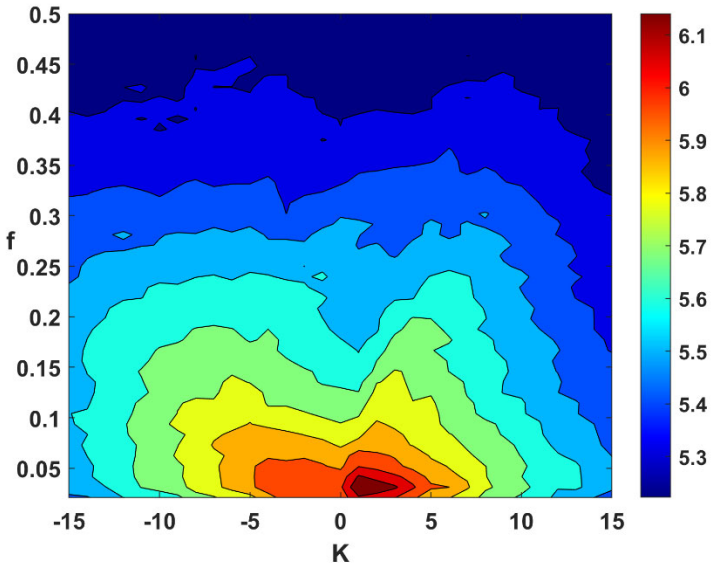

Figure 7.2: Base 10 logarithm of the spectral power of 10.5-12.5-micron radiances from CLAUS data over the period 1984-2008. This is the mean of the symmetric and anti-symmetric components, which is in turn ½ of the total power. The power has been summed over all latitudes between 20°S and 20°N in the data set. The frequency, on the y-axis, is in cycles per day.

The concentration of spectral power at low frequencies and wavenumbers is evident, as are significant departures from a simple red noise spectrum, some of which seem to loosely follow the Matsuno dispersion curves described in Chapter 6. Note in particular the concentration of very low frequency spectral energy in low zonal wavenumber eastward-propagating disturbances.

We might hypothesize that this power spectrum in wavenumber-frequency space is the sum of some kind of red noise that is random in space and time, and regular oscillations propagating along the equator. Wheeler and Kiladis (1999) estimated the background noise spectrum by smoothing the raw total power spectrum (that includes both symmetric and anti-symmetric components) by applying several times in succession a simple 1-2-1 smoother in wavenumber and frequency. Here we depart from that method and define the background noise as that part of the total power spectrum that projects roughly equally onto symmetric and anti-symmetric variability; that is, we will regard the background as ½ the total power spectral density, as illustrated in Figure 7.2. Then the spectral power representing the symmetric and antisymmetric variability is obtained by subtracting this background from, respectively, the symmetric and anti-

symmetric power spectra, and setting to zero any negative values that result. The result of applying this procedure to the CLAUS data is illustrated in Figure 7.3.

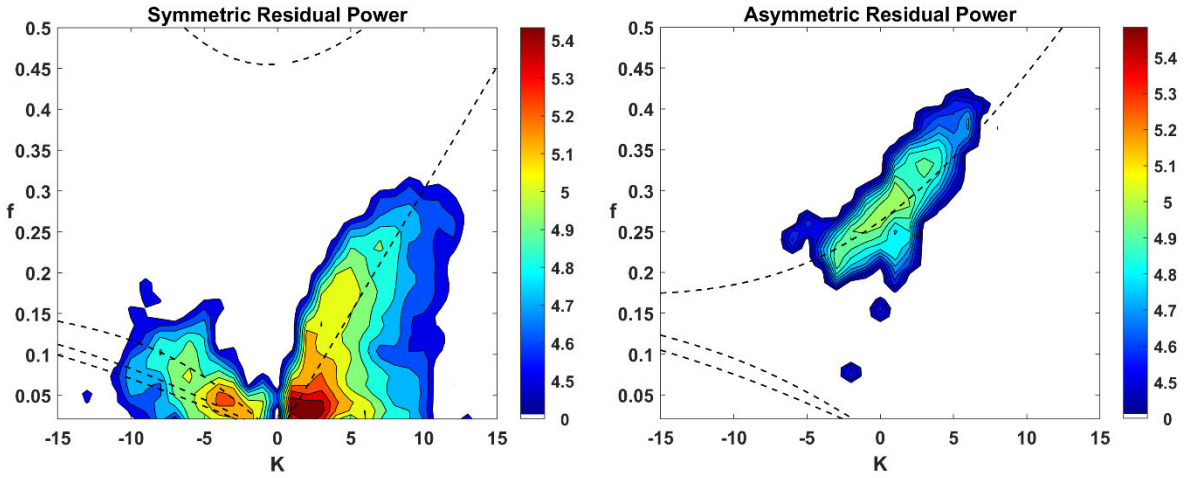

Figure 7.3: Base 10 logarithm of the residual power of the symmetric (left) and anti-symmetric components of the CLAUS brightness temperature record. Fields have been smoothed by applying a 1-2-1 filter 7 times in wavenumber only. Contours are omitted for values less than 4.4. The dashed lines show the Matsuno dispersion curves for n= -1 to +5 assuming a shallow water phase speed of 16 ms^{-1}, with all curves Doppler shifted assuming a background easterly wind of 2 ms^{-1}.

To deal with the strict quantization of the data in wavenumber and frequency, we have applied a 1-2-1 filter seven times, in wavenumber only. Figure 7.3 also shows the Matsuno dispersion relations, taking $c = 16\ ms^{-1}$ and Doppler shifting the curves assuming a background easterly wind of $2\ ms^{-1}$.

The most prominent signal in the symmetric part of the residual spectrum is the MJO, seen here as a spectral peak centered at the (quantized) frequency of one cycle per 48 days and extending from eastward zonal wavenumber 1 to 3[2]. The residual spectral power also extends along Kelvin wave dispersion lines. There is also quite a bit of energy along the n=1,3, and 5 equatorial Rossby wave curves, especially around westward zonal wavenumber 4 and (quantized) frequency of once in 24 days.

The only prominent signal in the anti-symmetric residual power spectrum corresponds to the dispersion curve of a mixed Rossby-gravity mode, with most of the activity in zonal wavenumber between -4 and 8.

Given the signals evident in the left panels of Figure 7.3, one can begin to examine the particular characteristics of variability in different sectors of wavenumber-frequency space by filtering within those sectors and regressing other fields, such as winds and temperatures from reanalyses against the filtered fields. An example of this is presented in Figure 7.4, which starts with a similar wavenumber-frequency decomposition of the same brightness temperature data as used to construct Figure 7.3 except that the background has been defined by smoothing the total power in wavenumber-frequency space, following Wheeler and Kiladis (1999). We use this

[2] Take care to remember that the zonal wavenumber is quantized in integers and the frequency in integer multiples of once in 96 days. The applied smoothing and contouring routine smooth out this quantization in the graphs.

figure to defines sectors corresponding to the most prominent modes of variability and proceed to examine the characteristics of equatorial variability in many of these sectors.

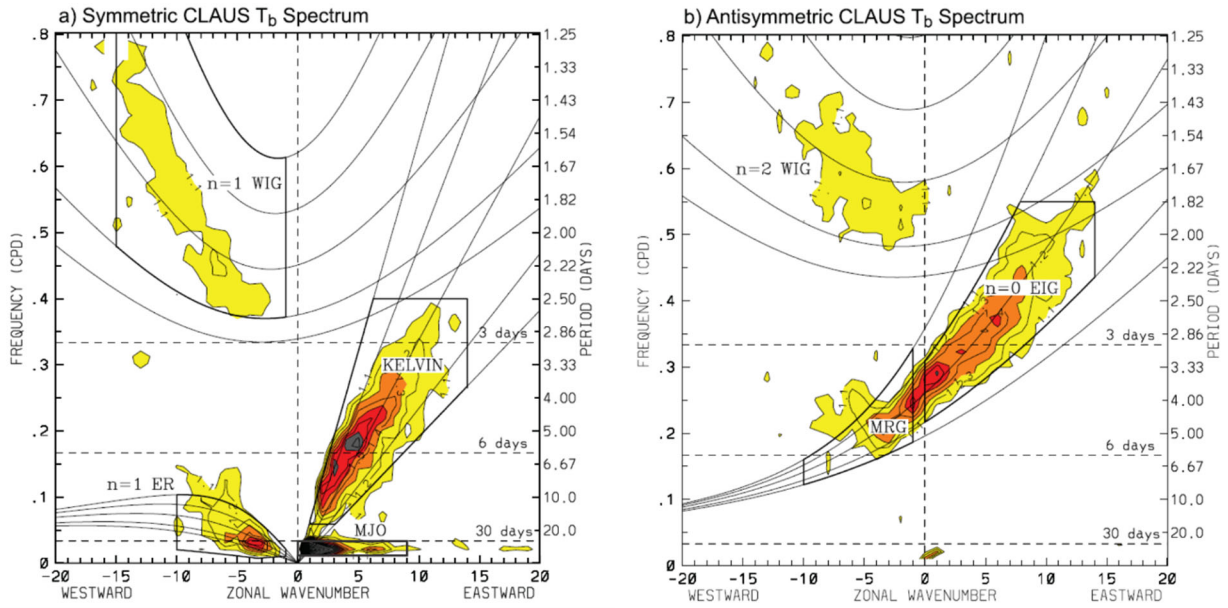

Figure 7.4: Similar to Figure 7.3 (right panels) but showing sectors used in wavenumber-frequency filtering. For this plot, the background spectrum has been created by smoothing the total (symmetric plus anti-symmetric) power, as in Wheeler and Kiladis (1999).

7.2.1: The Madden-Julian Oscillation

In terms of spectral power of many variables, including outgoing longwave radiation, the Madden-Julian Oscillation ("MJO") is the most prominent mode of subseasonal variability in he tropics. It was first discovered by Roland Madden and Paul Julian (Madden and Julian 1971, 1972) in their examination of zonal winds and surface pressure in time series of near-equatorial rawindsonde data. The variability consists disturbances dominated by wavenumber 1 traveling eastward, with peak amplitudes near the equator. In fields related to deep convection, such as OLR and precipitation, the MJO is seen to develop in the western equatorial Indian Ocean and move eastward, reaching maximum amplitude near or just east of Indonesia, and then decaying eastward, losing coherence near the dateline. However, the MJO can often be traced around the globe in near-tropopause variables such as zonal wind and velocity potential. A sketch of the structure of the MJO is shown in Figure 7.5.

The composite structure of an MJO event does not resemble that of any of the classical Matsuno modes, nor does its frequency dependence on wavenumber fall along any of the Matsuno dispersion curves (see Figure 7.4). Figure 7.6 shows a composite of the MJO structure made by regressing MJO frequency- and wavenumber-filtered fields over the period 1979-1989 onto OLR at 0ºN and 125ºE. The fields are OLR itself, 200 hPa winds from operational analyses, and satellite microwave sounding unit channel 2 temperature (MSUT). The regressions are performed using fields lagged with the respect to the OLR at time 0.

A similar regression analysis is shown in Figure 7.7, but also includes fields at 850 hPa.

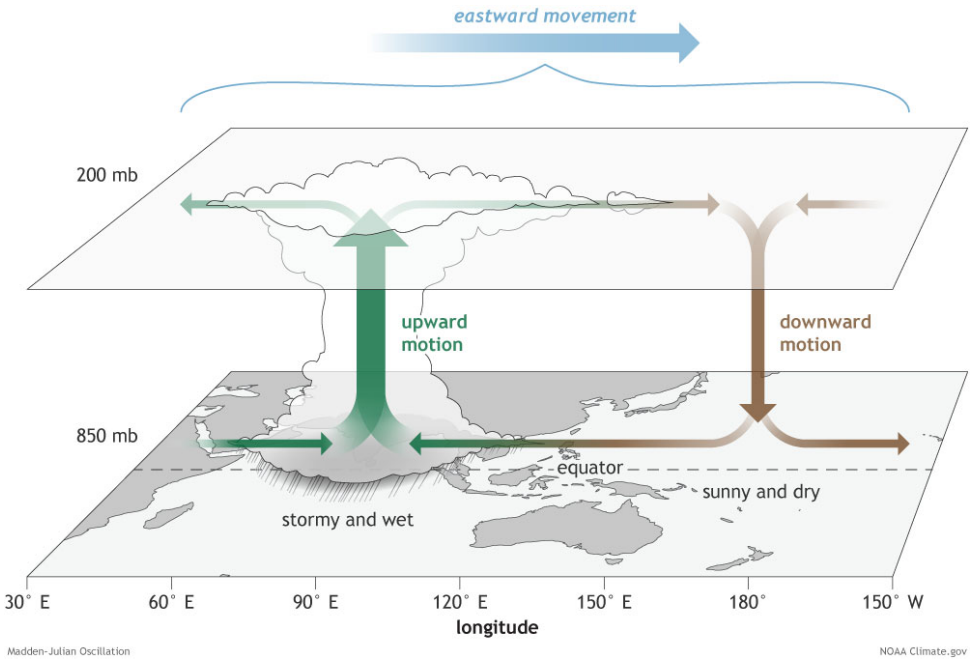

Figure 7.5: Sketch of the vertical circulation, zonal winds, and convection associated with the Madden-Julian Oscillation, at a time when the maximum ascent and rainfall is over the Indian Ocean. The horizontal winds shown are perturbations from the long-term mean. The MJO moves eastward with a period of 30-60 days.

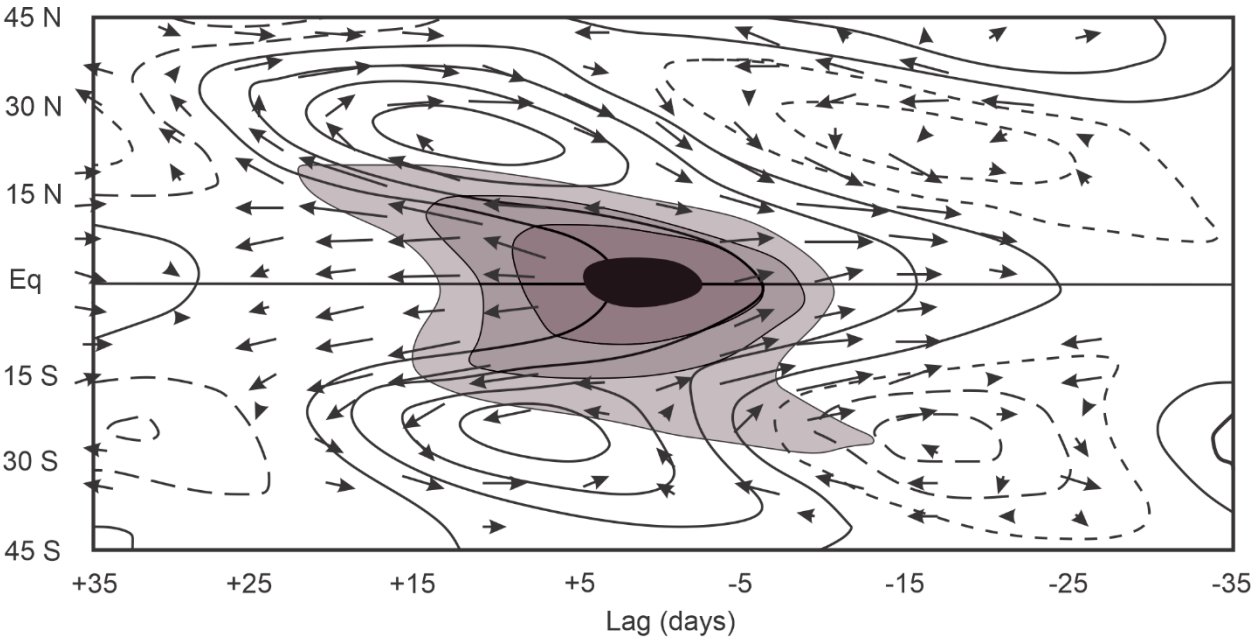

Figure 7.6: Various fields bandpass filtered for eastward-propagating zonal wavenumber 3 and periods of 35-95 days and linearly regressed onto OLR at 0ºN and 125ºE with the time lags indicated on the abscissa: OLR (shading), 200 hPa winds from operational analyses (arrows), and satellite microwave sounding unit channel 2 temperature (MSUT)

(black solid and dashed contours). The maximum wind speed is $2.7\ ms^{-1}$ *and the temperature contour interval is 0.05 K. Data from 1979-1989.*

The pattern in Figures 7.6 and 7.7 more nearly resembles the Gill pattern shown in Figure 6.11 than it does any of the Matsuo modes, as though it were a response to an imposed sea surface temperature anomaly. The MJO ascent region, more or less coinciding with low values of OLR, is preceded by surface easterlies and upper tropospheric westerlies, an enhancement of the background Walker circulation. Cyclonic gyres are found behind (west of) and poleward of the OLR minimum at low levels, with corresponding anticyclones in the upper troposphere. At upper levels there are also prominent cyclonic gyres straddling the equator to the east of the OLR minimum. In Figure 7.6 once can see a kind of chevron-shaped upper tropospheric temperature pattern, with a maximum along the equator just east of the OLR minimum and maxima in the anticyclonic gyres poleward and westward of the OLR minimum.

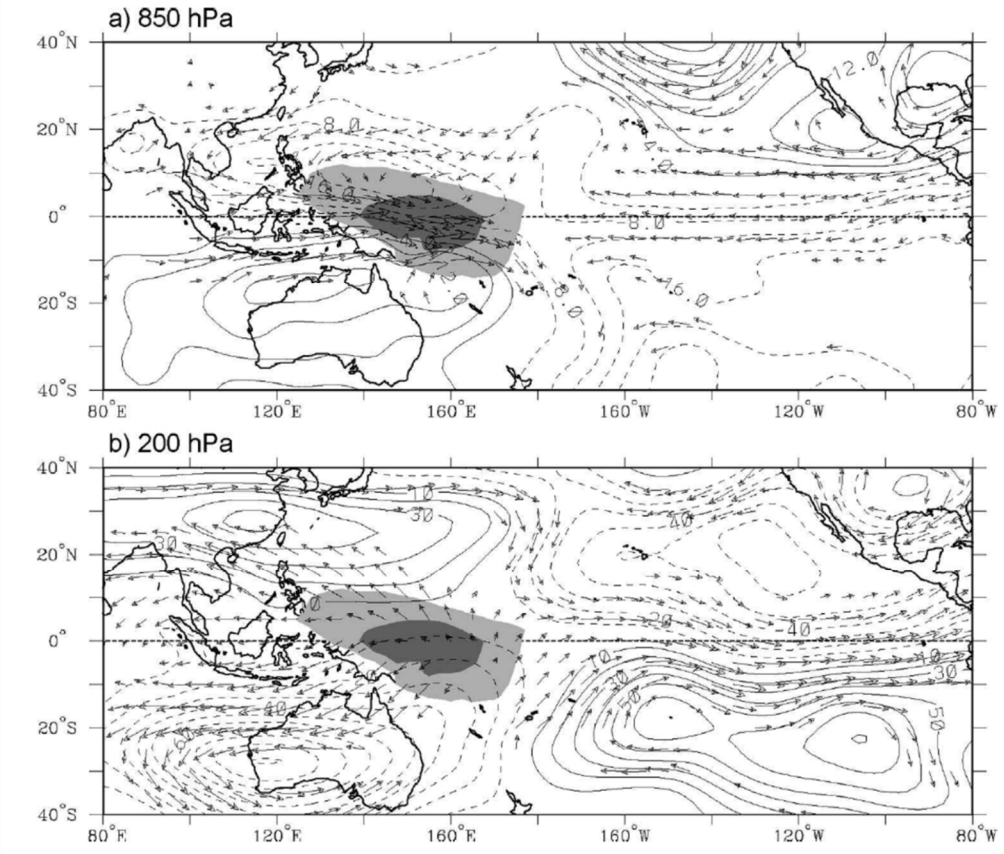

Figure 7.7: Anomalous outgoing longwave radiation (OLR; shading) and anomalous winds from the European Center for Medium Range Weather Forecasts 15-year reanalysis (ERA-15, arrows) regressed against OLR at the equator and 155ºE at 850 hPa (top) and 200 hPa (bottom). Contours show streamfunction. Largest wind in top panel is about 2 ms^{-1} and about 5 ms^{-1} in bottom panel.

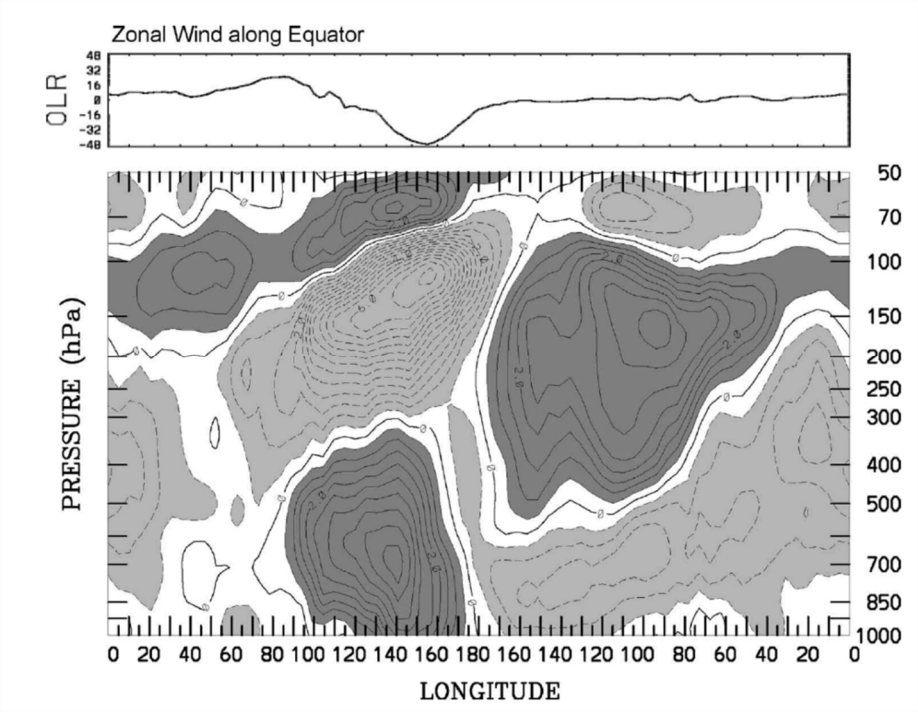

Figure 7.8: As in Figure 7.7 but showing the vertical structure of zonal winds regressed against OLR at the equator and 155ºE. Contour interval is 0.5 ms^{-1} and the associated OLR along the equator is shown in the top panel.

The vertical structure of zonal winds associated with the MJO is evident in Figure 7.8. To a first approximation, winds in the troposphere show first mode baroclinic structure, with opposite signs in the lower and upper troposphere. There is some indication also of a lower stratospheric response of the opposite sign as the upper troposphere.

The MJO has a strong annual cycle, at least as measured by outgoing longwave radiation. Figure 7.9 shows the annual cycle of the OLR variance filtered for eastward propagating zonal wavenumbers 1-3 and periods of 35-95 days. The variance peaks in late boreal winter to early boreal spring in the southern hemisphere, and shows a minimum in mid boreal summer in the northern hemisphere. Note that the ITCZ latitude globally averaged varies in a similar way.

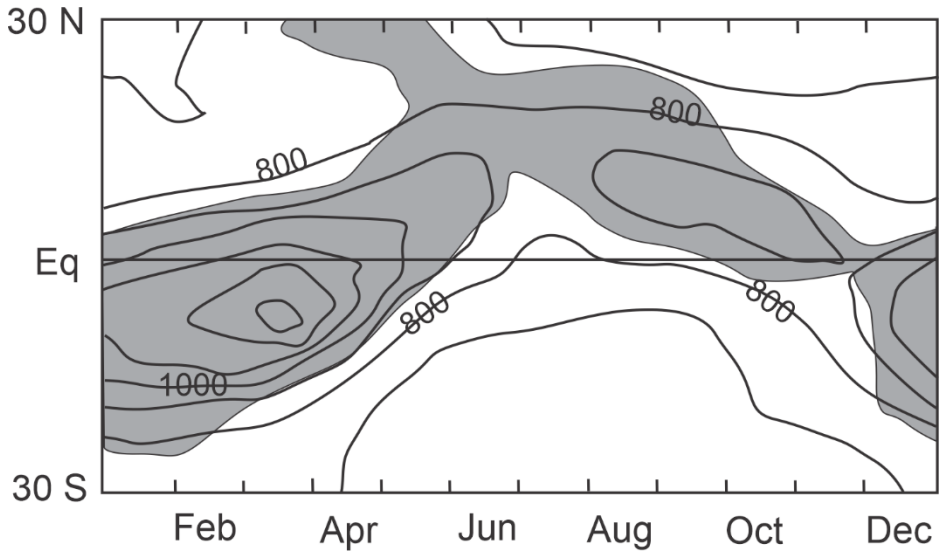

Figure 7.9: Outgoing longwave radiation spectral power (variance) in eastward-propagating wavenumbers 1-3 and periods of 35-95 days (open contours) with statistical significance greater than 95% shaded.

7.2.2: Convectively coupled equatorial waves

Some idea of the structure of the non-MJO equatorial disturbances whose variance seems to follow the classical Matsuno dispersion curves (figure 7.4) can be gleaned by regressing radiosonde- and reanalysis-derived variables against satellite brightness temperature filtered in the wavenumber-frequency domain according to the regions outlined in black in Figure 7.4 (Kiladis et al. 2009). In particular, the temporal progression of atmospheric variables as a function of pressure can be obtained by regressing against the satellite data with a time lag.

Figure 7.10 and 7.11 show the vertical structure of wind, temperature, and specific humidity for the Kelvin wave, westward mixed Rossby-gravity wave (MRG), eastward mixed Rossby-gravity wave (EIG), and n=1 equatorial Rossby wave, respectively, using rawinsonde data at the island of Majuro (7.1^{o}N, 171.4^{o}E) regressed against satellite brightness data with the same temporal, resolution at the grid point closest to Majuro.

A striking feature of all but the equatorial Rossby wave is the vertical tilt of the wave in the direction opposite to its propagation; e.g. the Kelvin wave tilts westward with height. The relationships between the 850 hPa and 150 hPa zonal wind anomalies are close to what one would expect if the first baroclinic mode were dominant, but the existence of significant anomalies in the middle troposphere is not consistent with first baroclinic mode structure. We will return to this issue when we discuss theoretical explanation for these wave modes, but in short, many theories now incorporate the barotropic mode together with the first baroclinic mode, and/or allow for non-moist adiabatic behavior such as the second baroclinic model. Either of the barotropic or the second baroclinic modes, in tandem with the first baroclinic mode, can potentially explain the wave tilt seen in Figures 7.10 and 7.11.

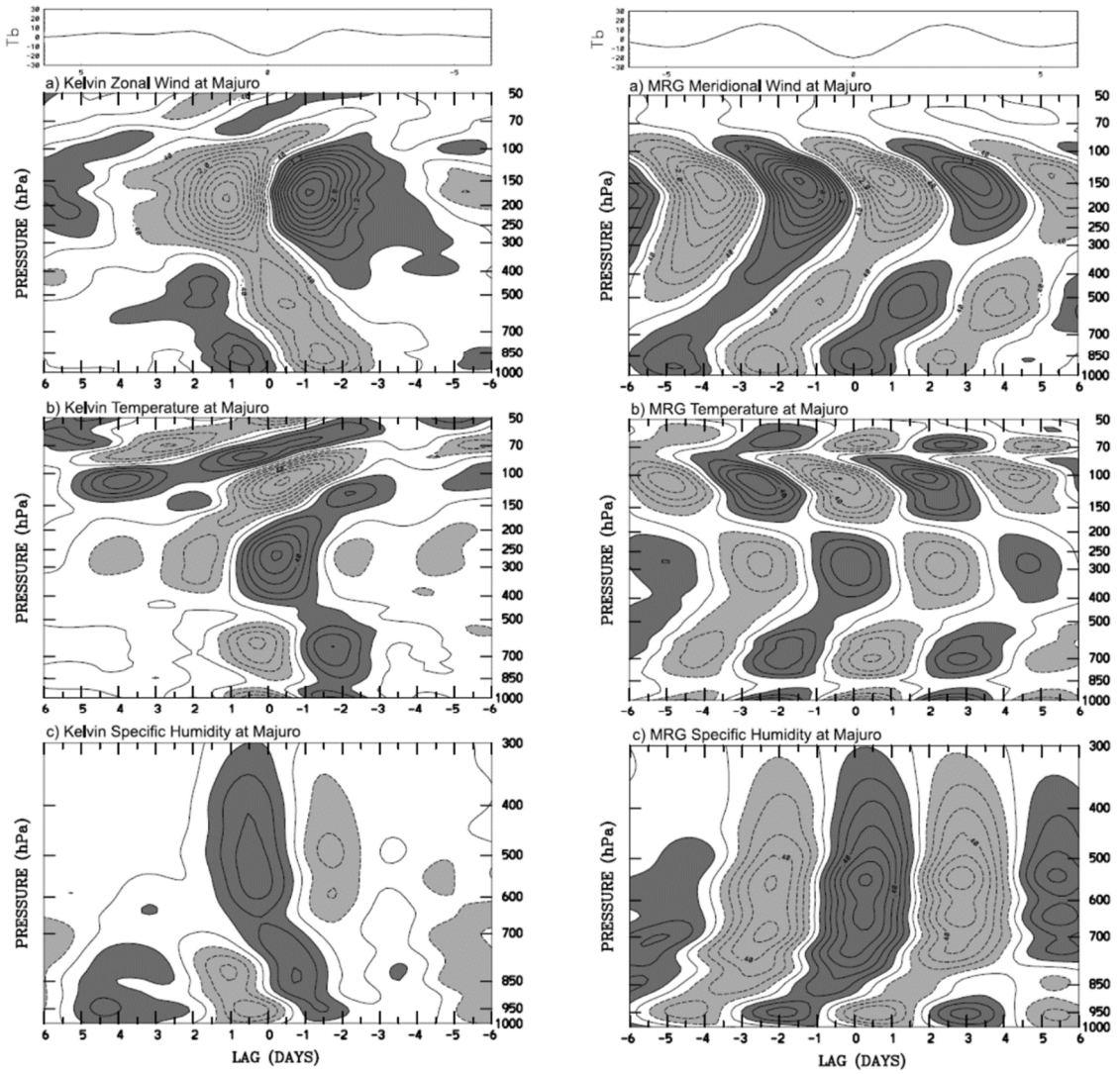

Figure 7.10: Time-pressure sections of anomalous zonal wind (top), temperature (middle), and specific humidity (bottom) from rawinsonde data at Majuro regressed against satellite brightness data filtered in the wavenumber-frequency domains shown in Figure 7.4 for the Kelvin wave (left) and the westward mixed Rossby-gravity wave (MRG; right). Negative lag indicates rawinsonde fields leading the satellite brightness temperature. All fields have been scaled to a brightness temperature anomaly of -20 K. Contour interval is 0.4 m s^{-1} for wind, 0.1 K for temperature, and 0.1 g kg^{-1} for specific humidity, with negative contours dashed and dark shading representing positive perturbations. The corresponding brightness temperature is shown at top, in K.

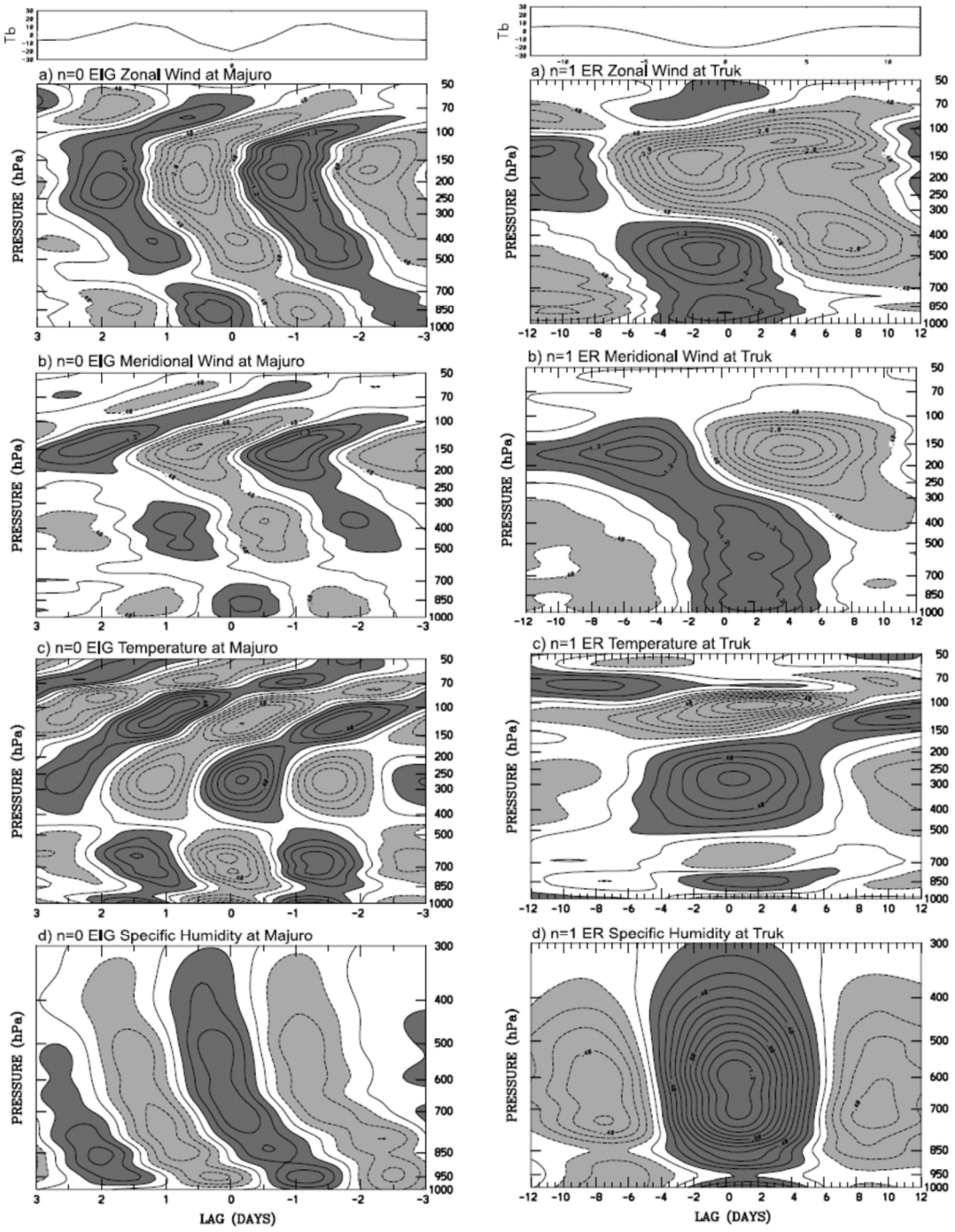

Figure 7.11: Same as Figure 7.10 except showing the eastward missed Rossby-gravity wave (EIG; left) and the n=1 equatorial Rossby wave (ER; right), except that the second row shows the meridional wind anomaly (same contour interval as used for the zonal winds).

Consistent with the possible presence of a second baroclinic mode, the vertical structures of temperature anomalies for all but the equatorial Rossby wave appear to have two maxima within the troposphere as well as one or more maxima in the lower stratosphere, though the amplitude of the temperature anomalies is not very large compared to expected rawinsonde sampling and instrumental error, so one should exercise some caution in interpreting them.

The vertical structure of the equatorial Rossby mode (right column of Figure 7.11) is much more consistent with dominance by the first baroclinic mode. At first blush, it looks like the temperature structure may have higher order mode contributions, but it must be remembered that the dynamically essential variable here is virtual temperature, not actual temperature. In round numbers, 5 contours of specific humidity is worth one contour of temperature, in terms of its effect on virtual temperature. Thus the single negative contour of temperature near 700 hPa (right side of Figure 7.11, third row, near a time lag of 0-2 days) is easily outweighed by the ~10 contours of specific humidity at the same time lag and pressure in terms of its effect on virtual temperature. Thus, it is likely that, consistent with the dominance of the first baroclinic mode in zonal winds, the is a single maximum in the vertical structure of virtual temperature anomalies.

Close inspection of Figures 7.10 and 7.11 show that in the lower stratosphere (above 150 hPa), for all but the equatorial Rossby mode, the phase lines are tilted in the direction of wave propagation. This indicates upward wave group velocity in the lower stratosphere, consistent with upward radiation of wave energy. The observations therefore indicate that approximating the tropopause as a rigid lid may not work well for these faster wave modes. In the case of the equatorial Rossby mode, however, the signal is muted and ambiguous above the tropopause, so these low frequency modes may not be losing much energy to the stratosphere.

7.2.3: Equatorial subseasonal variability in a convection-permitting global model

How well do current global climate models simulate subseasonal tropical variability? Most climate models have horizontal resolutions insufficient to permit explicit simulation of moist convection, and therefore have to represent moist (and dry) convection using parameterizations. A thorough analysis of two most recent generations of models that participated in the Climate Model Intercomparison Project (CMIP)[3] show that their simulation of convectively coupled waves is highly inconsistent among models, and only one of the many different models was able to simulate an eastward-propagating Madden-Julian Oscillation (Hung et al. 2013). It is widely believed that deficiencies on cumulus parameterizations are responsible for the relatively poor performance of climate models in simulating this kind of variability.

In recent years, advances in numerical modeling and in computing allow one, for the first time, to simulate global climate on the time scale of several years with horizontal resolution that permits explicit simulation of moist convection, although the convective clouds are poorly resolved. These models simulate tropical variability at many scales and reproduce much of the observed subseasonal variability near the equator. Here we analyze the output of one such model, an aquaplanet global version of the System for Atmospheric Modeling (SAM,

[3] https://www.wcrp-climate.org/wgcm-cmip

Khairoutdinov and Randall 2003), with equatorial horizontal grid spacing of about 20 km and a zonally invariant sea surface temperature distribution given by

$$SST = 273 + 27\left(1 - \sin^6(\theta)\right),$$

where θ is the latitude in radians and SST is in kelvins. This distribution is displayed in Figure 7.12.

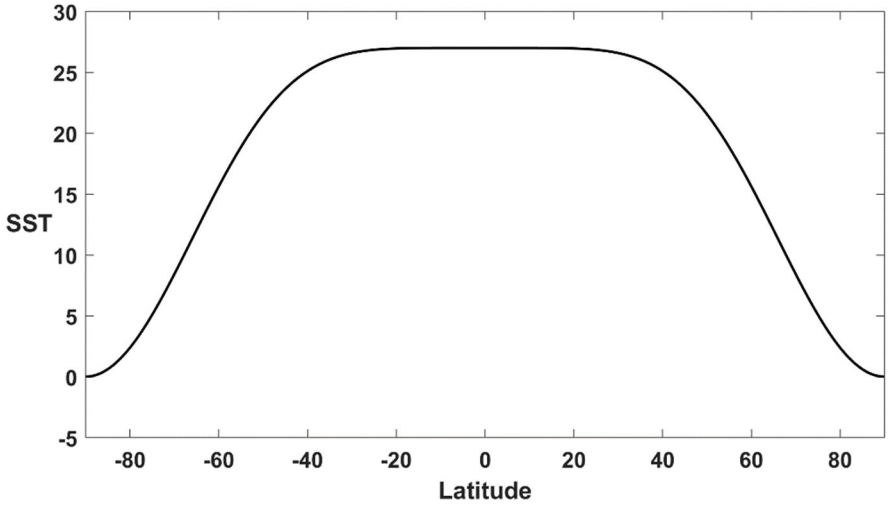

Figure 7.12: Distribution of sea surface temperature used in the convection-permitting simulations on an aquaplanet.

The tropical SST is much flatter than observed, and does not vary in time. The intent is to minimize the influence on the tropical atmosphere of baroclinic wave activity from higher latitudes. Experience with convection-permitting aquaplanet models shows that if SST has no meridional gradients at all, the climate becomes dominated by tropical cyclones at high latitudes. The SST distribution shown in Figure 7.12 is a compromise designed to minimize the influence of baroclinic instability and high latitude tropical cyclones.

This global version of SAM has insolation of $400\,Wm^{-2}$, constant in space and time, and has state-of-the-art representations of subgrid-scale turbulence and cloud microphysics, including the ice phase. The model is run for 360 days and we analyses the last 300 days of the simulation.

Figure 7.13 shows a snapshot of outgoing longwave radiation and 850 hPa winds at day 170 of the simulation. Gentle mean easterlies are present in the tropics, though clearly modulated at zonal wavenumber 1. Tropical cyclone-like disturbances are evident at around 30° latitude in both hemispheres; reference to Figure 7.12 shows that these are over very warm water but near the shoulders of the SST distribution, where the Coriolis parameter is relatively large. (Chavas and Reed (2019) showed that tropical cyclogenesis is strongly suppressed within an equatorial deformation radius of the equator.) At higher latitudes, baroclinic waves prevail, and the mean surface winds are westerly. Note also the relative lack of low OLR in the subtropics, between about 20° and 25° latitude, between the equatorial belt and the region of tropical cyclones. Cross-sections (not shown here) reveal these as the descent branches of Hadley-like circulations.

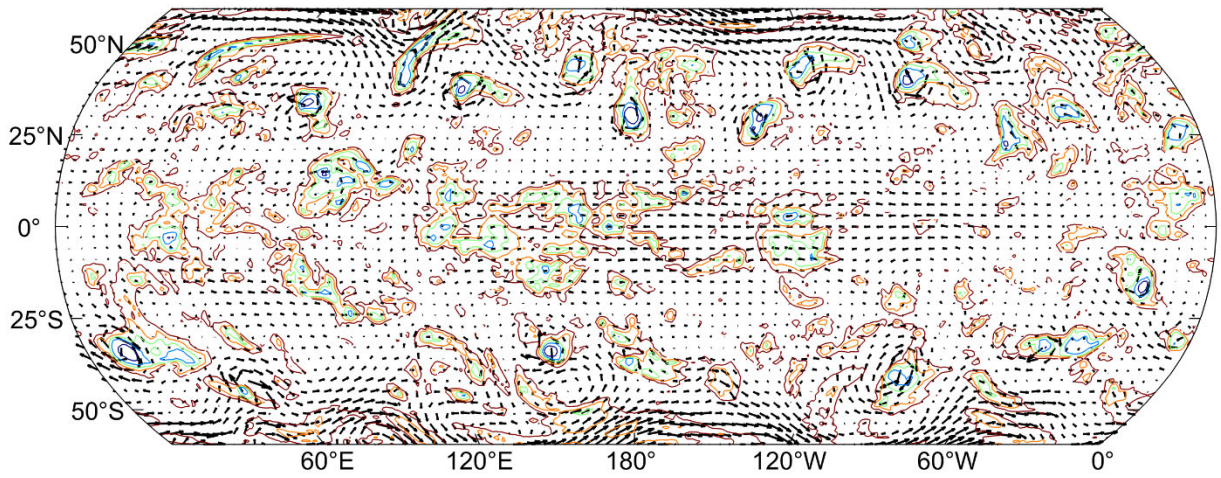

Figure 7.13: Outgoing longwave radiation (contoured only for values less than 280 W m^{-2}) and 850 hPa winds (arrows) on day 170 of a 360-day global SAM simulation.

A time-longitude section of outgoing longwave radiation averaged between 10^{o} S and 10^{o} N for the last 300 days of the simulation is shown in Figure 7.14. Aside from interpolation to a uniform 1-degree grid, no filtering has been applied.

The most prominent signal obvious to the naked eye is a wavenumber 1 disturbance propagating eastward with a period of around 40 days; this is the model's analog to an MJO. But there is also organized convection at small scales and higher frequencies, including a prominent westward-propagating mode that takes roughly 100 days to traverse the globe.

Spectral power density of precipitation averaged between 10^{o} S and 10^{o} N for the last 300 days of the simulation is shown in Figure 7.15, for the equatorially symmetric and anti-symmetric components. These plots have been made following the procedure described in Wheeler and Kiladis (1999) except that there is no need here to remove an annual cycle; and, as described before, the subtracted background consists of the average of the symmetric and anti-symmetric components. To deal with the quantization in zonal wavenumber, the plots have been smoothed in wavenumber only (not frequency) using a 1-2-1 smoother applied successively 7 times.

The equatorially symmetric precipitation power spectra exhibit a prominent peak at eastward zonal wavenumber 1 and frequencies ranging from once in 96 days to once on 24 days. (Note that the procedure for frequency decomposition operates on multiple 96-day subsets of the 300-day record, so that frequencies are quantized in increments of 1/96.) This peak, corresponding to the model's rendition of an MJO, is by far the largest spectral peak in the dataset. There is also a broad band of power extending along the convectively coupled Kelvin wave curve corresponding to an intrinsic phase speed of about $12\ ms^{-1}$, and some power in westward-moving disturbances possibly corresponding to $n=1$ equatorial Rossby waves.

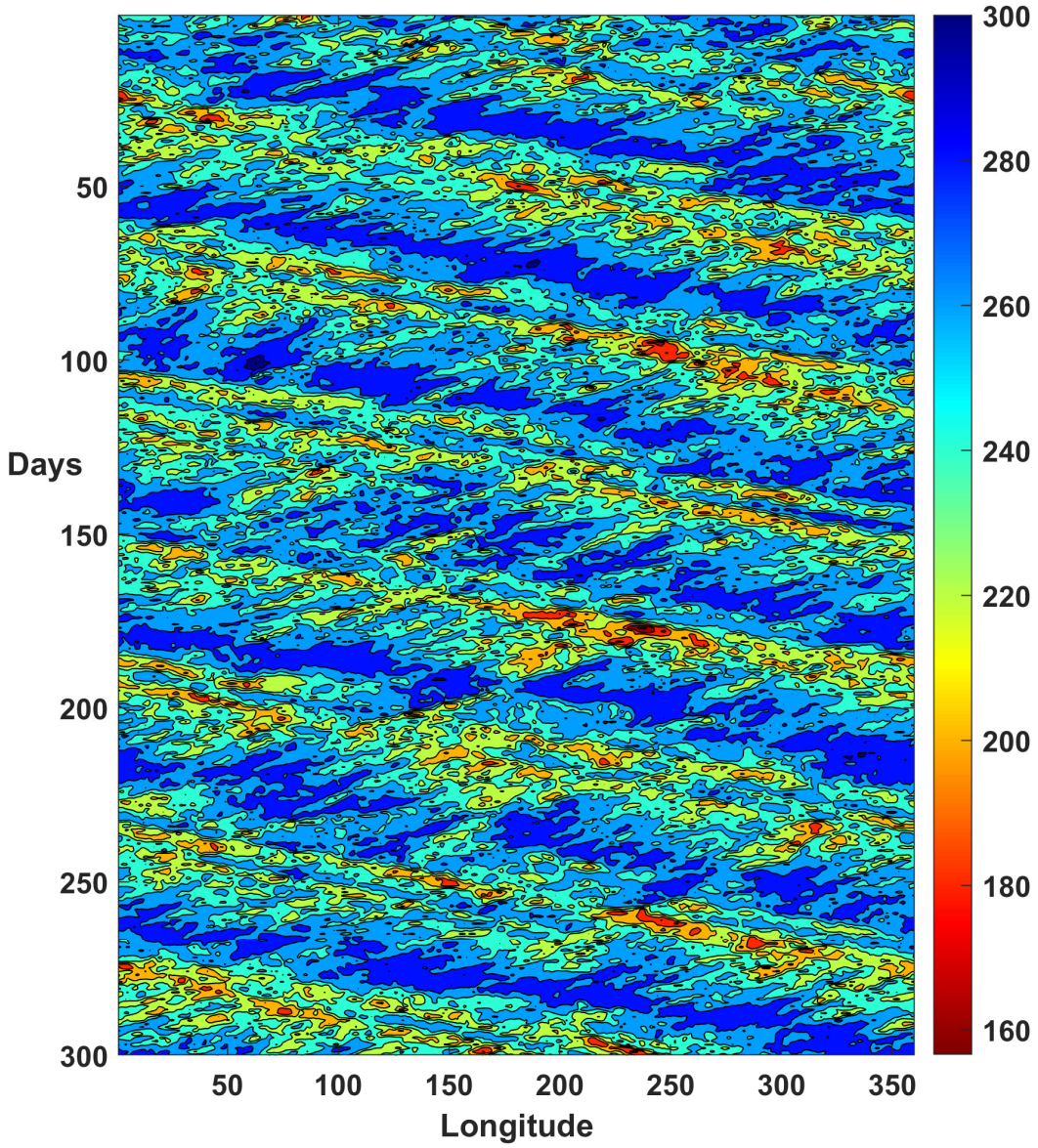

Figure 7.14: Outgoing longwave radiation (W m^{-2}) averaged between 10^{o} S and 10^{o} N during the last 300 days of the simulation. Model output has been interpolated to a 1-degree grid.

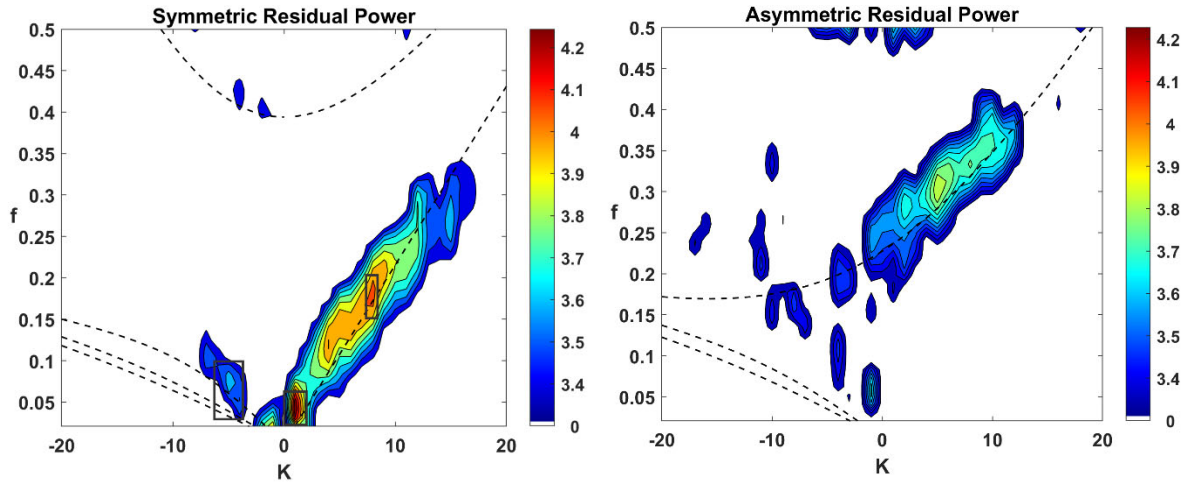

Figure 7.15: The base 10 logarithm of the spectral power density of precipitation from the last 300 days of the global SAM simulation. Equatorially symmetric (left) and antisymmetric (right) components. Power has been smoothed in wavenumber only by applying a 1-2-1 smoother 7 times. Values less than 3.3 have not been contoured. The dashed lines show the Matsuno dispersion curves for n= -1 to +5 assuming a shallow water phase speed of 12 ms^{-1}, with all curves Doppler shifted assuming a background easterly wind of 2 ms^{-1}. The solid boxes in the left-hand plot show the filtering domains for the n=1 equatorial Rossby wave, MJO and Kelvin waves, from left to right.

The equatorially anti-symmetric power spectral density plot shows a broad maximum along the Doppler-shifted mixed Rossby-gravity wave dispersion curve corresponding to the non-rotating shallow water intrinsic phase speed of $12\ ms^{-1}$ and extending from eastward zonal wavenumber 0 through about 12. Unlike the observed spectrum (Figure 7.3 and 7.4, right panels) there is little power in westward-propagating mixed Rossby-gravity waves. The peak signal strength is not quite large enough to obtain good reconstructions of spatial variability.

To examine the spatial structure of the SAM equatorial variability, we first choose a base variable that will serve as wave tracer and filter to include specified wavenumber-frequency combinations as indicated by the boxes in the left panel of Figure 7.15. The next step is to subdivide the longitude-time series at each latitude into space-time subdomains whose longitudinal extent is the wavelength of a single specified wavenumber and whose time extent corresponds to the period of the lowest specified frequency. For each subdomain, we calculate the frequency-wavenumber spectra and filter out all but the desired range of frequencies and single wavenumber. We then recombine the remaining frequencies and wavenumber into time-longitude sections, averaging them between specified latitude bounds corresponding approximately to expected meridional scales of the disturbances (e.g. 15^{o} in the case of the MJO mode). At each time, we find the longitude of the maximum or minimum of the base variables…this longitude is not necessarily continuous in time.

We similarly filter all the other variables of interest and recombine the filtered single wavenumber and frequency range into time-longitude sections at each latitude for each space-time subdomain. We then average these in time but use longitude relative to that of the maximum or minimum value of the base variable, as described in the previous paragraph[4]. Finally, we average the results over all the space-time subdomains. The disadvantage of this

[4] This procedure differs from the time lag analysis employed by Wheeler and Kiladis (2000) and here takes advantage of the zonal statistical homogeneity of the SAM aquaplanet fields.

method is that it only includes a single wavenumber and the lowest specified frequency and its harmonics up to a specified upper bound; it excludes frequencies higher than the specified lower bound but not part of the set of harmonics of the lower bound.

To create a composite vertical structure on the equator we apply the same procedure, but substituting pressure for latitude.

As mentioned previously, this procedure failed to detect any coherent structures anywhere in the equatorially anti-symmetric part of the power spectrum.

a. The MJO

For the MJO we used OLR as the base variable. The horizontal structure of the MJO mode is summarized in Figure 7.16. Following Wheeler set al. (2000), this composite includes both equatorially symmetric and anti-symmetric components. Near the equator, the wind and surface pressure fields have the same relative relationship as in a classical Kelvin wave, with the strongest easterlies aligned with the lowest surface pressure.

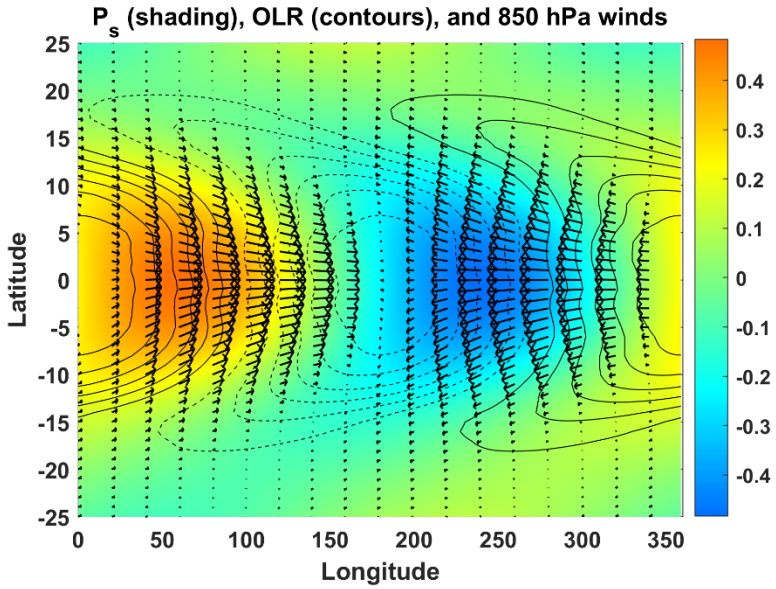

Figure 7.16: Composite structure of the MJO mode in the SAM aquaplanet simulation. Surface pressure (hPa) shaded, OLR contoured, with dashed lines denoting negative anomalies, and 850 hPa winds denoted by arrows. The maximum wind speed anomaly is 2.3 ms^{-1} and the maximum OLR anomaly is 10.0 W m^{-2}. This composite includes both equatorially symmetric and antisymmetric components, though it is dominated by the former.

Unlike a pure Kelvin wave, the meridional velocity off the equator is non-zero and shows meridional convergence west of and divergence east of the OLR minimum.

The physics driving this mode is illuminated through the budget of vertically integrated moist static energy, as illustrated in Figure 7.17.

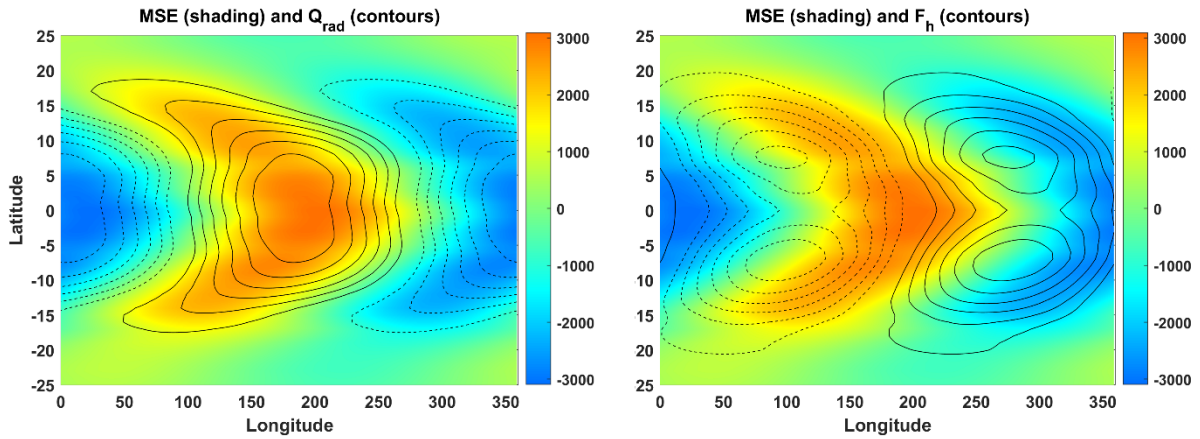

Figure 7.17: Composite structure of column-average moist static energy (J Kg^{-1}; shading) and column-integrated radiative heating (contours in left panel) and surface enthalpy flux (right panel) for the MJO mode. The maximum absolute value of the column-integrated heating is 9.3 W m^{-2} and the maximum absolute value of the surface enthalpy flux is 8.7 W m^{-2}.

The budget equation for the moist static energy, vertically integrated through the troposphere, may be written

$$\frac{\partial \langle h_m \rangle}{\partial t} + c\frac{\partial \langle h_m \rangle}{\partial x} = -\langle \mathbf{V} \bullet \nabla h_m \rangle - \left\langle \omega \frac{\partial h_m}{\partial p} \right\rangle + F_0 + R, \tag{7.2}$$

where the angle brackets denote a mass-weighted vertical integral through the depth of the troposphere, h_m is the moist static energy, c is the zonal phase speed of the disturbance, the first term on the left of (1) is the vertically integrated horizontal advection of moist static energy, the second term is the integrated vertical advection, the third term is the surface enthalpy flux, and the last term is the column-integrated radiative heating, which is just the difference between the surface and tropopause values of the net radiative flux.

In the long run, and in a coordinate system moving zonally with the disturbance, we expect the left side of (1) to vanish if the system is in a steady state. Then the right side of (1) should sum to zero.

Figure 7.17 shows the vertically averaged moist static energy (shading) and the radiative (left panel) and surface flux (right panel) terms in (1). Khairoutdinov and Emanuel (2018) showed in a similar simulation that the surface flux and radiative terms in (1) were very nearly balanced by the vertical advection term, so we do not show that here. The net radiative heating term is strongly correlated with the vertically averaged moist static energy itself, so that this mode is being strongly amplified by radiation. The surface flux variability, much of which is owing to fluctuating surface wind speed, is nearly in quadrature with the moist static energy, so that WISHE is driving the wave eastward. But close inspection of the figure reveals a small negative correlation between moist static energy and the surface enthalpy flux, so the latter is exerting a weak damping effect in the wave.

In short, the MJO in this model is being driven by radiation (most of whose variability is driven by clouds) and propagated eastward by WISHE.

The vertical structure of the MJO mode, subject to the same filtering, is shown in figure 7.18. The zonal wind, vertical velocity, and virtual temperature have tropospheric structure consistent with a dominant first baroclinic mode structure, as predicted in an atmosphere constrained to have a moist adiabatic virtual temperature lapse rate. The slight forward tilt of the zonal wind structure is consistent with the presence of a barotropic component excited by some combination of upward energy radiation into the stratosphere and surface friction. The forward phase tilt of the structures of all four variables in the stratosphere is owing to upward radiation of wave energy by Kelvin waves, a process difficult (but not impossible) to include in simple linear models. [Reference Jonathan Lin if he has a paper out on this.] The moist static energy has a pronounced eastward tilt, with anomalies in the shallow convective boundary layer (below about 900 hPa) of the opposite sign as free tropospheric anomalies. Given that deep convection is likely mostly in phase with the large-scale vertical velocity, it may be the case that the deep convection is simultaneously increasing the moist static energy of the free troposphere and reducing it in the boundary layer through downdrafts. Note, as predicted by convective neutrality, that the boundary layer moist static energy is in phase with the free tropospheric virtual temperature.

b. Kelvin waves

We apply the same procedure to examine the structure of Kelvin waves, focusing on zonal wavenumber 9 and frequencies from once in 10 days to once in 5 days, but in contrast to the MJO we consider only equatorially symmetric perturbations. Figure 7.19 shows the horizontal structure of this relatively low frequency Kelvin mode. The structure of the wind and pressure field is that of a classical Kelvin wave, with the zonal winds very nearly in phase with the surface pressure. There is no obvious meridional wind component, though the procedure does pick up maximum absolute values of about 0.05 ms^{-1}, perhaps more a measure of how adept the procedure is than of any real meridional wind contribution. Note that the OLR minimum is displaced west of the maximum convergence of 850 hPa zonal winds.

The phase relationships between the column mean moist static energy and column radiative heating and surface enthalpy fluxes are shown in Figure 7.20. It is clear that both WISHE and radiation act in concert to amplify this Kelvin-like mode, with WISHE helping to drive it eastward while the radiation anomalies retard this motion. Curiously, when we apply the same diagnostics to lower frequency Kelvin-like modes (not shown here), the wave driving shifts away from WISHE and toward radiation, and conversely, at higher frequencies WISHE begins to dominate the wave driving. This demonstrates that the relative importance of different contributions to the column moist static energy budget may change along what appears to be a continuum in the power spectral density.

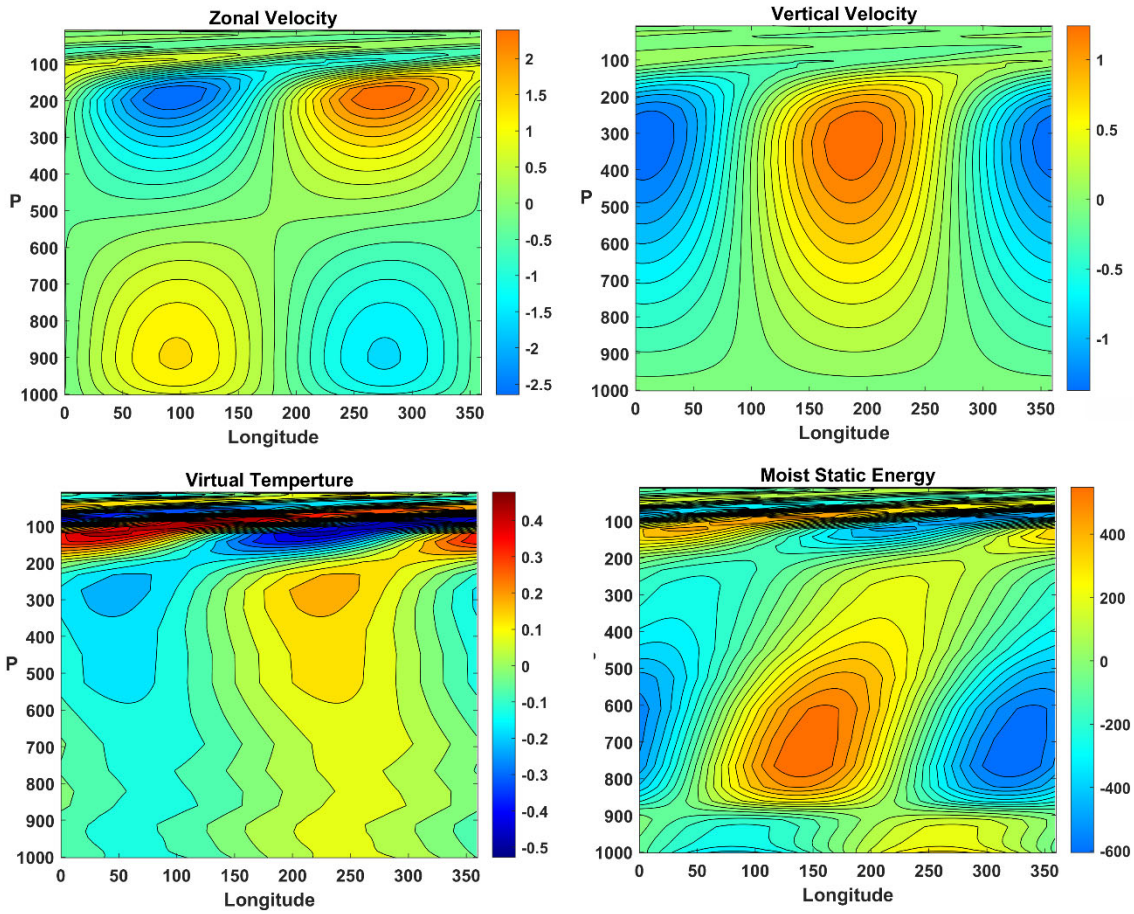

Figure 7.18: Vertical structure of the MJO mode averaged between 15°N and 15°S: Upper left: zonal wind (ms^{-1}); upper right: vertical velocity ($mm\ s^{-1}$); lower left: virtual temperature (K) and lower right: moist static energy ($J\ Kg^{-1}$).

The vertical structure of the $k = 9$ Kelvin mode is shown in Figure 7.21, where we have averaged the fields between 5°S and 5°N. It differs in several remarkable ways from the vertical structure of the MJO mode shown in Figure 7.18; most particularly, the virtual temperature strongly departs from first baroclinic mode structure and exhibits two prominent peaks in the troposphere and a third near the tropopause. Comparison of the virtual temperature with the boundary layer moist static energy suggests that while convective neutrality may hold for the lower half of the troposphere, it breaks down dramatically in the upper half, which is more or less in quadrature with the lower half. Both the zonal and vertical velocity fields tilt substantially westward with height, although they are otherwise consistent with first baroclinic mode structure, with two extrema of zonal wind in the troposphere and a single extremum of vertical velocity. As with the MJO, there are prominent indicators of upward radiation of Kelvin wave energy in the stratosphere.

Note that the vertical structure of this Kelvin-like mode strongly resembles the observed vertical structure of equatorial Kelvin waves, as shown on the left side of Figure 7.10, including the two temperature extrema in the troposphere and the westward-sloping zonal wind structure.

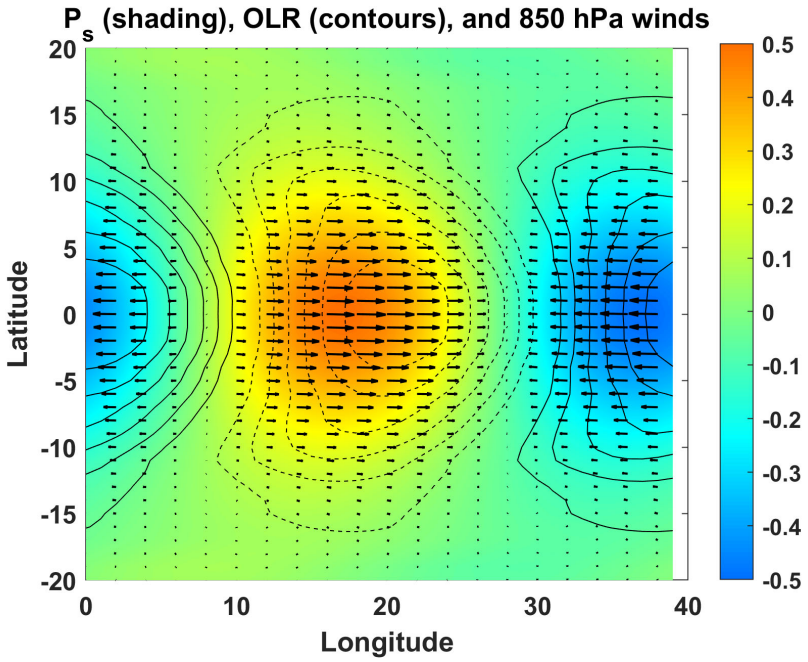

Figure 7.19: Composite structure of the Kelvin mode in the SAM aquaplanet simulation. Surface pressure (hPa) shaded, OLR contoured, with dashed lines denoting negative anomalies, and 850 hPa winds denoted by arrows. The maximum wind speed anomaly is 1.5 ms^{-1} and the maximum OLR anomaly is 17.3 W m^{-2}.

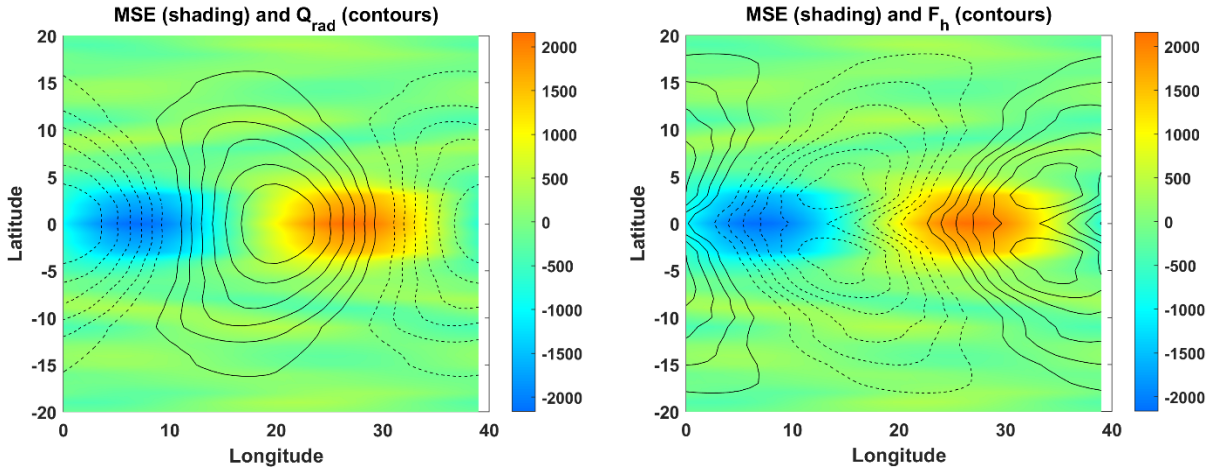

Figure 7.20: Composite structure of column-average moist static energy (J Kg^{-1}; shading) and column-integrated radiative heating (contours in left panel) and surface enthalpy flux (right panel) for the Kelvin mode. The maximum absolute value of the column-integrated heating is 17.7 W m^{-2} and the maximum absolute value of the surface enthalpy flux is 6.5 W m^{-2}.

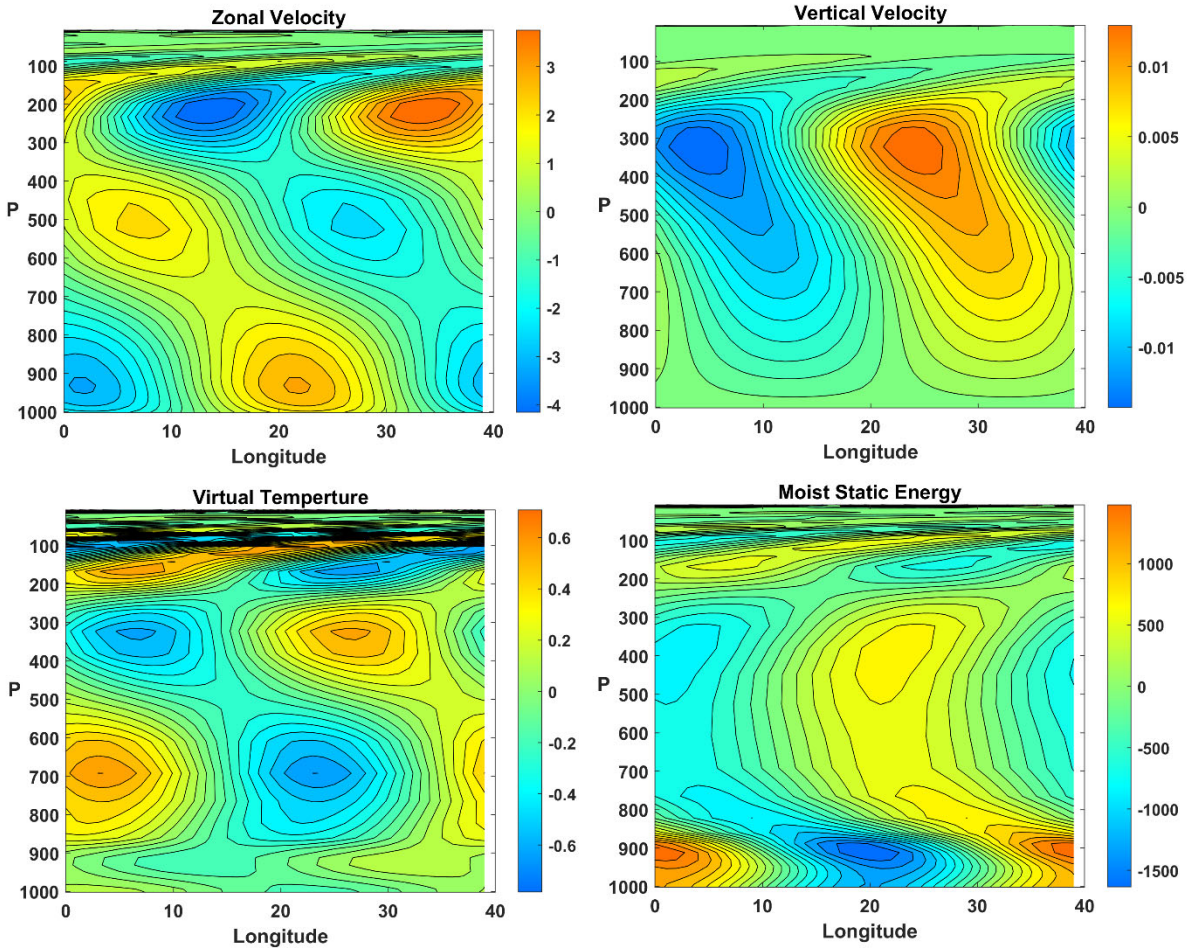

Figure 7.21: Vertical structure of the Kelvin mode averaged between 5ºN and 5ºS: Upper left: zonal wind (ms^{-1}); upper right: vertical velocity ($mm\ s^{-1}$); lower left: virtual temperature (K) and lower right: moist static energy ($J\ Kg^{-1}$).

c. Westward-propagating symmetric mode

Finally, we look at the structure of the variability in a region of spectral space ordinarily associated with an $n=1$ equatorial Rossby wave; this region is enclosed by the left-most box in Figure 7.15. Figure 7.22 summarizes the structure of this mode at wavenumber $k=-5$ and frequencies between 0.03 and 0.09 cycles per day. The structure of this disturbance does not resemble any single classical Matsuno mode. The phase relationship between the column mean moist static energy and the radiation and surface enthalpy fluxes (Figure 7.23) shows that this mode, like the MJO mode, is amplified by radiation and propagated (westward, in this case) by WISHE, which also slightly damps the wave. Unlike either the MJO or Kelvin modes, most of the strong forcing of the column moist static energy occurs well off the equator, even though the winds are strongest along the equator. The vertical structure of the disturbance (Figure 7.24) is close to the first baroclinic mode, but the free troposphere virtual temperature perturbations are not in phase with the lowest level moist static energy, so the waves are not maintaining strict moist neutrality, at least not along the equator. The lack of correspondence between the structure of this disturbance and that of any Matsuno mode cautions us against trying to fit all

equatorial variability into the simple framework of linear neutral, shallow water equatorial modes. If the effects of radiation and surface fluxes are strong enough, even a loose correspondence of the amplifying modes with neutral modes may vanish, leaving us without much vocabulary to label what we see in this model, and perhaps in observations as well.

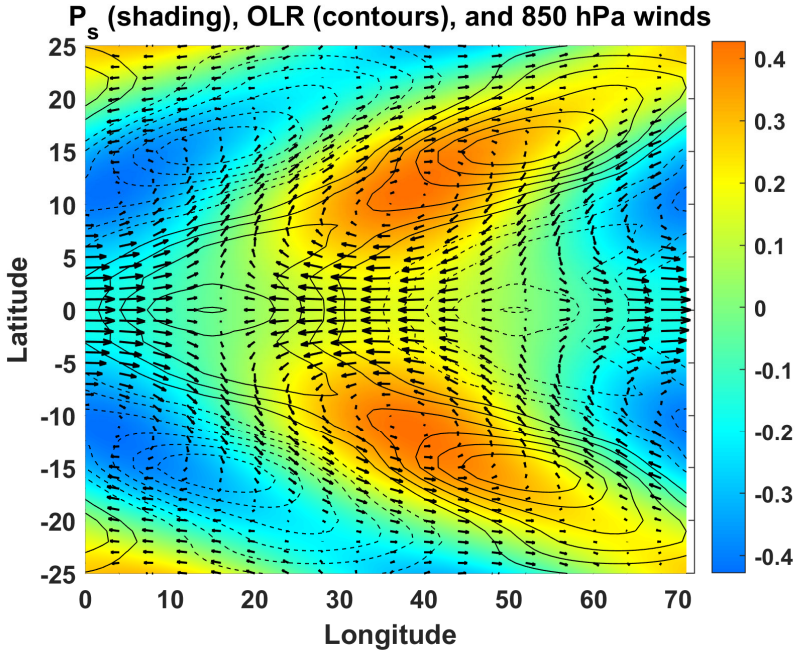

Figure 7.22: Composite structure of a low frequency westward-propagating mode in the SAM aquaplanet simulation. Surface pressure (hPa) shaded, OLR contoured, with dashed lines denoting negative anomalies, and 850 hPa winds denoted by arrows. The maximum wind speed anomaly is 2.9 ms^{-1} and the maximum OLR anomaly is 10.9 $W\ m^{-2}$.

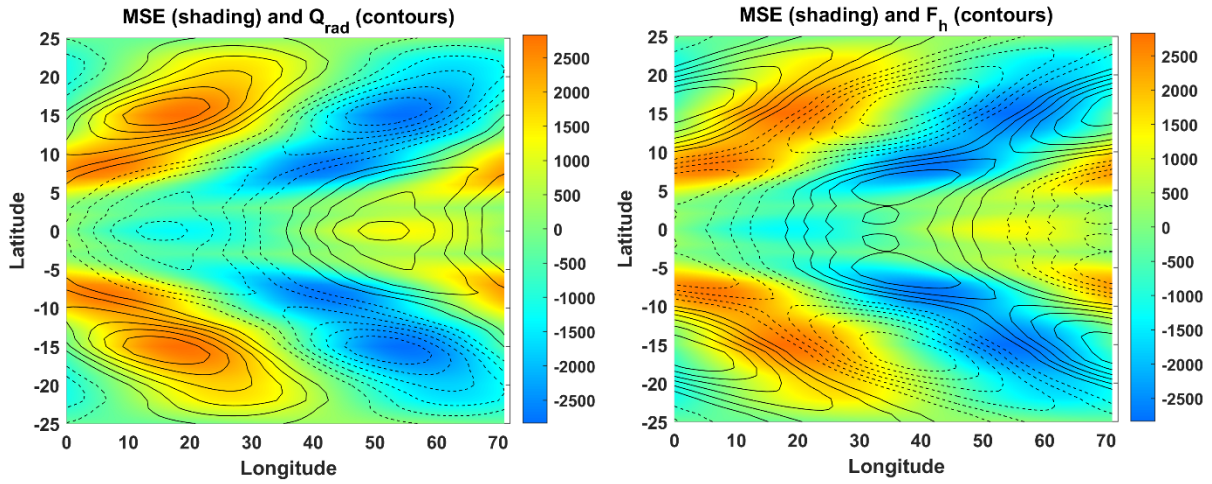

Figure 7.23: Composite structure of column-average moist static energy (J Kg^{-1}; shading) and column-integrated radiative heating (contours in left panel) and surface enthalpy flux (right panel) for the low-frequency, westward-propagating mode. The maximum absolute value of the column-integrated heating is 9.9 $W\ m^{-2}$ and the maximum absolute value of the surface enthalpy flux is 8.3 $W\ m^{-2}$.

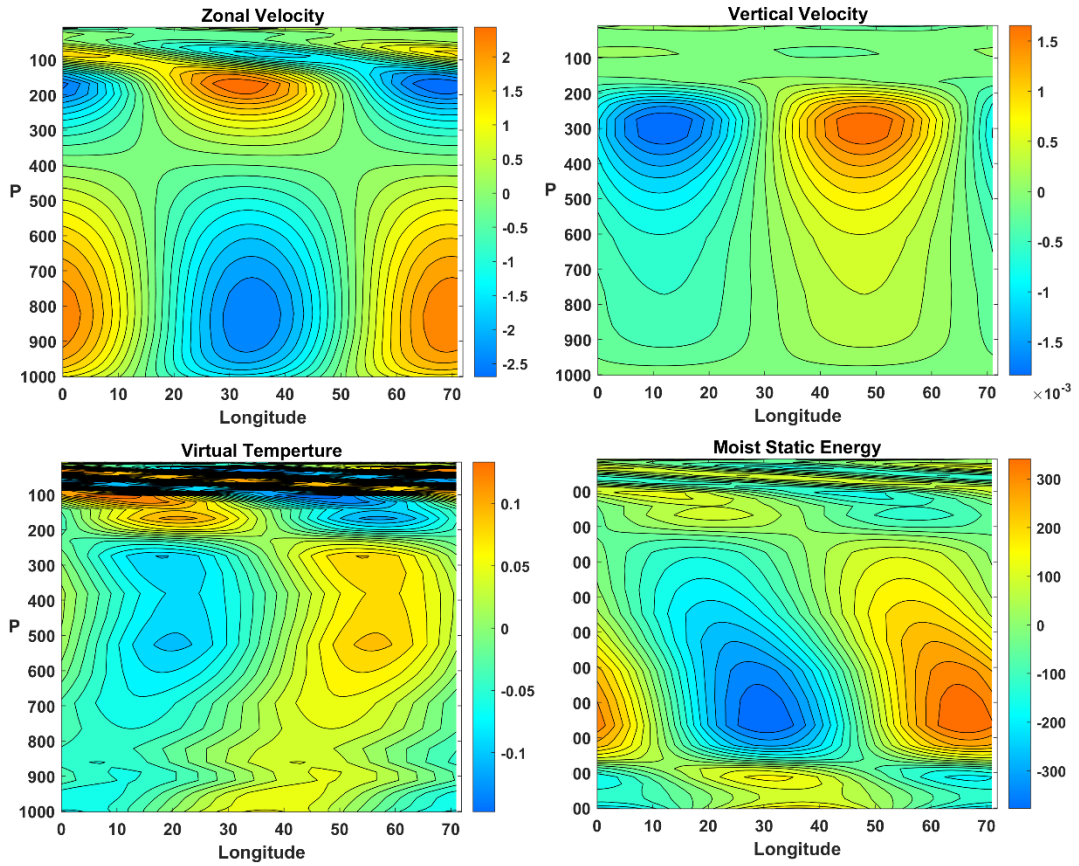

Figure 7.24: Vertical structure of the low-frequency, westward-propagating mode averaged between 8ºN and 8ºS: Upper left: zonal wind (ms^{-1}); upper right: vertical velocity (mm s^{-1}); lower left: virtual temperature (K) and lower right: moist static energy (J Kg^{-1}).

7.2.4 Theory

In Chapter 6 we showed that the variation of the Coriolis parameter across the equator has the effect of trapping various kinds of oceanic waves near the equator, and the very similar dynamics governing the moist adiabatic troposphere will likewise contain solutions in the form of equatorially trapped waves. We can explore these by adapting the linear atmospheric model developed in Chapter 6 and expressed there by equations (6.75) – (6.79). Given the rich variability produced by the SAM simulations with a fixed distribution of SST, described in the previous section, one can hope to produce some realistic variability in a linear model with fixed SST, so we omit perturbations to the surface saturation entropy, s_0^*. We drop the drag terms in the momentum equations. While these are not necessarily small, they do not appear essential to the problem and increase the mathematical complexity of the system.

The SAM results presented in the previous subsection demonstrate that variability of radiation is an essential element of tropical intraseasonal variability. We expect that most of this variability owes its existence to variations in tropospheric humidity and clouds; the tiny magnitude of

temperature perturbations (e.g. a few tenths of a degree in the SAM simulations) make that an unlikely explanation for the large variations in radiative cooling rates.

To make progress in relating variations in radiative cooling to the dependent variables of our linear system, we make use of am interesting relationship between OLR and moist entropy discovered by Sandrine Bony (Bony and Emanuel 2005) as illustrated in Figure 7.25, which shows a time series of satellite-measured OLR and compared it to the quantity $\ln\left(\frac{\theta_{eb}}{\theta_{em}}\right)$, where θ_{eb} is the equivalent potential temperature of the subcloud layer (975 hPa) and θ_{em} is the same quantity averaged between 975 hPa and 300 hPa.

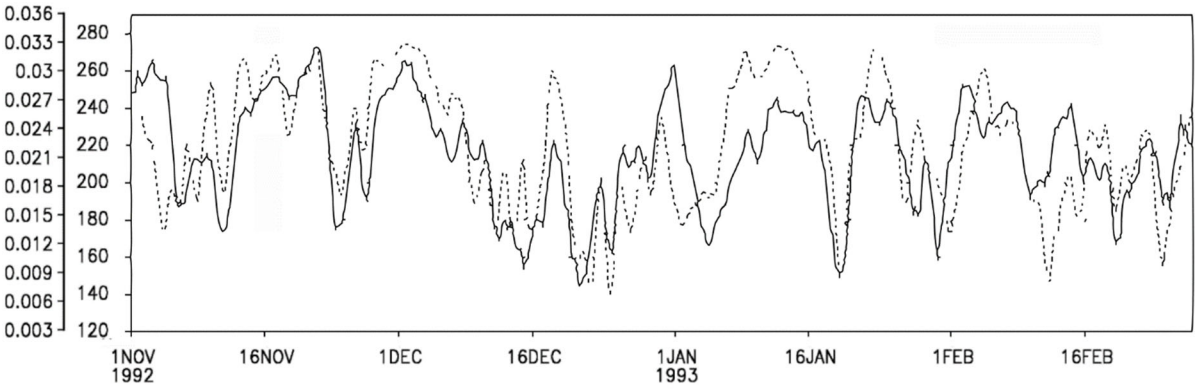

Figure 7.25: Time series of OLR (W m^{-2}; dotted curve) and the logarithm of the ratio of 975 hPa θ_e to the mean θ_e between 975 hPa and 300 hPa (solid). The OLR scale is on the inner side of the y-axis label, while the scale of the log of the ratios of θ_e is on the outer side of the y-axis label. From satellite and rawinsonde data collected during TOGA COARE.

The data were collected as part of the TOGA-COARE experiment in the western tropical Pacific in 1992-1993, with the equivalent potential temperature taken from an array of 4 rawinsondes (see Figure 3.18). If we assume that the modulation of net radiative cooling of the troposphere closely follows the modulation of OLR (i.e., neglecting variations of the net surface longwave flux and variations in the absorption of solar radiation in the troposphere), and we also assume that the variations in the ratio of subcloud layer θ_e to mean tropospheric θ_e are dominated by the latter[5], we can represent fluctuations in radiative cooling by the simple formula

$$Q = -Ch_m, \tag{7.3}$$

where C is a nondimensional constant that represents the magnitude of the modulation of radiative cooling, and h_m is the (nondimensional) perturbation column-average moist static energy of the troposphere.

[5] We could incorporate the effect of fluctuating subcloud layer θ_e, but that would only have the simple effect of slightly changing the value of the parameter χ in the equations.

Finally, to qualitatively mimic the effect of upward radiation of wave energy into the stratosphere (a process we will discuss later), we had a wavelength-dependent damping term to (6.79), which governs the evolution of column-mean moist static energy.

With this parameterization and the aforementioned assumptions, the linear model represented by equations (6.75) – (6.79) becomes

$$\frac{\partial u}{\partial t} = \frac{\partial s}{\partial x} + yv, \tag{7.4}$$

$$\frac{\partial v}{\partial t} = \delta\left(\frac{\partial s}{\partial y} - yu\right), \tag{7.5}$$

$$w = -\left(\frac{\partial u}{\partial x} + \frac{\partial v}{\partial y}\right), \tag{7.6}$$

$$\frac{\partial s}{\partial t} = -\left(\chi + \chi_2\right)s - \alpha u - w + \left(1 + C\right)h_m, \tag{7.7}$$

and

$$\gamma\frac{\partial h_m}{\partial t} = -\chi s - \alpha u - G_m w + Ch_m + d\frac{\partial^2 h_m}{\partial x^2}. \tag{7.8}$$

Here the new nondimensional parameter d governs the wavelength-dependent damping of moist static energy.

Recall that a fundamental assumption between this linear model of the equatorial troposphere is that the lapse rate of temperature is always moist adiabatic, and that this assumption filters out all but a barotropic mode and the first baroclinic mode. In this case, having assumed a rigid lid at the tropopause and no surface drag, only the first baroclinic mode survives. This mode has a single virtual temperature extremum in the troposphere, and while this is consistent with the MJO in observations and in the SAM model (see Figure 7.18), it is not consistent with observations or SAM simulations of the higher frequency modes such as Kelvin waves (Figures 7.10 and 7.21). For the present, we push on to examine solutions to this linear model, as a baseline, and later return to the issue of the higher frequency modes.

We begin by eliminating, through cross-differentiation, all the variables in (7.4) – (7.8) in favor of the meridional velocity, v, and look for modal solutions of the form

$$v = \mathrm{Real}\left[V(y)e^{ikx+\sigma t}\right], \tag{7.9}$$

where $V(y)$ is a complex function, k is the zonal wavenumber $\left(k = 1, 2, 3....\right)$ and σ is a complex growth rate. This yields an ordinary differential equation for $V(y)$:

$$\sigma a_3\frac{d^2V}{dy^2} - a_2 y\frac{dV}{dy} + \left[ika_3 - a_2 - \frac{\sigma}{\delta}\left(a_1\sigma + ika_2 + k^2a_3\right) - a_1y^2\right]V = 0, \tag{7.10}$$

where

$$
\begin{aligned}
a_1 &\equiv \chi\left(1+C\right)+\left(\chi+\chi_2+\sigma\right)\left(\gamma\sigma+dk^2-C\right),\\
a_2 &\equiv \alpha\left(\gamma\sigma+dk^2+1\right),\\
a_3 &\equiv \gamma\sigma+dk^2-C+G\left(1+C\right).
\end{aligned}
\tag{7.11}
$$

As can be verified by substitution, equation (7.11) has solutions have the form

$$V_n = H_n(y)e^{-by^2}, \tag{7.12}$$

where the complex exponential coefficient b is given by

$$b = \frac{-a_2 \pm \sqrt{a_2^2 + 4\sigma a_1 a_3}}{4\sigma a_3}, \tag{7.13}$$

and the $H_n(y)$ are Hermite polynomials whose first 4 terms are

$$
\begin{aligned}
H_0 &= 1,\\
H_1 &= y,\\
H_2 &= \frac{1}{2}y^2 + c_1,\\
H_3 &= \frac{1}{3}y^3 + c_2 y,
\end{aligned}
\tag{7.14}
$$

with constants c_1 and c_2 given by

$$
\begin{aligned}
c_1 &= \frac{\sigma a_3}{\left(2b\sigma - ik\right)a_3 + a_2 + \dfrac{\sigma}{\delta}\left(a_1\sigma + ika_2 + k^2 a_3\right)},\\
c_2 &= \frac{2\sigma a_3}{\left(6b\sigma - ik\right)a_3 + 2a_2 + \dfrac{\sigma}{\delta}\left(a_1\sigma + ika_2 + k^2 a_3\right)}.
\end{aligned}
\tag{7.15}
$$

For these solutions, the complex growth rate σ must satisfy the dispersion relation

$$\frac{1}{2}a_2 - ika_3 + \frac{\sigma}{\delta}\left(a_1\sigma + ika_2 + k^2 a_3\right) \pm \left(n + \frac{1}{2}\right)\sqrt{a_2^2 + 4\sigma a_1 a_3} = 0, \tag{7.16}$$

in which $n = 0,1,2,3....$, corresponding to the order of the Hermite polynomials in (7.14). The choice of sign in the square root in (7.16) must match that of (7.13). To satisfy the boundary conditions at $y = \pm\infty,$ the real part of b must be positive; any roots of (7.16) that do not satisfy this condition are discarded.

When (7.16) is expanded, it becomes apparent that it is an 8th order polynomial equation for the complex growth rate σ. We use a polynomial equation solver in MATLAB to solve this for the

those roots that obey the boundary conditions in y and check, by substitution, that they indeed solve the dispersion relation and the boundary conditions. Routines for finding these eigenvalues and plotting the associated eigenfunctions, for specified choices of the governing parameters, are available at the course website. Here we first consider some special cases before exploring the general solutions.

We first note that setting the damping parameters d, χ and χ_2, the WISHE term α, and the cloud-radiation term C all to zero reduces our system to a slightly modified form of the Matsuno equations for neutral oscillations on an equatorial β plane. (Setting h_m to zero in (7.7) decouples (7.8) from the rest of the system, which then takes the exact from of the Matsuno equations.) It can be demonstrated without solving the equations that their solutions are all neutral modes, which were described and discussed in Chapter 6.It can further be shown that including positive values of d, χ and χ_2 in any combination leads to solutions that decay exponentially in time. Amplifying solutions, on the other hand, require positive values of the WISHE parameter α and/or the cloud-radiation parameter C.

a. WISHE modes

We first explore amplifying disturbances that result from sufficiently large values of α while omitting the cloud-radiation terms. As a specific example, we take $\alpha = 1.5$, $\gamma = 1$, $G_m = 0.1$, $C = 0$, $\chi = 1$, $\chi_2 = 0.2$, $d = 0.02$, and $\delta = 30$. The dispersion solutions for growing modes only is shown in Figure 7.26.

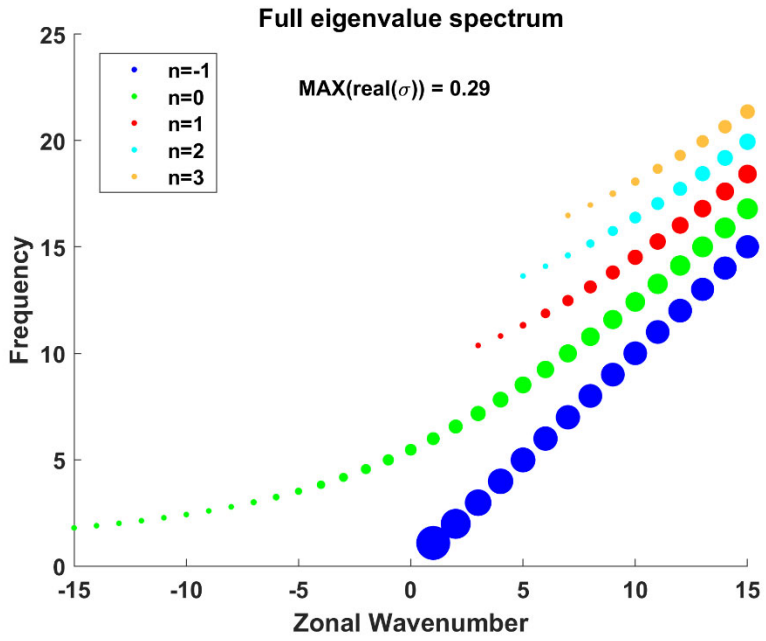

Figure 7.26: Amplifying solutions to the dispersion relation for WISHE-only wave driving and parameter values described in the text. The diameters of the circles are proportional to the exponential growth rate, with the value of the fastest growing mode indicated near the top of the figure. Solutions for the first 5 meridional mode numbers are displayed, including the Kelvin-like mode as n=-1, according to the colors described in the legend.

The $v = 0$ Kelvin-like mode grows most rapidly, especially at wavenumber 1. The other Matsuno-like modes also grow, but only the mixed Rossby-gravity mode shows growing, westward-propagating solutions and these do not grow as fast as their eastward-propagating counterparts. (When α is set to a negative value, there are growing, westward-propagating Poincare waves, but no other growing solutions.) Note also that, except for the Kelvin-like mode, growth rates increase with wavenumber, implying that disturbances with shorter zonal wavelengths should dominate.

The physics underlying the wave growth and propagation are straightforward to understand, and is illustrated in Figure 7.27. The structure is, to a close approximation, that of a classic equatorial Kelvin waves, with the strongest easterlies closely aligned with the minimum surface pressure, and ascent and descent nearly in quadrature with the temperature field (which is the inverse of the surface pressure field) but note the slight displacement of the w field such that it is slightly positively correlated with temperature, so that potential energy is being converted to kinetic energy. The surface enthalpy flux (right panel) is almost in quadrature with the column moist static energy, but here too there is a slight positive correlation between enthalpy flux and MSE, which is consistent with wave growth. Note also that the surface fluxes are shifted eastward from the maximum surface winds (see left panel)…this is because the saturation entropy is damping the surface fluxes, in phase with the entropy. The WISHE effect is responsible for both the wave growth and, in part, its eastward propagation. (The rest of the propagation can be regarded as the contribution (not shown in the figure) of vertical advection of moist static energy (third term on the right of (7.8)) to the net tendency of column moist static energy.)

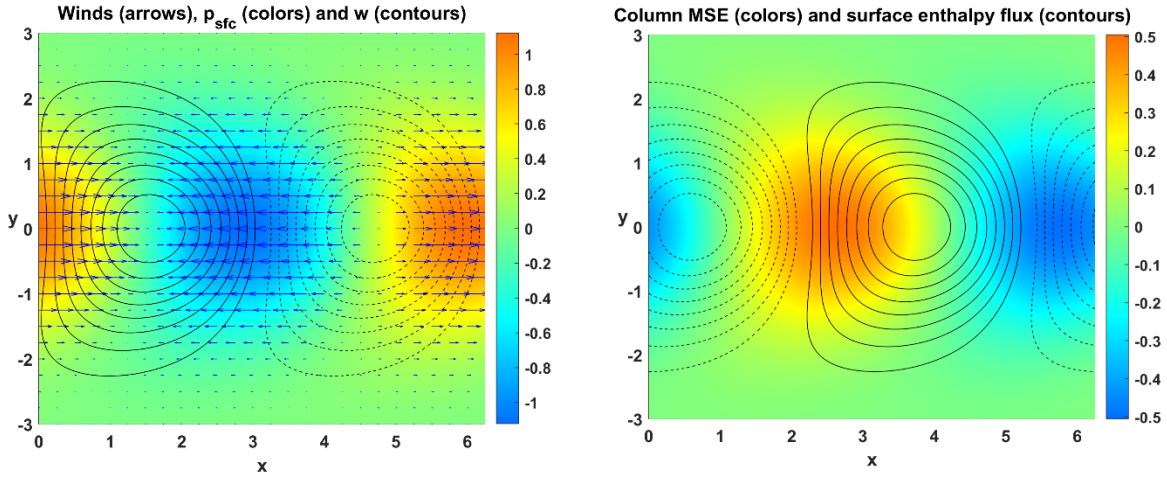

Figure 7.27: Eigenfunctions of the zonal wavenumber 1 Kelvin-like mode excited by WISHE. In the left panel, the shading shows the surface pressure, the vertical velocity is in black contours with dashes indicating negative values, and zonal wind is indicated by arrows. The right panel shows the column moist static energy (shading) and the surface enthalpy flux (black contours). The latitude variable is nondimensional, and the x axis spans one full zonal wavelength. The eigenfunctions also depend on the value of the precipitation efficiency, taken to be 0.8 here.

b. Effect of cloud-radiation interactions

Modulation of radiative cooling rates by clouds and water vapor have a large effect on low-frequency variability in the equatorial waveguide. This effect works in tandem with WISHE, turning on the cloud radiation term while turning off WISHE (not shown here) yields no viable growing solutions.

Figure 7.28 shows the dispersion relationship using the same parameters as in the previous subsection, but setting $C = 1$. Thus both WISHE and cloud radiation are active. The right panel of Figure 7.28 zooms in on the lower frequencies and wavenumbers

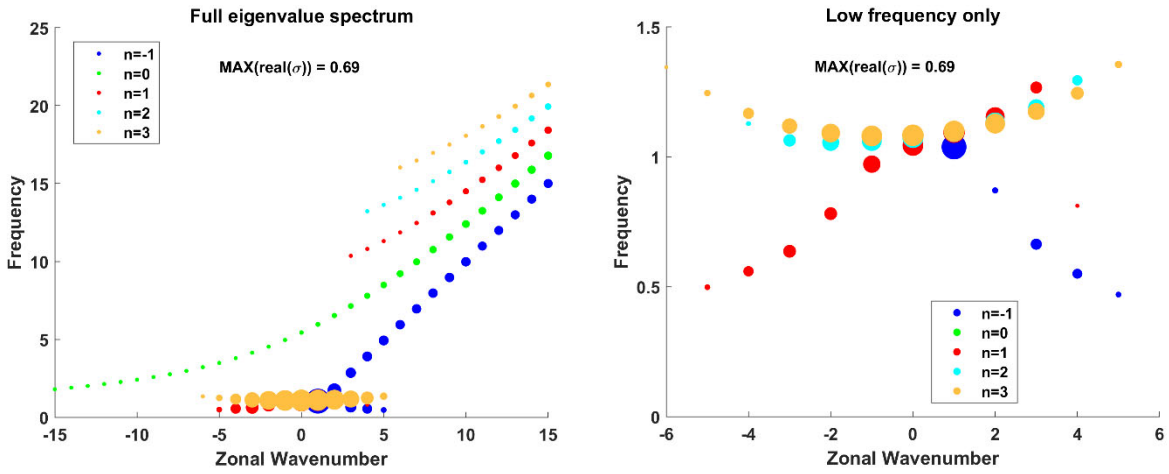

Figure 7.28: Amplifying solutions to the dispersion relation when both WISHE and cloud radiation interactions are active, and parameter values as before but with C=1. The right panel zooms in on lower frequencies and wavenumbers. The diameters of the circles are proportional to the exponential growth rate, with the value of the fastest growing mode indicated near the top of the figure. Solutions for the first 5 meridional mode numbers are displayed, including the Kelvin-like mode as n=-1, according to the colors described in the legend.

Note that the maximum growth rate is more than twice what is was in the WISHE-only solution. The higher frequency WISHE modes remain intact, but the very lowest frequency Kelvin-like mode is greatly amplified compared to its WISHE-only counterpart. But the most interesting feature is a new array of very low frequency disturbances spanning zonal wavenumbers between about -5 and 5. (Setting the diffusion parameter d to zero allows for growing low frequency solutions across the whole span of zonal wavenumber.) The right panel of Figure 7.28 zooms in on these. It is important to notice that these have no counterparts among the classical Matsuno modes, so we will avoid labeling them accordingly and refer to them simply as cloud-radiation modes. These can be regarded as the manifestation of self-aggregation of moist convection in the equatorial waveguide.

Figure 7.29 shows the structure of the $n = -1, \quad k = 1$ mode and the relationship between the column moist static energy and the surface enthalpy flux. (Note that in this parameterization, the radiative heating anomaly is just a constant multiplied by the column moist static energy itself.) the structure is similar, but not identical, to the structure of the WISHE-only mode shown in Figure 7.27, and the peak radiative heating anomaly is 88% of the peak surface enthalpy flux anomaly.

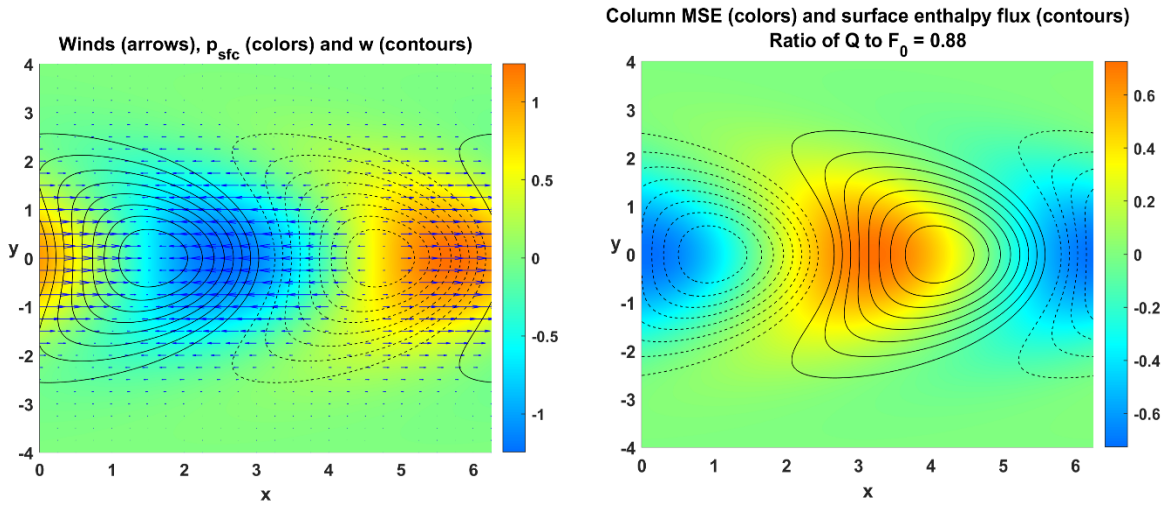

Figure 7.29: Eigenfunctions of the $n=-1, k=1$ mode with both WISHE and cloud radiation. In the left panel, the shading shows the surface pressure, the vertical velocity is in black contours with dashes indicating negative values, and zonal wind is indicated by arrows. The right panel shows the column moist static energy (shading) and the surface enthalpy flux (black contours); the cloud radiative heating anomaly is exactly in phase with the moist static energy itself. The latitude variable is nondimensional, and the x axis spans one full zonal wavelength.

The eigenfunctions shown in Figure 7.29 may be compared to the structures that emerge from a filtered analysis of the SAM aquaplanet modes shown in Figure 7.16 and 7.17. In particular, the phase relationship between wind and surface pressure (which in Figure 7.29 is just the saturation entropy with the sign flipped) is very similar to the SAM mode, while the left panel of Figure 7.17 shows that, as is assumed in the linear model, the radiative heating is very well aligned with the column moist static energy. In both SAM and the linear model, the surface enthalpy flux leads the column moist static energy anomalies, but in the linear model they are positively correlated with the column MSE, whereas in SAM the correlation is negative. Thus, WISHE is damping the SAM modes but acting to amplify the linear mode shown here. (It is possible that the linear correlation would be of the opposite sign for other combinations of parameter values.)

With some parameter combinations, the $n=-1, \quad k=1$ mode does not have the largest growth rate, and some interesting structures can appear with appreciable growth and $n>-1$. For example, Figure 7.30 shows aspects of the structure of the $n=1$ mode at zonal wavenumber 4, for the same parameters as used in Figure 7.28 and 7.29 except $C=1.5$ and $\chi=1.5$. Along the equator, the structure is approximately that of a Kelvin wave but with divergence of the meridional wind contributing negatively to the vertical velocity anomaly. Off the equator there are prominent cyclones and anticyclones manifested in both the surface pressure and wind fields.

The linear theory of equatorial waves suggests that while the WISHE effect can destabilize some of the classical Matsuno modes, cloud-radiation interactions can produce a new suite of unstable modes that have no counterparts among the Matsuno modes, including low frequency disturbances with gyres similar to equatorial Rossby waves but propagating eastward. Clearly, the modulation of radiative cooling rates by clouds and moisture is a critically important component of the physics governing many tropical phenomena.

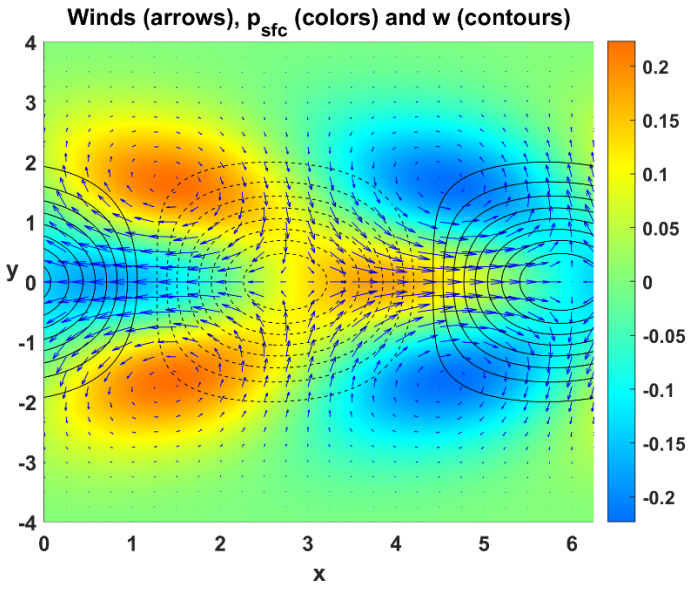

Figure 7.30: Eigenfunctions of the $n = 1, k = 4$ mode with both WISHE and cloud radiation. The shading shows the surface pressure, the vertical velocity is in black contours with dashes indicating negative values, and wind is indicated by arrows.

c. Effect of coupling to the stratosphere

The equatorial stratosphere, like the ocean and the troposphere, supports a spectrum of Matsuno modes, but unlike the troposphere, these are not coupled to convection or clouds or forced by surface fluxes or cloud-radiation interactions. Tropospheric disturbances can excite some of these wave modes, which carry the energy upward. For disturbances that behave like internal gravity waves, like Kelvin and Poincare waves, the vertical group velocity increases with the wave frequency, so for these modes the stratosphere acts as a reddening filter, allowing the higher frequency modes to escape upward more rapidly than the lower frequency modes. In linear theory, this damps the growth rates of otherwise growing modes in proportion to their wavenumber (Yano and Emanuel 1991) [Insert Jonathan Lin reference here].

For the more Rossby-like disturbances, such as equatorial Rossby waves and the westward-propagating mixed-Rossby gravity mode, the relationship between upward group velocity and wave frequency is more complex, but in general these disturbances have slower upward energy propagation and are thus better trapped in the troposphere; this is also true of the MJO [Lin reference].

Another effect of coupling to the stratosphere is to excite the barotropic component in the troposphere. The response of the tropopause effectively couples the barotropic and baroclinic modes, allowing energy to be transferred from the latter to the former. For reasonable values of the stratification of the stratosphere, the barotropic component is considerably weaker than the baroclinic wave and the superposition of the two modes gives a small eastward tilt with height of the eastward-propagating modes [Lin reference].

d. Effect of surface drag

Including the drag terms in linear systems like (7.4) – (7.8) also couples the baroclinic and barotropic modes and damps the growth rates. The surface drag operates directly on the boundary layer and this step-like vertical structure projects roughly equally on the barotropic and baroclinic modes. Unlike coupling to the stratosphere, surface drag damps disturbances more or less interpedently of their frequency, and so does not redden the overall spectrum. Solutions of (7.4) – (7.8) with surface drag were obtained by [reference to Jonathan Lin] and show, as expected, that the growth rates are diminished across the whole spectrum of unstable waves, but for reasonable values of the surface drag coefficient, not enough to eliminate the disturbances. As with the stratosphere coupling, the barotropic mode excited by surface drag is somewhat weaker than the baroclinic mode and leads to a small eastward tilt with height of the combined barotropic-baroclinic structure.

e. Excitation of higher order baroclinic modes

The vertical structure of temperature in observed Kelvin (Figure 7.10b) and Mixed Rossby-gravity (Figure 7.11c) waves, and the structure of virtual temperature in the SAM model Kelvin waves (Figure 7.21, lower left) show clear departures from the first baroclinic mode structure that would obtain if the troposphere always remained moist adiabatic. The magnitude of these higher frequency virtual temperature anomalies in the SAM simulations is around 0.5 K, a departure from moist adiabatic conditions that would be hard to detect in observations.

Khairoutdinov and Emanuel (2018) performed an experiment with an earlier version of SAM, zonally homogenizing radiative cooling rates and the wind speed that enters the formulation of surface sensible and latent heat fluxes. While several of the prominent equatorial modes, like the MJO and planetary Rossby waves, disappeared, there were still strong spectral peaks corresponding to Kelvin-like modes. While it is possible that these are weakly damped modes excited by convective noise and/or tropical cyclones and baroclinic waves at higher latitudes, one cannot rule out that these are locally generated within the tropics.

If the WISHE and cloud-radiation terms are set to zero in (7.4) – (7.8), these equations will admit growing solutions, provided the damping terms in (7.7) and (7.8) are small enough. In particular, it can be shown than for zero damping and asymptotically small G_m / γ, the complex growth rate is $-ik + G_m / 3\gamma$. It is not clear whether the energetics of such growing modes are internally consistent, and in any case, for reasonable values of G_m, γ, and the damping parameters χ and χ_2, all the $v = 0$ modes have negative growth rates.

The tilted vertical temperature structure of both observed and SAM-simulated higher frequency disturbances suggests that variations in the temperature lapse rate and/or coupling between the boundary layer and the free troposphere may play an important role in these disturbances. Several theoretical explanations have been proposed. Mapes (2000) presented a simple model of tropical atmospheric perturbations around and RCE state in which a second vertical mode is active and excited by variations in convective inhibition (CIN) brought about by stratiform rainfall. He termed the resulting instability “stratiform instability”, and the simple model is successful in re-producing the observed vertical structure of higher frequency tropical

disturbances, such a Kelvin waves. Another nice aspect of this model is that the energetics of the stratiform instability are internally consistent and involve the build-up and subsequent release of moist available potential energy, proximately controlled by variations in CIN. No modulation of surface enthalpy fluxes or radiative cooling is required. Temporal variations of CAPE in the mode are consistent with observed variations, with a build-up CAPE prior to convective onset followed by a rapid diminution.

Building on this work, Kuang (2008) proposed that while the lower tropospheric virtual temperature is tightly coupled to the boundary layer moist static energy, as assumed in the first-baroclinic-mode theory described earlier in this subsection, the upper tropospheric virtual temperature is strongly influenced by lower tropospheric humidity through its effect on convective cloud buoyancy and thus depth. He showed that the stratiform-type mode identified by Mapes could equally well be excited by variations in cloud depth brought about by variations in lower tropospheric moisture as by variations in CIN, and also obtained theoretical results in good agreement with observed Kelvin waves.

While much progress has been made in defining the characteristics of equatorially trapped disturbances by increasingly refined observational technology and analysis techniques, and in theoretical understanding of the origins of these modes, a fair number of different mechanisms remain in play and more work needs to be done to improve both the understand and numerical simulation of convectively coupled equatorial disturbances.

7.3 African easterly waves

Away from the equator, the trade winds are often perturbed by disturbances that are not related to equatorially trapped waves. These are often of “synoptic” scale, with wavelengths on the order of thousands of kilometers, and generally, though not universally, travel from east to west with the Trades. Since they appear as waves in surface isobars and in ground-relative streamlines, they are often described and thought of as waves, but though we will adhere to tradition and continue to refer to these as waves, most of them are almost certainly not waves in the dynamical sense, as they are not dispersive and have closed contours of conserved variables like potential vorticity. Some of these disturbances eventually become tropical cyclones.

As early as the 1940s, forecasters concerned with hurricanes in the tropical Atlantic, including the Caribbean and Gulf of Mexico, noticed westward propagating wavy disturbances in the summertime easterly low-level flow, which they referred to as “easterly waves” and regarded as precursors to hurricanes. The noticed that the waves not only modulated low-level winds but also rainfall, with rain usually suppressed west of the trough access and enhanced to the east, though later it was noticed that the opposite distribution sometime happens, especially in the far eastern North Atlantic. An example of an early analysis of such a wave is presented in Figure 7.31.

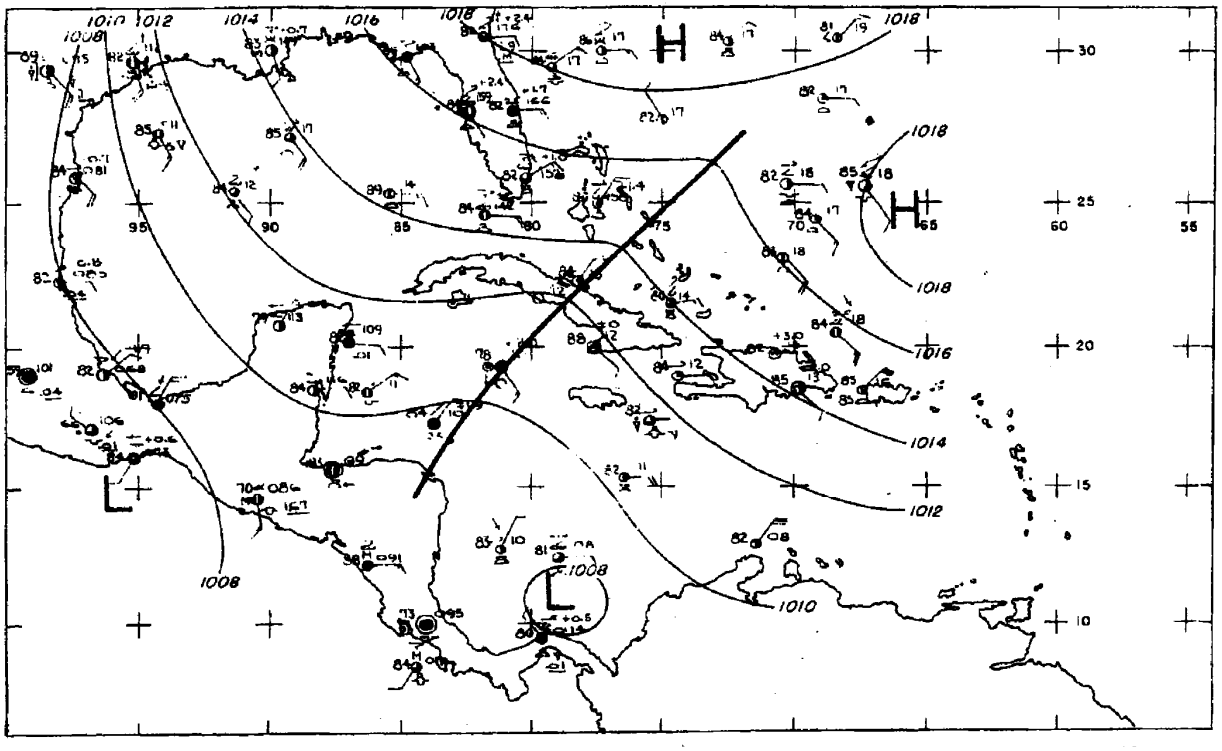

Figure 7.31: Surface weather map for September 9, 1941 at 00:30 GMT. The solid black curve shows the trough axis extending from the Bahamas to Central America. It had moved over Puerto Rico two days earlier. The circle and barbs depict weather conditions, including wind direction and speed, in standard meteorological notation. The trough is progressing northwestward.

The surface pressure and station winds indicate a general southeasterly flow, typical for the tropical North Atlantic in summer, but a prominent trough in the pressure field extends from Central America through Cuba and the Bahamas. This trough had been observed over Puerto Rico two days earlier and continued northwestward into the Gulf of Mexico.

7.3.1 basic structure

As the radiosonde network expanded to cover parts of Africa and islands in the Caribbean, and as more surface observation sites were established, it became evident that easterly waves generally originate over central and eastern sub-Saharan Africa, and today the waves first documented in the Caribbean and Gulf of Mexico are known as African easterly waves, or "AEWs", which also distinguishes them from westward moving disturbances in the western North Pacific and elsewhere.

Today, a suite of satellite-borne instruments, and contemporary data assimilation techniques allow us to construct detailed analyses of the structure and behavior of AEWs. Figure 7.32 shows the surface structure of an AEW over the central tropical North Atlantic, as depicted by sea-surface scatterometer data (left panel) and ERA5 reanalysis data (right panel). The reanalysis, which assimilates the scatterometer data among other observations, is in good agreement with the scatterometer winds. The westward-moving AEW is marked by a pronounced perturbation in the surface winds, with a pronounced relative vorticity maximum (not shown here) extending from 16°N to 20°N along 42°W. Both the surface wind speed and the

rainfall show pronounced maxima north of the vorticity center, and there is a secondary maximum in rainfall east of the vortex center.

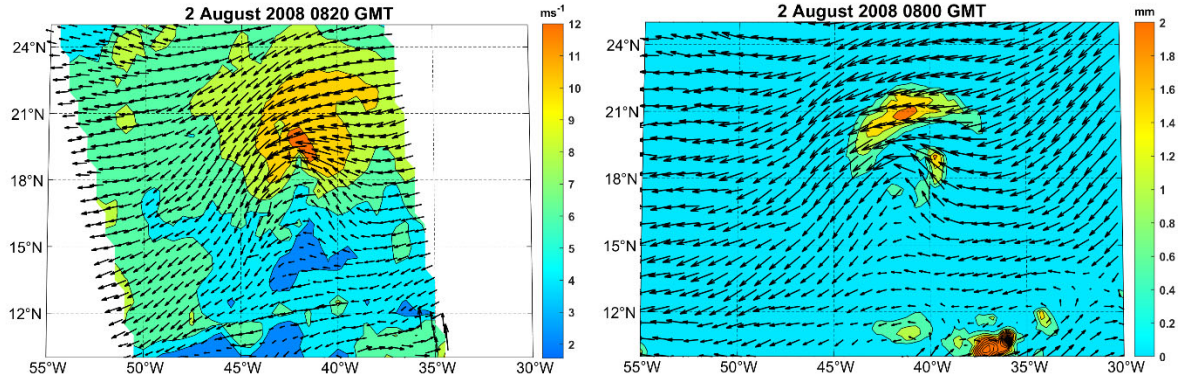

Figure 7.32: An African easterly wave (AEW) over the central tropical North Atlantic on 2 August, 2008, as revealed by sea surface scatterometer winds (left) and in ERA5 reanalysis data (right). The arrows in both panels shows the 10 m wind speed and direction, while the shading in the left panel shows the 10 m wind speed (ms^{-1}) and in the right panel shows the rainfall (mm) over the past hour.

A time-longitude section of outgoing longwave radiation and precipitation, averaged between 7.5ºN and 22.5ºN and extending from western Africa through the far western tropical North Atlantic, is shown in Figure 7.33. The time series spans all of August and September, 2004. A fairly steady progression of AEWS is evident, with periods of 3-5 days and westward migration speeds comparable to those of the low level summertime Trades.

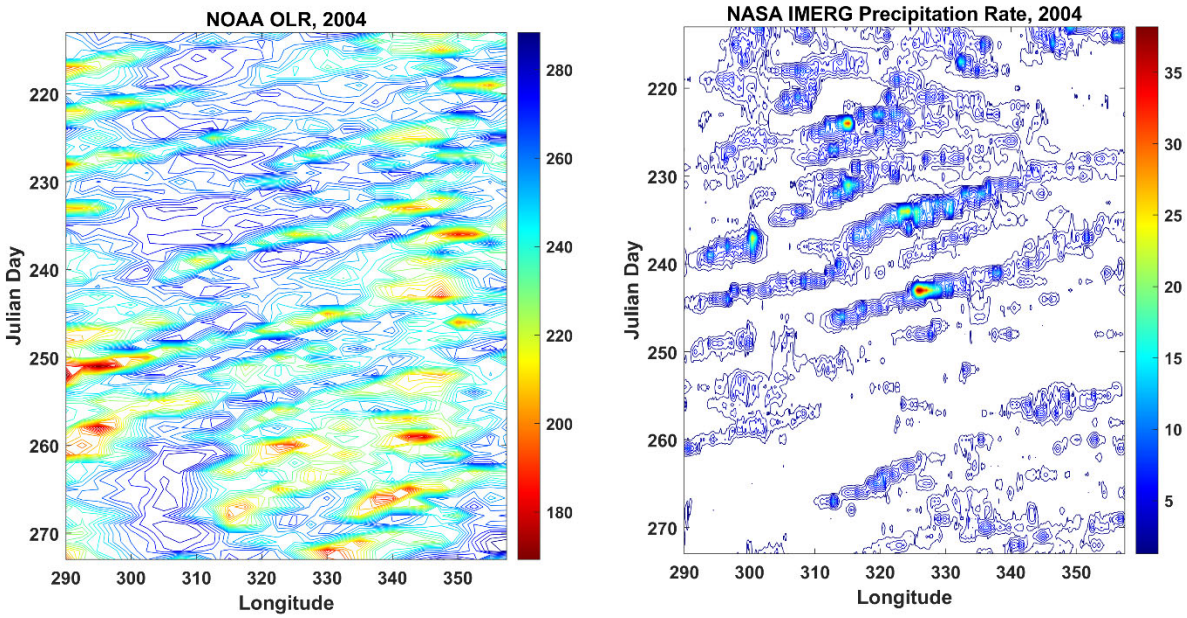

Figure 7.33: Time longitude sections of OLR (left) and precipitation (right) averaged between 7.5ºN and 22.5ºN for August and September, 2004. The sections span the width of the tropical North Atlantic from western Africa eastward to the U.S. coastline.

The vertical structure of AEWs is illustrated in Figure 7.34, constructed using time-lagged analysis of rawinsonde data from Dakar, in Senegal on the extreme western coast of Africa, with the compositing done relative to the time of minimum frequency-filtered OLR in satellite imagery at 12.5ºN, 7.5 ºW (Kiladis et al. 2006).

The peak lower tropospheric easterly wave winds occur between 850 and 500 hPa, and there is a node in the temperature anomalies around 600 hPa; as we shall see, this also corresponds to the altitude of the peak flow in an easterly jet that is present in the Sahel region in summer. As the disturbance center, defined by the OLR minimum, approaches, surface winds are northerly, switching to southerly about a day before the OLR minimum. But note that in the middle troposphere, around 400-700 hPa, the OLR minimum more nearly coincides with the wind shift from northerlies to southerlies. The lower tropospheric meridional winds are strongly correlated with temperature, with high temperatures associated with northerly flow from the Sahara and lower temperatures coinciding with southerly flow from the Gulf of Guinea. The peak cyclonic vorticity in the middle troposphere is ‘cold core’ in the lower troposphere below 600 hPa and warm core in the upper troposphere. In spite of the vertical shears of the meridional winds, there is clearly a strong barotropic component to easterly waves, and like the higher frequency equatorial modes, the vertical temperature structure shows a strong influence of the second baroclinic mode, violating the principle of strict moist adiabaticity.

In contrast with the other fields, the specific humidity anomalies are strongly coherent in the vertical, with little indication of any phase shifts with altitude. This suggests that modulation of deep convection may be the principal direct cause of the humidity anomalies.

7.3.2 Climatology

African easterly wave activity has a strong seasonal cycle, with peak activity in summer. Figure 7.35 shows the eddy kinetic energy over northern Africa and the tropical North Atlantic averaged over the months of July-September 2010-2019 at 700 and 925 hPa. The eddy kinetic energy is defined as the mean square departures of hourly winds at 00 GMT every day from their average values over the period of record. At 700 hPa, there is an east-west oriented local maximum of eddy kinetic energy between 6^{o}N and 12^{o}N extending from the Ethiopian highlands around 30^{o}E to the west coast of the continent, and then continuing into the northeastern Caribbean. This reflects mostly AEW activity at this level. But closer to the surface (bottom panel of Figure 7.35), the largest values of eddy kinetic energy are found much further north, from 18^{o}N to 24^{o}N, in the western Sahel and Sahara. This locus of activity extends southwestward, eventually overlapping with the 700 hPa activity maximum but petering out in the western tropical North Atlantic. This demonstrates the complexity of AEWs, but complexity that has come to be fairly well understood, as well be explained presently.

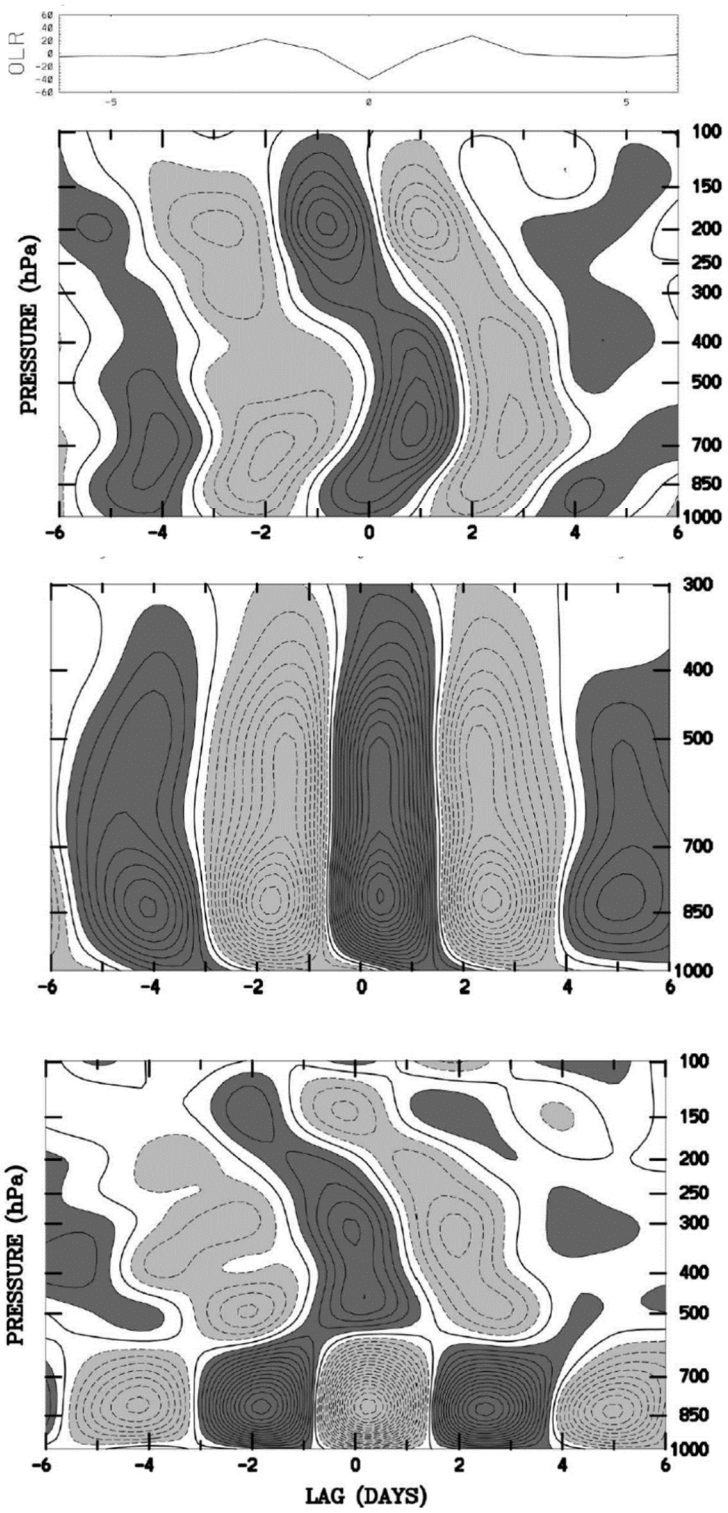

Figure 7.34: Time-lagged composite of radiosonde data at Dakar, with time relative to the minimum OLR at 12.5°N, 7.5 °W. OLR anomaly shown at top. Meridional winds (top), specific humidity (middle) and temperature (bottom), all scaled to a minimum OLR anomaly of 40 Wm^{-2}. Negative values shown by dashed contours. For the meridional wind, the contour interval is 0.5 ms^{-1} with dark (light) shading denoting anomalies greater than (less than) 0.5 ms^{-1}; for specific humidity the contour interval is 0.1 g Kg^{-1}, and for temperature the interval is 0.1 K. Note that the specific humidity plot extends upwards only to 300 hPa.

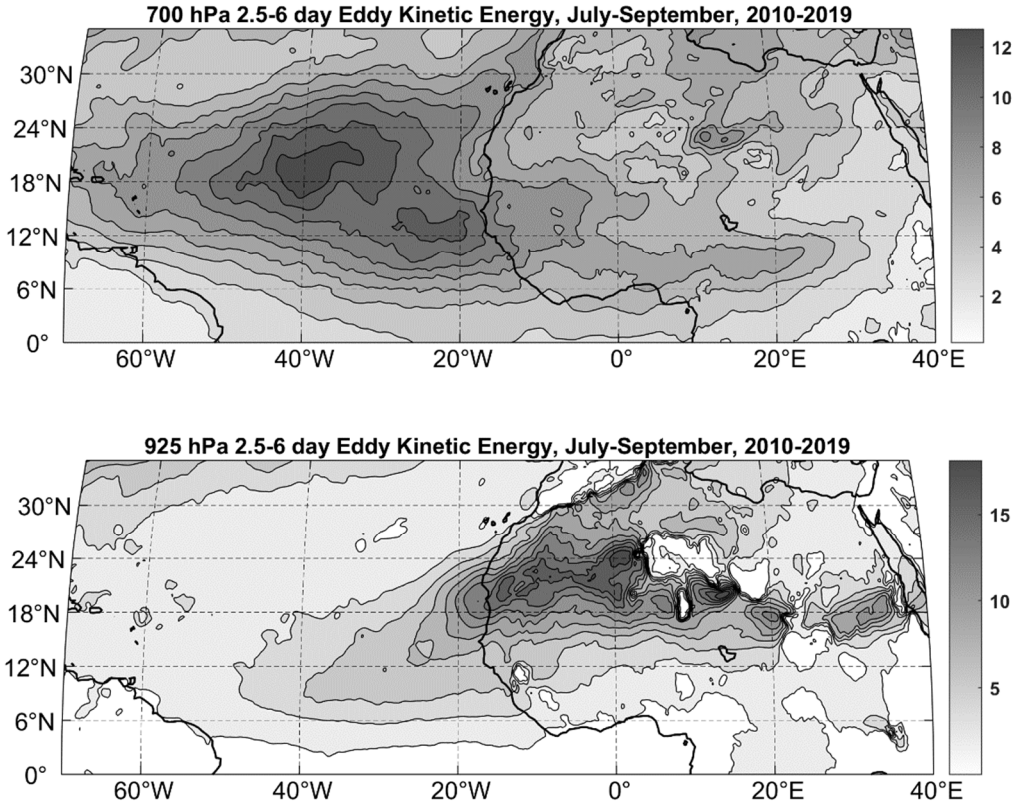

Figure 7.35: Sum of the variances of 2.5-6 day filtered zonal and meridional velocities at 700 hPa (top) and 925 hPa (bottom) averaged over July-September, 2010-2019. The variances represent the departures of hourly 00 GMT velocities from their long-term July-September mean values. From ERA5 reanalyses.

7.3.3 Time-mean background conditions

To understand the dynamics of AEWs, it is first necessary to describe the background summertime flow over northern Africa and the adjacent North Atlantic. The August mean rainfall and 10-m winds in the region are shown in Figure 7.36. A prominent belt of rainfall extends westward from eastern sub-Saharan Africa across the tropical North Atlantic, occupying latitudes from 3°N to 15°N. Over the ocean, this rain belt is marked by the convergence of southerly flow from the southern hemisphere with northeasterly Trades to the north. This circulation may be regarded as part of the solstitial Hadley cell. Over Africa, the southerlies extend much further north into the southern margins of the Sahara, marking the African summer monsoon circulation, driven in part by intense heating over the land. But note that the rain belt does not extend further north over Africa than it does over the ocean. The rain belt over land also coincides with the axis of maximum eddy activity at 700 hPa shown in Figure 7.35. A strong “Azores High” anticyclone dominates the airflow over the North Atlantic at this time of year, and the northeasterlies to the east of the anticyclone center penetrate inland over coastal Africa. A weak cyclonic circulation occupies the norther Sahara, while northerlies off the Mediterranean are found over Libya, Egypt and the Sudan.

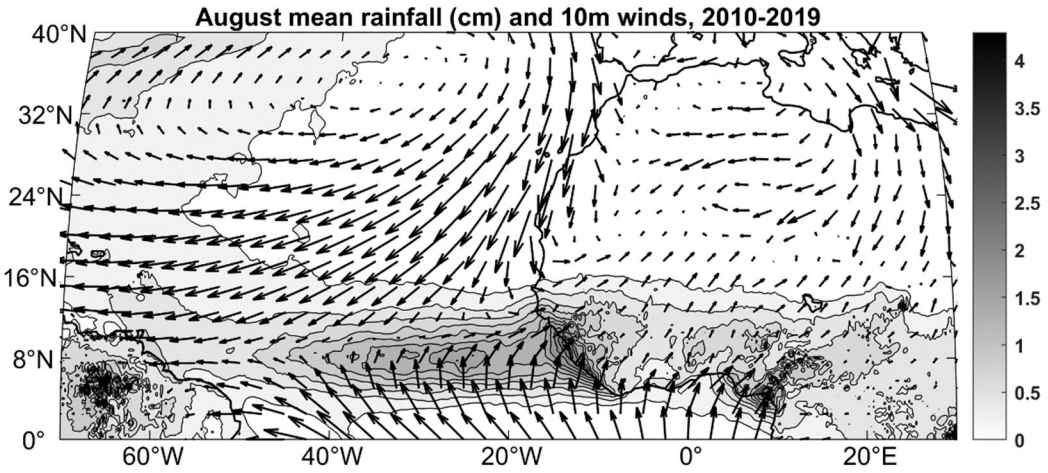

Figure 7.36: August mean rainfall (cm; shaded) and 10-m wind vectors averaged over the period 2010-2019. From ERA5 reanalyses.

Figure 7.37 shows the August mean zonal wind at 700 hPa, averaged over the period 2010-2019 (top) and the 1000 hPa potential temperature and 700 hPa Ertel potential vorticity (bottom). A strong, narrow easterly jet, whose axis lies along 16ºN, extends from far eastern tropical North Africa westward across all of the tropical North Atlantic, reaching peak intensity near the western African coast. The rain belt lies on the cyclonic (southern) flank of this African easterly jet.

The bottom panel of Figure 7.37 shows the distributions of 1000 hPa potential temperature (dashed contours) and 700 hPa Ertel potential vorticity (shading). This diagram will be central to our discussion of AEW dynamics. There is a strong ‘reverse” gradient of low-level potential temperature over sub-Saharan Africa, with temperature increasing northward. From a thermal wind balance perspective, this coincides with the strong easterly zonal wind shear below about 700 hPa. The very dry soils of the Sahara convert all of the absorbed sunlight into sensible heat, leading to very high surface temperatures and dry adiabatic lapse rates that extend as high as 600 hPa in places. Thus, the potential temperature stratification over the Sahara is essentially zero leading to very vanishingly small values of potential vorticity over the desert, clearly visible in the lower panel of Figure 7.37. This in turn leads to an elongated local maximum of potential vorticity that nearly coincides with the rain belt and extends westward to roughly 30ºW. This local potential vorticity maximum is central to the dynamics of AEWs.

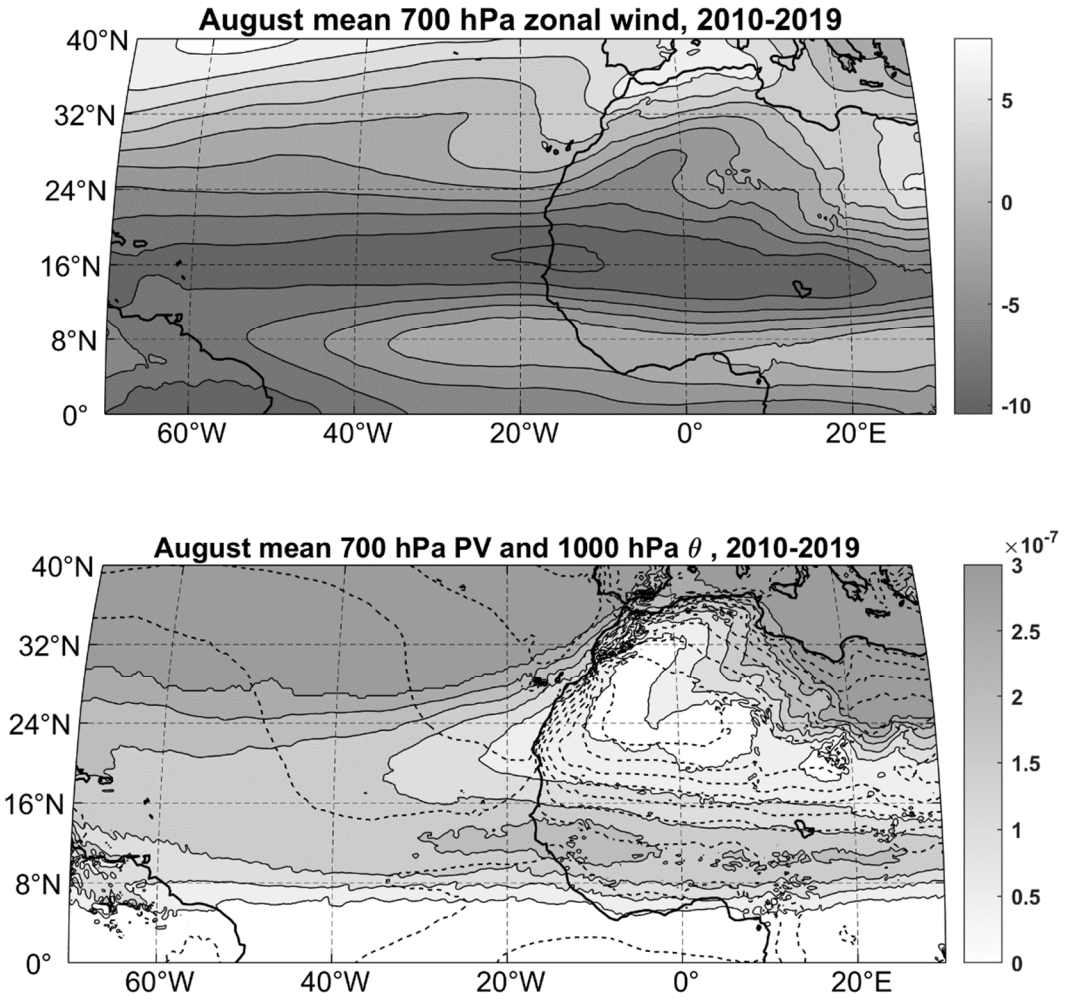

Figure 7.37: August mean 700 hPa zonal wind (ms^{-1}; top) and 700 hPa Ertel potential vorticity ($K\ Kg^{-1}\ m^2\ s^{-1}$; shading) and 1000 hPa potential temperature (K; dashed contours) at bottom. Potential temperature ranges from a minimum of 292 K over the North Atlantic off Portugal to a maximum of 314 K over the northeastern Sahara. Quantities are from ERA5 reanalyses and have been averaged over 2010-2019.

Cross-sections through the August mean climatological state, averaged from 10°W to 20°E and over the period 2010-2019, are shown in Figure 7.38. The African easterly jet is prominent, centered near 15°N and 600 hPa, with another maximum of easterly flow around the tropopause between the equator and 15°N. The mid-latitude westerly jet is in evidence near the northern boundary of the plot. The flow is broadly in thermal wind balance with the potential temperature distribution, which also reveals the region of very low stratification over the Sahara. The latter also shows up as a prominent minimum in the potential vorticity distribution (bottom panel), except very close to the surface where nocturnal cooling contributes to strong stratification in the diurnal average. Note also the strong surface potential temperature gradients between 10°N and 22°N.

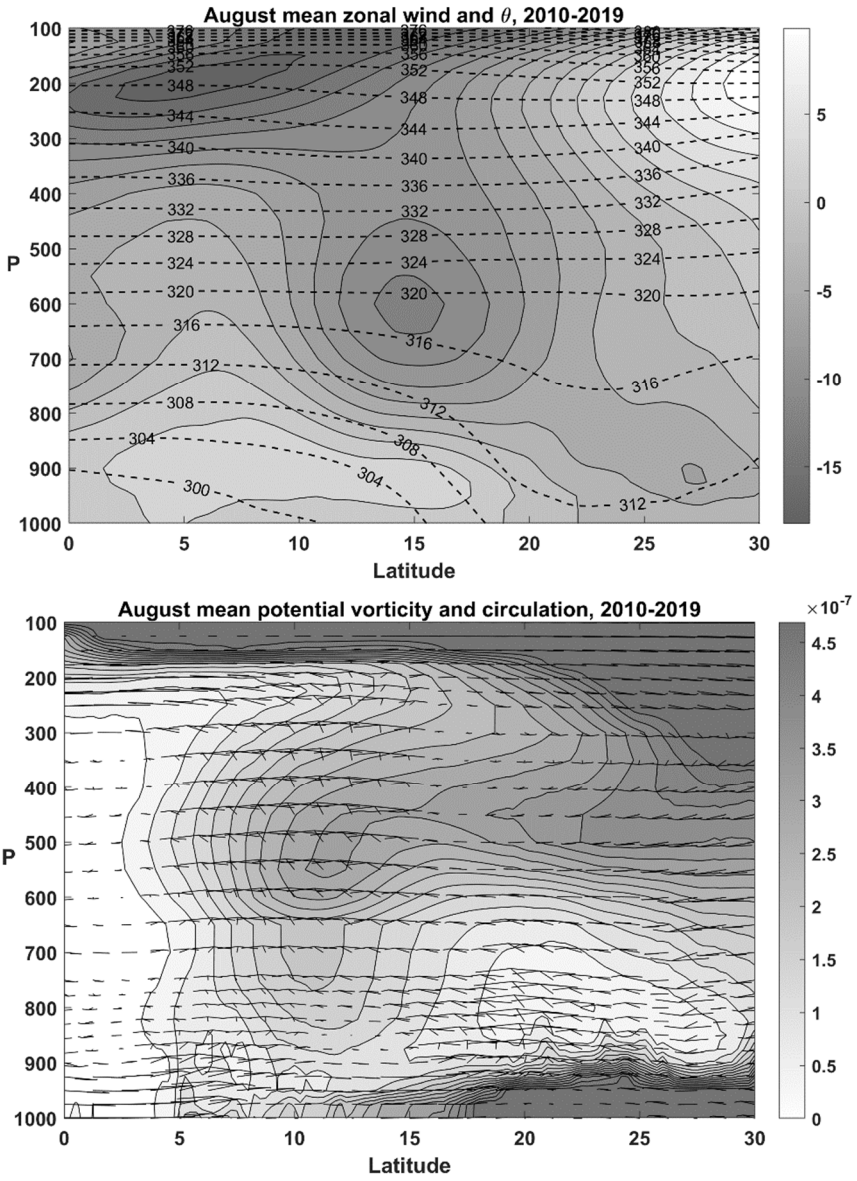

Figure 7.38: Latitude-pressure cross-sections for August mean conditions averaged between 10°W and 20°E and over the period 2010-2019. Top: Zonal wind (ms^{-1}; shading) and potential temperature (K, dashed contours). Bottom: potential vorticity ($K\ Kg^{-1}\ m^2\ s^{-1}$; shading) and vectors showing meridional wind and pressure velocity.

The potential vorticity distribution shows a prominent maximum between 5°N and 15°N, from about 900 hPa up to 500 hPa. Note the reversed potential vorticity gradient between 12°N and 18°N in the lower troposphere, while in the high troposphere the gradient is 'normal'; i.e., potential vorticity increases northward. This implies that the intrinsic (flow-relative) phase speed of Rossby waves in this range of latitude is eastward in the lower troposphere and westward in the high troposphere.

Also shown in the bottom panel of Figure 7.38 is the time-mean circulation in the latitude-pressure plane. Strong, northward monsoonal flow is evident below 900 hPa from the equator all the way up to about 20°N, with strong convergence in the rain belt around 5°N to 15°N and also between 20°N and 25°N. This leads to strong upward motion in the rain belt, especially in

the upper troposphere, and to ascent up to about 700 hPa over the Sahara. The latter ascent region is not associated with rainfall, owing to the extreme dryness of the air in this region. Much of the ascending air returns southward in the 850-700 hPa layer; this shallow, dry circulation may be thought of as a local monsoonal flow responding to the steep temperature gradient resulting from large surface sensible heat fluxes from the desert floor.

7.3.4 AEW dynamics

African easterly waves are thought to result from a barotropic/baroclinic instability of the summertime mean state of the atmosphere over the Sahel. This instability arises from the interaction of sets Rossby waves that have opposite intrinsic phase speeds but are Doppler shifted by the mean flow in such a way that they may lock phases and amplify each other. The basic dynamics of barotropic and baroclinic instabilities is nicely summarized in Hoskins et al. (1985) and Hoskins and James (2014). Here we review an important result, the "Charney-Stern Theorem" (Charney and Stern 1962), which sets necessary (but no sufficient) conditions for steady, zonal flows to be unstable to normal mode disturbances whose intrinsic time scales are sufficiently slow that they may be considered quasi-geostrophic.

Quasi-geostrophy is founded on the basic principle of conservation of a quantity, the pseudo-potential vorticity, q_p, that is conserved following the geostrophic (not actual) wind. For quasi-geostrophic flows in the absence of friction of heating[6], this conservation principle may be written in pressure coordinates:

$$\left(\frac{\partial}{\partial t}+\mathbf{V}_g\bullet\nabla\right)q_p=0, \tag{7.17}$$

where $\mathbf{V}_g$ is the geostrophic wind and q_p is a function of a single variable, the geopotential φ:

$$q_p=\frac{1}{f_0}\nabla^2\varphi+\beta y+f_0\frac{\partial}{\partial p}\left(\frac{1}{S}\frac{\partial\varphi}{\partial p}\right), \tag{7.18}$$

where f_0 is a constant Coriolis parameter evaluated at a central latitude, β is a constant latitudinal gradient of the Coriolis parameter at the central latitude, and S is a background static stability that can be, as most, a function of pressure:

$$S(p)\equiv-\frac{\overline{\alpha}}{\overline{\theta}}\frac{d\overline{\theta}}{dp}, \tag{7.19}$$

in which the overbars refer to the mean state and α is specific volume. Since the geostrophic wind (in (7.17)) is also just a function of φ, (7.17) is a closed, nonlinear expression provided appropriate boundary conditions are supplied.

[6] Real AEWs are strongly affected by latent heating, but it is not clear that this heating is essential to their existence. Here, as a first look at the problem, we will neglect it.

The Charney-Stern Theorem address the stability of a steady, specified, balanced background flow that varies only in pressure and latitude to infinitesimal perturbations that may vary in all three spatial dimensions and time. Denoting these perturbations by primes and the background state by overbars, we express all the variables as

$$\begin{aligned} \varphi &= \overline{\varphi}(y,p) + \varphi'(x,y,p,t), \\ \mathbf{V}_g &= \overline{u}(y,p)\hat{i} + \mathbf{V}_g'(x,y,p,t), \\ q_p &= \overline{q}_p(y,p) + q_p'(x,y,p,t). \end{aligned} \tag{7.20}$$

Substituting (7.21) into (7.17), using (7.18), and dropping terms that are quadratic in the perturbation variables gives

$$\left(\frac{\partial}{\partial t} + \overline{u}\frac{\partial}{\partial x}\right)\left[\frac{1}{f_0}\nabla^2\varphi' + f_0\frac{\partial}{\partial p}\left(\frac{1}{S}\frac{\partial\varphi'}{\partial p}\right)\right] + v_g'\frac{\partial\overline{q}_p}{\partial y} = 0. \tag{7.21}$$

Here $v_g' = \frac{1}{f_0}\frac{\partial\varphi'}{\partial x}$ is the meridional component of the perturbation geostrophic wind. Note the importance of the meridional gradient of the background pseudo-potential vorticity, that appears in the last term in (7.21).

Charney and Stern were interested in modal solutions[7] to (7.21), of the form

$$\varphi' = \Phi(y,p)e^{ik(x-ct)}, \tag{7.22}$$

where Φ is a complex function of y and p, and c is a complex phase speed. (If c has a positive imaginary part, this corresponds to solutions that grow exponentially in time.) Substituting (7.22) into (7.21) gives

$$\frac{\partial^2\Phi}{\partial y^2} + f_0^2\frac{\partial}{\partial p}\left(\frac{1}{S}\frac{\partial\Phi}{\partial p}\right) + \Phi\left(\frac{\partial\overline{q}_p/\partial y}{\overline{u}-c} - k^2\right) = 0. \tag{7.23}$$

Given suitable boundary conditions together with self-consistent distributions of $\partial\overline{q}_p/\partial y$, $\overline{u}$, and $S(p)$, (7.23) can, in principle, be solved for the eigenvalues c and associated eigenfunctions. But Charney and Stern sought instead to derive certain constraints on any normal mode instabilities that might develop in general background states. They did this through a procedure in which (7.23) is first multiplied through by the complex conjugate of Φ, Φ^*, and then integrated over a domain that is infinite in y but bounded above and below by rigid plates as specified pressures p_0 and p_1, which might here be thought of as the surface and the tropopause:

[7] Note that in this problem, the normal modes are not 'complete'; i.e., a disturbance of arbitrary shape cannot in general be expressed as a weighted sum of the normal modes. The parts of any initial perturbation that do not project onto normal modes may nevertheless grow rapidly but transiently and are the subject of a large body of published literature (e.g. Farrell 1984).

$$\int_{-\infty}^{\infty}\int_{p_1}^{p_0}\left[\Phi^*\frac{\partial^2\Phi}{\partial y^2}+f_0^2\Phi^*\frac{\partial}{\partial p}\left(\frac{1}{S}\frac{\partial\Phi}{\partial p}\right)+|\Phi|^2\left(\frac{\partial\overline{q}_p}{\partial y}\frac{1}{\overline{u}-c}-k^2\right)\right]dpdy=0. \tag{7.24}$$

Next, we integrate the first two terms by parts. In doing so, we assume that the disturbances decay toward $y=\pm\infty$, but we do not assume that disturbances vanish on the top and bottom boundaries. The result is

$$\begin{aligned}\int_{-\infty}^{\infty}\int_{p_1}^{p_0}\left\{\left|\frac{\partial\Phi}{\partial y}\right|^2+\left(k^2-\frac{\partial\overline{q}_p/\partial y}{\overline{u}-c}\right)|\Phi|^2+\frac{f_0^2}{S}\left|\frac{\partial\Phi}{\partial p}\right|^2\right\}dydp\\ +f_0^2\int_{-\infty}^{\infty}\left[\frac{\Phi^*}{S}\frac{\partial\Phi}{\partial p}\right]\Big|_{p_1}^{p_0}dy=0.\end{aligned} \tag{7.25}$$

The last term is evaluated in the upper and lower boundaries. If there are any mean state potential temperature gradients on either boundary, they can potentially be advected by the perturbation flow at the boundaries, giving rise to temperature perturbations, and, through the hydrostatic condition, to geopotential perturbations. Thus, we must use dynamical boundary conditions on potential temperature θ:

$$\left(\frac{\partial}{\partial t}+\mathbf{V}_g\bullet\nabla\right)\theta=0\quad\text{on}\ \ p=p_0,p_1 \tag{7.26}$$

There is no vertical advection on the boundaries as they are considered rigid and horizontal. Linearizing as before, using (7.20), and making use of the hydrostatic equation

$$\frac{\partial\varphi'}{\partial p}=-\frac{\overline{\alpha}}{\overline{\theta}}\theta'$$

and substituting (7.22) allows to write the linearized version on (7.26) as

$$\frac{\partial\Phi}{\partial p}-\frac{\overline{\alpha}}{f_0\overline{\theta}(\overline{u}-c)}\frac{\partial\overline{\theta}}{\partial y}\Phi=0\quad\text{on}\ \ p=p_0,p_1. \tag{7.27}$$

We substitute this into the last term in (7.25) to arrive at

$$\begin{aligned}\int_{-\infty}^{\infty}\int_{p_1}^{p_0}\left(\left|\frac{\partial\Phi}{\partial y}\right|^2+\left(k^2-\frac{\partial\overline{q}_p/\partial y}{\overline{u}-c}\right)|\Phi|^2+\frac{f_0^2}{S}\left|\frac{\partial\Phi}{\partial p}\right|^2\right)dpdy\\ -\int_{-\infty}^{\infty}\left(\frac{\overline{\alpha}f_0\dfrac{\partial\overline{\theta}}{\partial y}}{\overline{\theta}S(\overline{u}-c)}\right)|\Phi|^2\Big|_{p_1}^{p_0}dy=0.\end{aligned} \tag{7.28}$$

We can simplify the notation in (7.28) by defining a new quantity Q_y:

$$Q_y \equiv \frac{\partial q_p}{\partial y} + \frac{\overline{\alpha} f_0}{\overline{\theta} S} \frac{\partial \overline{\theta}}{\partial y} \left[\delta(p_0 - p) - \delta(p - p_1) \right], \tag{7.29}$$

where δ is the Dirac delta function. With this definition, (7.28) may be written more compactly as

$$\int_{-\infty}^{\infty} \int_{p_1}^{p_0} \left(\left| \frac{\partial \Phi}{\partial y} \right|^2 + \left(k^2 - \frac{Q_y}{\overline{u} - c} \right) |\Phi|^2 + \frac{f_0^2}{S} \left| \frac{\partial \Phi}{\partial p} \right|^2 \right) dp dy = 0 \tag{7.30}$$

The quantity Q_y is a generalized pseudo potential vorticity gradient, with potential temperature gradients on the lower and upper boundaries acting like delta functions of positive and negative potential vorticity gradients, respectively.

Because c is, in general, a complex number, the real and imaginary parts of (7.30) must be individually satisfied. In particular, the imaginary part of (7.30) is

$$c_i \int_{-\infty}^{\infty} \int_{p_1}^{p_0} \left(\frac{Q_y}{|\overline{u} - c|^2} |\Phi|^2 \right) dp dy = 0, \tag{7.31}$$

where c_i is the imaginary part of the phase speed; positive for exponentially growing solutions. For (7.31) to be satisfied, either the solutions cannot be growing or decaying exponentially $(c_i = 0)$, or the effective gradient of pseudo potential vorticity, Q_y, must change sign at least once within the domain. Referring to its definition, (7.29), one or more of the following must be true:

1. The meridional gradient of pseudo-potential vorticity, $\partial \overline{q}_p / \partial y$, changes sign in the domain;
2. The meridional temperature gradient, $\partial \overline{\theta} / \partial y$, changes sign along one or both boundaries;
3. The meridional temperature gradient, $\partial \overline{\theta} / \partial y$, at the lower boundary (p_0) has the same sign as $\partial \overline{\theta} / \partial y$ at the upper boundary (p_1) and/or the opposite sign of the interior pseudo potential vorticity gradient, $\partial \overline{q}_p / \partial y$;
4. The meridional temperature gradient, $\partial \overline{\theta} / \partial y$, at the upper boundary (p_1) has the same sign as either or both the meridional temperature gradient at the lower boundary (p_0) and the interior potential vorticity gradient.

Equation (7.31) forms the core of the Charney-Stern theorem. In the classical Charney problem of baroclinic instability, (Charney 1947), $\partial \overline{q}_p / \partial y$ is taken to be a positive constant in the troposphere, while $\partial \overline{\theta} / \partial y$ is negative at the surface and the atmosphere is unbounded in the vertical. Thus Q_y , as given by (7.29), changes sign in the domain and the necessary (but no

sufficient) condition for instability is satisfied. In fact, the linear stability analysis does turn up unstable modes with the structure and scale of observed baroclinic waves. In the also classical Eady linear stability analysis (Eady 1949), $\partial \overline{q}_p / \partial y$ is taken to be zero everywhere, and $\partial \overline{\theta} / \partial y$ is constant with the same value on both boundaries. Once again, Q_y changes sign within the domain and Eady's analysis does show a rich spectrum of unstable modes, with reasonable structure and length and time scales.

Taking the real part of (7.30) also provides a useful constraint:

$$\int_{-\infty}^{\infty}\int_{p_1}^{p_0}\left(\left|\frac{\partial\Phi}{\partial y}\right|^2+\left(k^2-\frac{(\overline{u}-c_r)Q_y}{|\overline{u}-c|^2}\right)|\Phi|^2+\frac{f_0^2}{S}\left|\frac{\partial\Phi}{\partial p}\right|^2\right)dpdy=0, \tag{7.32}$$

where c_r is the real part of the phase speed. Whether the solutions are growing, decaying, or neutral, (7.32) must be satisfied. Now for growing (or decaying) solutions $(c_i \neq 0)$, we are free to add any constant multiple of the double integral in (7.31) to (7.32), since the former vanishes. We choose the multiplier to be c_r, and subtracting the result from (7.32) gives

$$\int_{-\infty}^{\infty}\int_{p_1}^{p_0}\left(\left|\frac{\partial\Phi}{\partial y}\right|^2+\left(k^2-\frac{\overline{u}Q_y}{|\overline{u}-c|^2}\right)|\Phi|^2+\frac{f_0^2}{S}\left|\frac{\partial\Phi}{\partial p}\right|^2\right)dpdy=0. \tag{7.33}$$

Thus another constraint that exponentially growing solutions must satisfy is that $\overline{u}$ and Q_y must be positively correlated. This is a variation on a theorem by Ragnar Fjørtoft (Fjørtoft 1950).

There is a nice, straightforward interpretation of the Charney-Stern and Fjørtoft theorems. It stems from the recognition that Q_y serves as a refractive index for Rossby waves. The intrinsic (flow-relative) phase speed of such waves is the opposite sign of Q_y, so that on earth, where Q_y is usually positive in the free troposphere, Rossby waves propagate westward relative to the flow. Thus the requirement, from (7.31), that Q_y change sign is a requirement that the intrinsic phase speed of Rossby waves have both signs (we might refer to this as having to have two different 'flavors' of Rossby wave interacting). The condition (7.33) that $\overline{u}$ and Q_y be positively correlated can be interpreted to mean that the Doppler shifting of the two flavors of Rossby wave must be such as to make it possible for them to phase lock: the westward flavor waves $(Q_y > 0)$ must be Doppler shifted eastward, and/or the eastward flavor waves $(Q_y < 0)$ must be Doppler shifted westward.

In the classical Charney baroclinic instability problem, the two flavors consist of intrinsic westward-propagating internal Rossby waves in the troposphere, where $Q_y > 0$ and intrinsic eastward propagating waves on the surface delta function. (These latter decay exponentially away from the surface and are known as "Eady edge waves".) The increasing westerlies with

altitude Doppler shift the internal Rossby waves eastward so that they potentially phase lock with the surface Eady edge wave, and in fact do phase lock in the unstable models.

In the classical Eady baroclinic instability problem, there are no internal Rossby waves, since Q_y is zero in the free troposphere, but there are two flavors of Eady edge wave: A surface wave with intrinsic easterly phase speed, and a tropopause edge wave with intrinsic westerly phase speed. The increasing westerly wind with altitude Doppler shifts the edge waves so that they can phase lock, and do so in the unstable modes first found by Eady.

Armed with the Charney-Stern and Fjørtoft theorems, we can now analyze whether the mean state over North Africa in summer may be subject to baroclinic/barotropic instability.

First the bottom panels of Figures 7.37 and 7.38 show that the internal meridional gradient of potential vorticity (assumed to be similar to that of the pseudo-potential vorticity) changes sign across the axis of the mid-level easterly get. Moreover, it is clear from the top panels of these two figures that the strong easterlies north of the axis of maximum potential vorticity can Doppler shift the intrinsic eastward propagating internal Rossby waves westward relative to the intrinsically westward propagating internal Rossby waves south of the axis of maximum potential vorticity. The potentially unstable interaction of these two flavors of internal Rossby waves on either side of the axis of maximum potential vorticity would normally be called barotropic instability as it need not involve temperature perturbations[8]. It is believed that this interaction is the main source of wave energy in the genesis region of AEWs in eastern and central sub-Saharan Africa, as indicated by the strip of high eddy kinetic energy at 700 hPa top part of Figure 7.35) near the axis of maximum potential vorticity.

Next, examine the bottom panel of Figure 7.38. Note that between 10^{o}N and 20^{o}N, the interior meridional potential vorticity gradient switches from negative to positive going from the lower to the upper troposphere. (There is a second reversal below 900 hPa, but that is strictly nocturnal, resulting from surface radiative cooling at night, and a night is too short to engender instabilities like these, with time scales of several days.) So we have two flavors of Rossby wave: intrinsic eastward propagation in the lower troposphere, and westward in the upper troposphere. But examination of the zonal flow (upper panel of Figure .38) shows that what little Doppler shifting exists is in the wrong direction, acting to increase the difference in actual phase speeds, so we do not expect this to be a source of wave growth.

Finally, examine the bottom panel of Figure 7.37. Note that across all of Africa, but not west of the coastline, the 700 hPa potential vorticity gradient is negative and the surface potential temperature gradient is positive roughly between 10^{o}N and 24^{o}N. This means that there are intrinsic eastward-propagating internal Rossby waves in the lower troposphere, and intrinsic westward-propagating Eady edge waves at the surface. This time, the strong easterly low-level shear Doppler shifts the two flavors of Rossby waves so that they can potentially phase lock and amplify each other…both the Charney-Stern and Fjørtoft necessary conditions are satisfied. (This is the classical Charney problem upside down!) Now refer back to the bottom panel of Figure 7.35: This unstable interaction is probably the source of all the low-level eddy kinetic

[8] The Charney-Stern and Fjørtoft theorems are silent about any distinction between barotropic and baroclinic instability. Indeed, while the energetics shift with the relative orientations of the two flavors of Rossby wave, the dynamics are the same, and thus there is little reason to make a distinction between barotropic and baroclinic instability. Here we treat them as one and the same.

energy between 10ºN and 24ºN in western Africa as well as some of the eddy kinetic energy at 700 hPa west of the Greenwich meridian (top panel of Figure 7.35).

Thus it appears that there are two main sources of African easterly wave activity: unstable interaction of two flavors of internal Rossby wave across the axis of maximum potential vorticity in the lower to middle troposphere, extending across sub-Saharan Africa, and interaction of the northern member of this pair with surface Eady edge waves living on the strong northward gradient of potential temperature at the surface. This is perhaps why there are two distinct wave trains over Africa, which merge near the western coastline.

7.3.5. Case study with dynamical interpretation

Let's examine a particular AEW that developed during late July and early August, 2008, tracing back in time from its state as depicted in Figure 7.32. The left-hand columns of Figures 7.39-7.40 show the 700 hPa winds and potential vorticity (PV), while the right-hand columns show 1000 hPa winds and potential temperature. These charts have been created from hourly ERA5 reanalysis data at 00 GMT over the period 27 July – 1 August 2008.

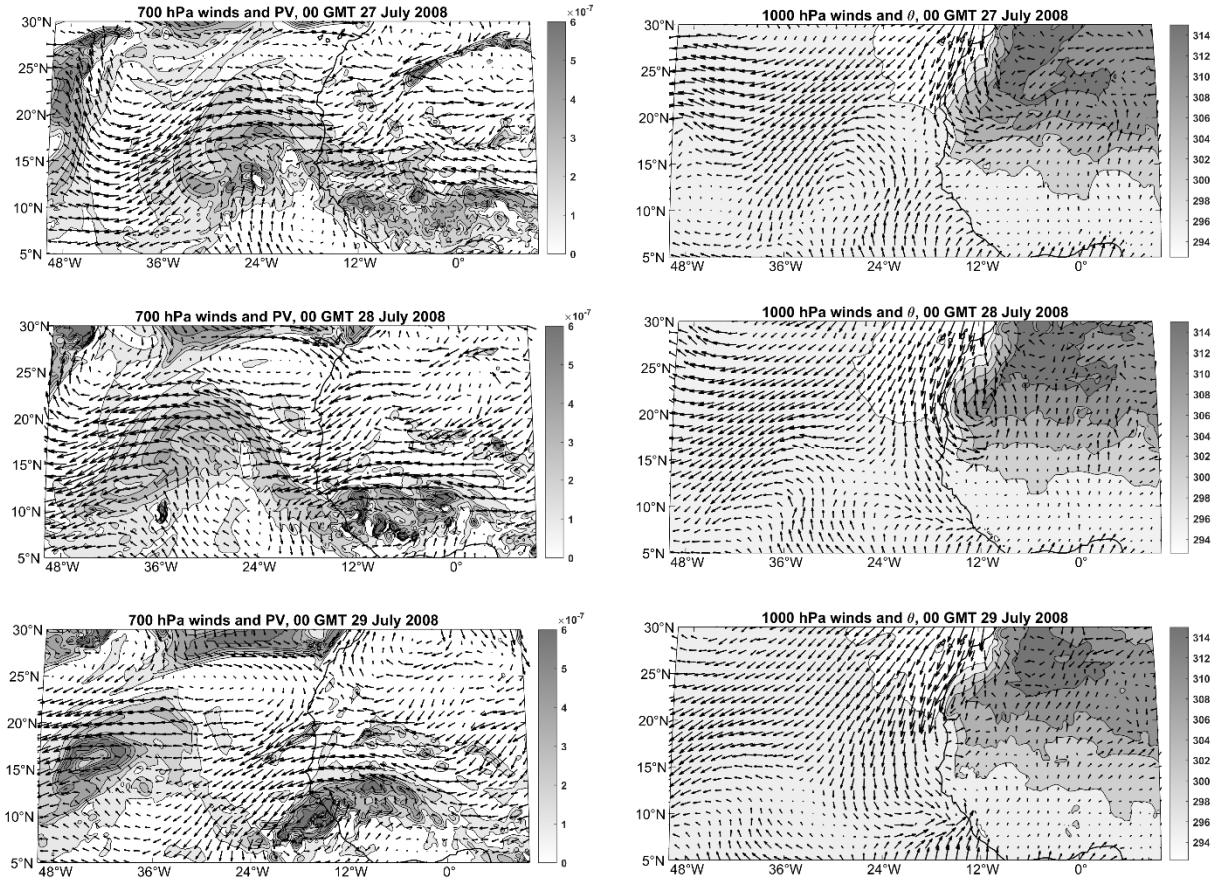

Figure 7.39: 700 hPa winds and potential vorticity (K Kg^{-1} m^2 s^{-1}; left column) and 1000 hPa winds and potential temperature (K; right column) at 00 GMT on July 27 – 29 2008, from ERA5 reanalyses.

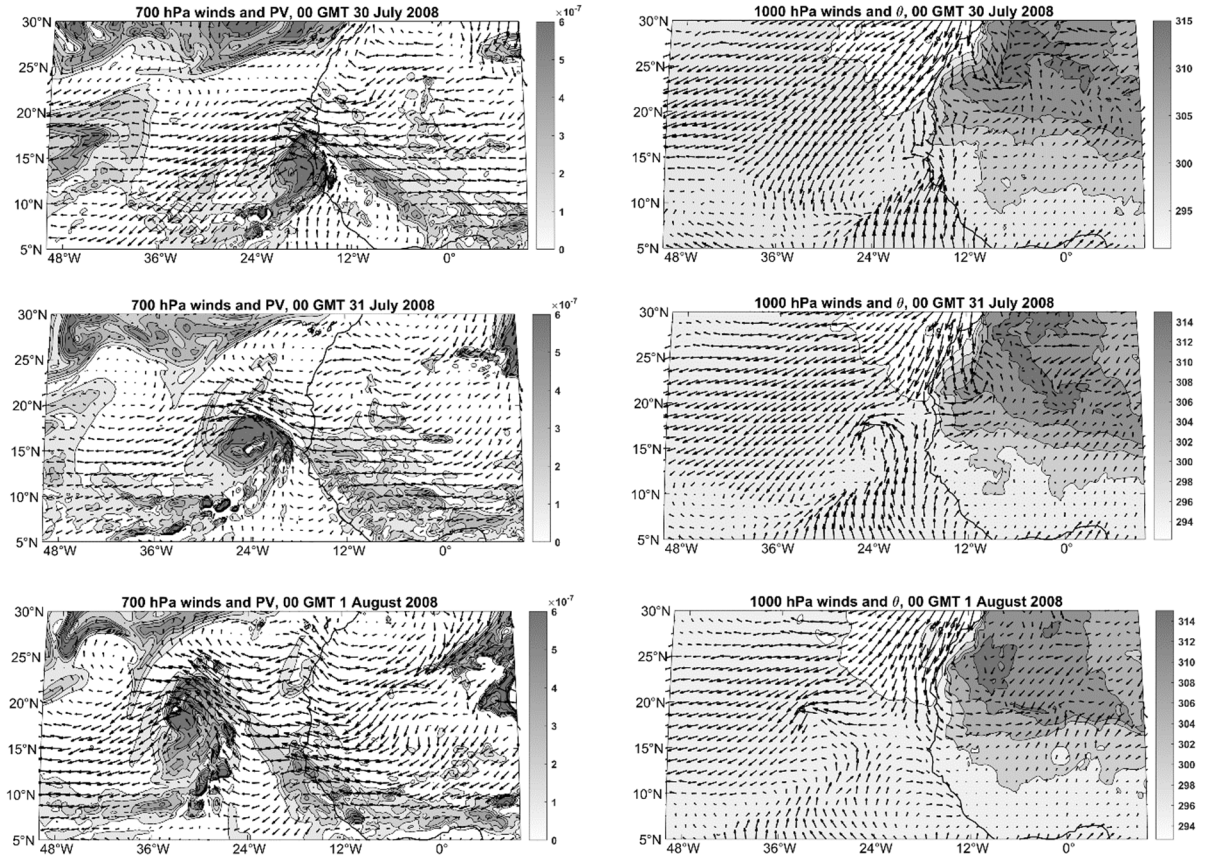

Figure 7.40: 700 hPa winds and potential vorticity (K Kg^{-1} m^2 s^{-1}; left column) and 1000 hPa winds and potential temperature (K; right column) at 00 GMT on July 30 – August 1 2008, from ERA5 reanalyses.

On July 27th (top row of Figure 7.39) one can see two AEWs at 700 hPa over the Atlantic, with strong signatures in the winds at both 700 hPa and 1000 hPa (right column). But focus on the western coastal region of Africa and note the high values of PV there, in keeping with the long-term summer climatology (bottom panel of Figure 7.37). Also notice the anomalously high PV around 8^{o}W and 10^{o}N – 15^{o}N, as well as some fragments of high PV to the northeast; these are associated with a pronounced cyclonic circulation extending to 20^{o}N. This circulation projects down to the surface (upper left panel of Figure 7.39) where it is exciting an Eady edge wave on the pronounced northerly potential temperature gradient at 1000 hPa. But note that there is little or no circulation at 1000 hPa underneath the 700 hPa high potential vorticity strip near the coast.

By the next day (middle row of Figure 7.39), a strong circulation is beginning to consolidate around 10^{o}W and there continues to be a strong cyclonic circulation around 10^{o}W and 17^{o}N. associated with the fragmented positive PV anomalies which have also moved westward. To its west, at the surface, the Easy edge wave has intensified and moved southwest from its location a day earlier. On the 29th of July (bottom panel of Figure 7.39) the PV at 700 hPa has further consolidated into a more nearly circular mass centered just offshore at around 14^{o}W , 10^{o}N, and the cyclonic circulation around it, obvious at 700 hPa, extends down to the surface where there

is now a prominent cyclonic circulation. Meanwhile, the Eady edge wave to the north is beginning to dissipate, having run out of 1000 hPa temperature gradient at the coast.

By the 30th of July (top row of Figure 7.40) the 700 hPa PV is gathered into a quite circular mass with a strong manifestation at the surface. The larger peak values of PV may be owing to diabatic process such as radiative heating under the thick deep clouds associated with this AEW. There is now a strong manifestation at the surface, with a pronounced cyclonic trough extending southwest from the African coast. The absence now of any appreciable surface potential temperature anomalies suggests that the edge wave dynamics are no longer playing any role.

The rest of Figure 7.40 documents the westward migration of the AEW, whose maximum surface manifestation is around July 31st. It is important to notice that only in its early evolution can the AEW be considered a to involve wave dynamics. Certainly by the 31st of July the AEW is far better characterized as an isolated maximum of PV in the lower to middle troposphere, just being carried westward with the Trades. In no dynamical sense is it a wave at all. Perhaps AEWs should instead be referred to as African Easterly Vortices (AEVs). This is also why the disturbances can be easily tracked across the Atlantic; were they Rossby waves they would be highly dispersive and not trackable beyond a wavelength or two.

7.4 Easterly waves over the eastern North Pacific

Westward-propagating disturbances with dimensions and time scales comparable to those of African easterly waves are observed over the tropical eastern North Pacific, west of Central America and Mexico. An example of such a wave is shown in Figure 7.41.

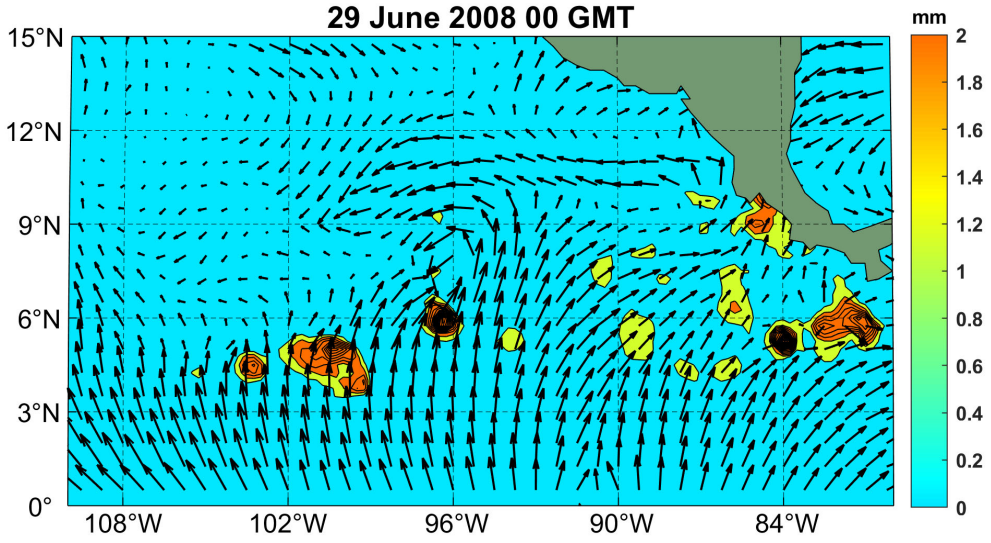

Figure 7.41: 10 m winds (arrows) and hourly precipitation amount (mm, shading) at 00 GMT on 29 June, 2008, from ERA-5 reanalyses.

The surface circulation is centered near 8ºN, 96ºW, and there are broken patches of rainfall along the eastern North Pacific ITCZ. At this particular time, there is not much rainfall associated with the wave in the easterlies. We shall examine the evolution of this particular event in greater detail later in this section.

Time-longitude sections (Figure 7.42) show a regular progression westward-propagating of OLR and precipitation anomalies, similar to AEWs (Figure 7.33). The disturbances move at around 6 ms^{-1} and with a period of a few days, corresponding to a wavelength of 1,000-3,000 km. But, as is the case with AEWs, by the time these perturbations are well offshore, they are closed vortices and do not behave dynamically like waves.

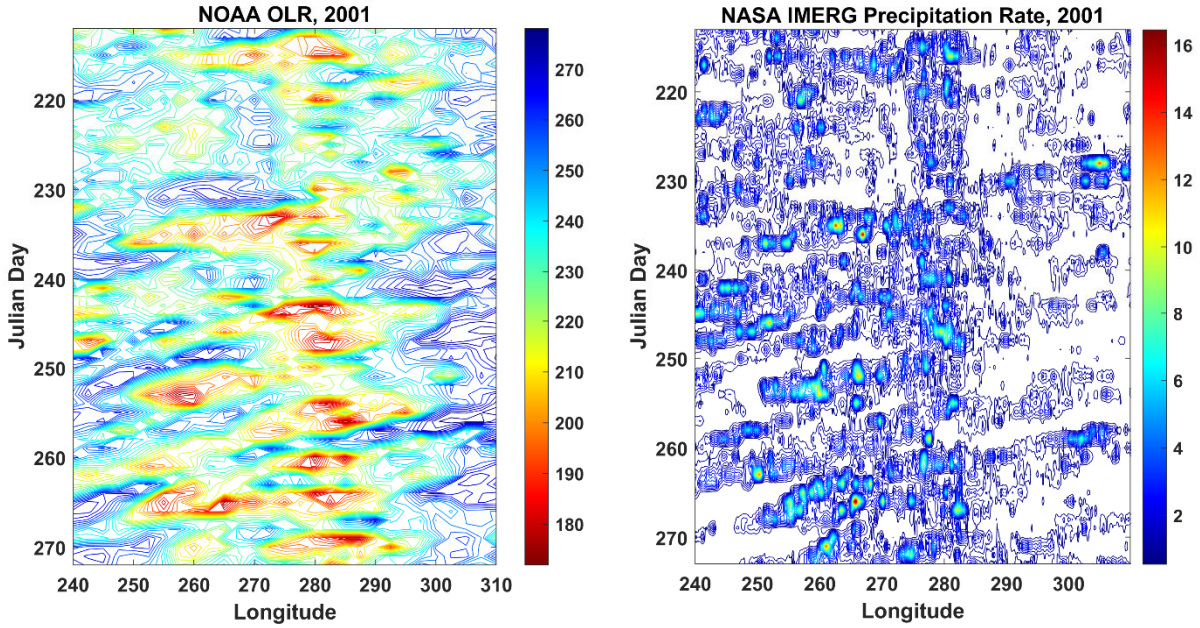

Figure 7.42: Time longitude sections of OLR (left) and precipitation (right) averaged between 5ºN and 15ºN for August and September, 2001. The sections span the tropical eastern North Pacific from 120ºW to 60ºW.

The climatological track density of easterly waves over both the North Atlantic and eastern North Pacific is shown in Figure 7.43. The tracks were computed from frequency-filtered vorticity at 850, 700, and 600 hPa from ERA-Interim reanalyses from 1998-2013, applying criterion for direction of motion, vorticity magnitude, and other criteria as described in details in Dominguez et al. (2020). Although the belt of high activity is continuous across the tropical North Atlantic Central America, and the eastern North Pacific, there is a clear maximum of track density in the far eastern North Pacific west of Central America.

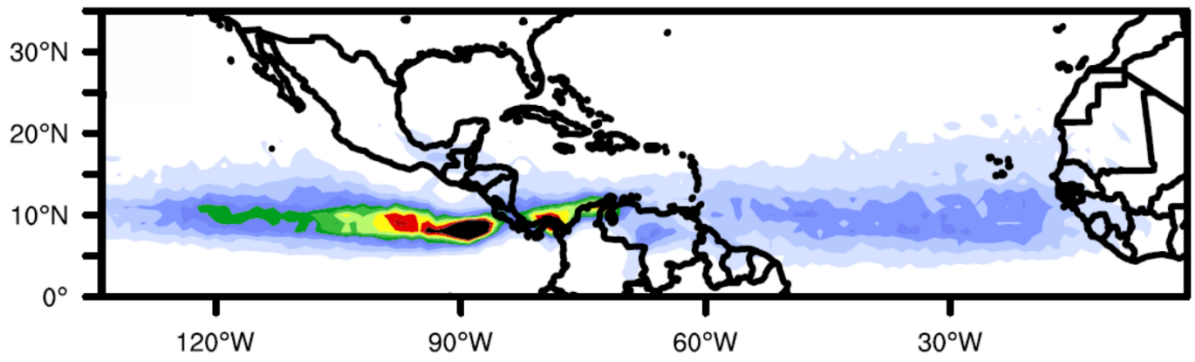

Figure 7.43: Track density of easterly waves, from reanalysis data. See text for description of tracking method.

The climatological distribution of near-surface winds and precipitation during the month of July is displayed in Figure 7.44. Low-level conditions differ dramatically between the Caribbean region and the eastern North Pacific. Strong low-level easterlies dominate the Caribbean Sea in July, with almost no rain, while the eastern Pacific has a prominent ITCZ extending from 5°N to 10°N. The airflow within and south of the ITCZ is from the south, with very light surface winds to the north, giving way to northeasterly Trades in the western portion of the domain. Note also the high rainfall over the Andes and just west of Lake Maracaibo in northern Venezuela; there is also intense convective rainfall over Panama and Costa Rica.

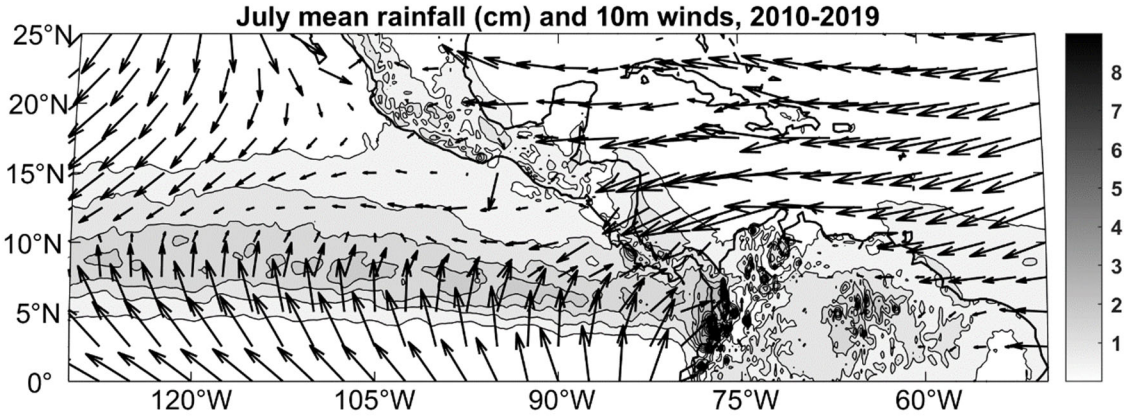

Figure 7.44: July mean surface (10m) winds (arrows) and rainfall (cm; shading) averaged over 2010-2019 from ERA-5 reanalyses.

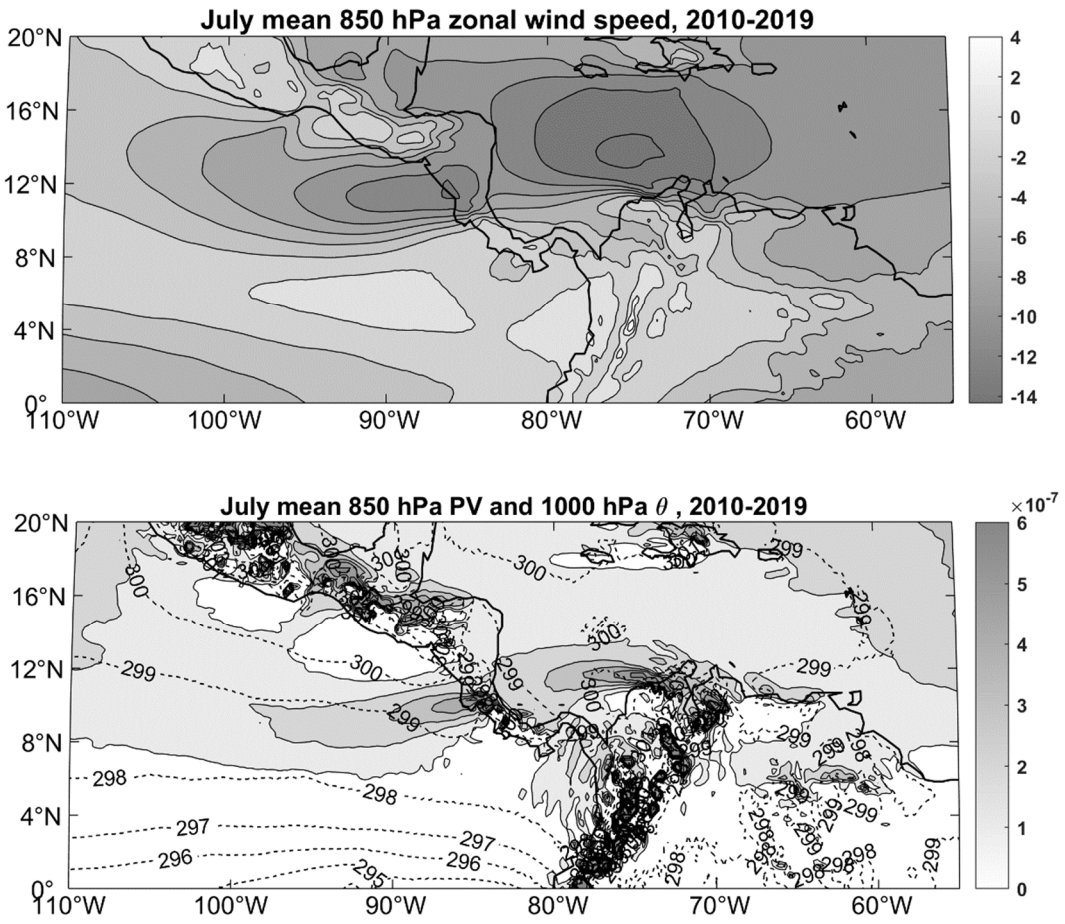

Figure 7.45: July mean 850 hPa zonal wind (ms^{-1}; top), and 850 hPa Ertel potential vorticity ($K\ Kg^{-1}\ m^2\ s^{-1}$; shading) and 1000 hPa potential temperature (K; dashed contours) at bottom. Quantities are from ERA5 reanalyses and have been averaged over 2010-2019.

July-mean zonal winds and potential vorticity at 850 hPa are shown in Figure 7.45 along with 1000 hPa potential temperature. There is a strong low-level easterly jet over the southern Caribbean Sea, reaching peak values north of Venezuela, around 76°W, and a secondary maximum over and west of Nicaragua. These jets are associated with two prominent plumes of high potential vorticity emanating from just west of Lake Maracaibo in Venezuela and from a region near the border between Nicaragua and Costa Rica. Both are regions of large convective rainfall and very high lightning density, suggesting that the high PV plumes may be generated by latent heat release associated with the strong convective storms in those regions. The region near the Catatumbo River, west of Lake Maracaibo, has the highest density of lightning anywhere on the planet (Albrecht, R. I. et al.). The nearly continuous lightning display is known as the "Relámpago del Catatumbo" and has been used as a navigation beacon by fishermen on Lake Maracaibo. The more westerly plume also originates a in a region of high convective rainfall in summer.

While there is hardly any low-level temperature gradient over the Caribbean in summer, there is strong, northward-directed temperature gradient over all of the easterly wave-prone region of

the eastern North Pacific. This is partly owing to the cold water near the equator cause by the climatological equatorial upwelling in that region.

July-mean cross-sections of zonal wind, absolute vorticity, and circulation in the meridional plane, averaged between 70°W and 80°W and averaged between 2010 and 2019, is shown in Figure 7.46.

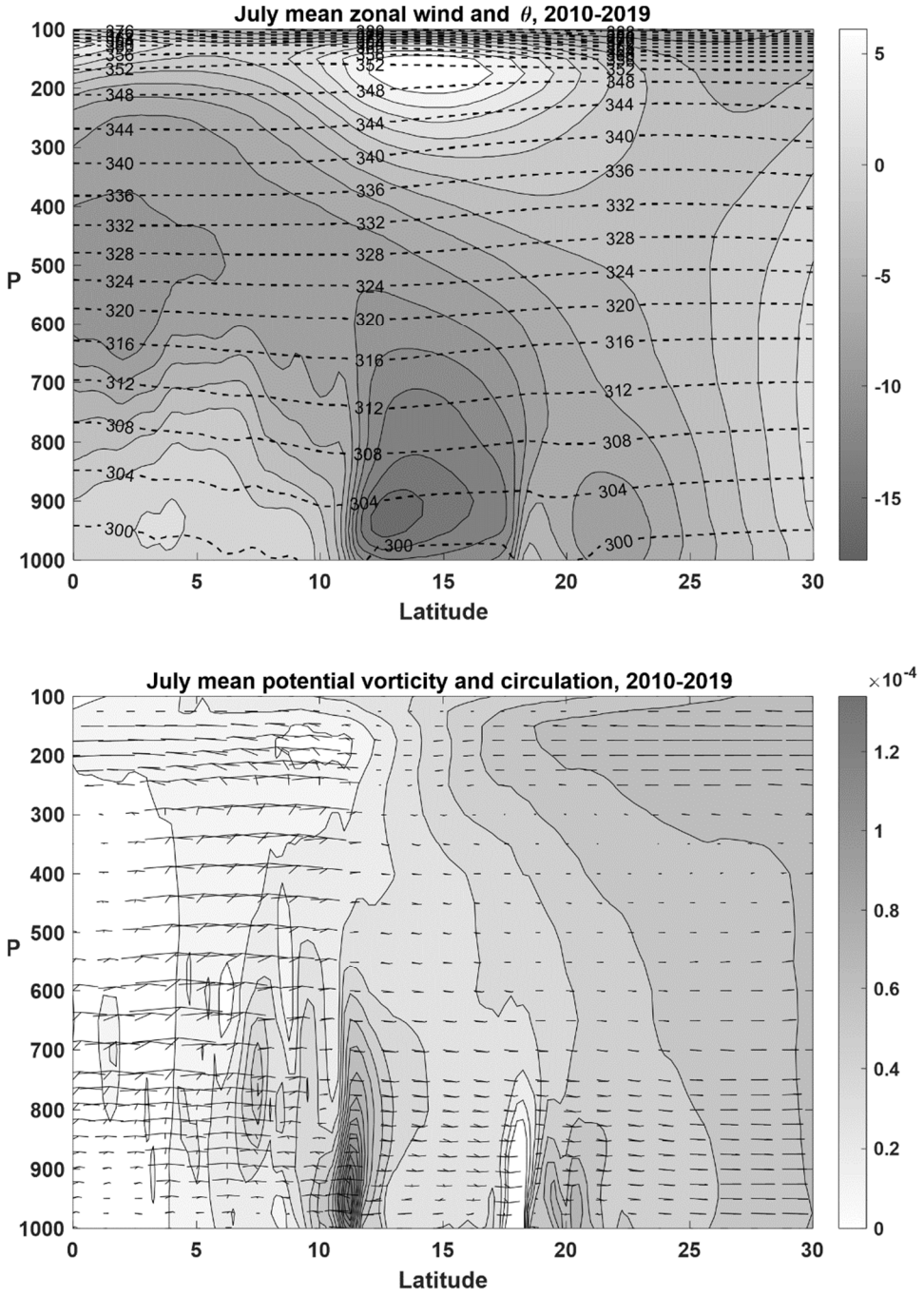

Figure 7.46: Latitude-pressure cross-sections for July mean conditions averaged between 80°W and 70°W and over the period 2010-2019. Top: Zonal wind (ms^{-1}; shading) and potential temperature (K, dashed contours). Bottom: absolute vorticity (s^{-1}; shading) and vectors showing meridional wind and pressure velocity.

(Here we display absolute vorticity rather than PV, since, owing to the high topography of the northern Andes, the PV field is very noisy over the continent.)

The low-level Caribbean Jet is strongly concentrated between the surface and 800 hPa – somewhat lower than the African easterly jet – and its associated cyclonic vorticity is also highly concentrated in latitude, as is also evident in Figure 7.45. There is strong ascent, particularly at high levels, over South America, between 3^{o}N and 10^{o}N; elsewhere, the meridional circulation in this plane is quite weak, but with descending motion in the lower troposphere north of the jet.

From a dynamic standpoint, the two strips of high potential vorticity air in the lower troposphere, evident in Figure 7.45, are highly unstable to internal baroclinic/barotropic instability, owing to the sign reversal of the PV gradient coupled with the strong easterly flow north of the strips. This is very similar to the conditions over central sub-Saharan Africa in summer, except that the jet is much lower and more concentrated in latitude. Indeed, several studies of the energetics of eastern North Pacific easterly waves shows that, initially, they are powered mostly by barotropic conversion of the kinetic energy of the easterly jet into eddy kinetic energy associated with the easterly wave disturbances (e.g. Rydbeck, A.V. and Maloney, E. D. 2014).

The westernmost of the two high PV plumes evident in Figure 7.45 overlies a region of monotonic, northward-directed potential temperature gradient at the surface, thus supporting westward-propagating Eady edge waves at the surface. This is similar to the conditions over the western part of sub-Saharan Africa in summer. At the same time, the decreasing PV north of the PV maximum supports eastward (flow-relative) Rossby waves, and the strong easterlies aloft can Doppler shift those waves to phase lock with the surface Eady edge wave. Thus, in addition to the internal jet instability, can lead to wave growth. This circumstance is quite different from the conditions over the far western North Atlantic, off Africa, where there is little surface air temperature gradient to support Eady edge waves.

As with the AEWs, the dynamics of eastern North Pacific easterly waves is complicated by moist processes, and the very warm sea surface temperatures of the region coupled with low tropopause temperature, favor deep convective clusters whose cold, high clouds can trap infrared radiation and promote self-aggregation of convection. As the disturbances move westward, wind-induced surface fluxes (WISHE) may also begin to contribute to the development of the disturbances as they morph into tropical cyclones.

A case study of particular easterly wave system is displayed in Figures 7.47 – 7.49. Figures 7.47-7.48 show the 850 hPa PV and winds (left columns) and 1000 hPa potential temperatures and winds (right columns). Figure 7.49 shows the Cloud Archive User Data Service (CLAUS) brightness temperatures (10.5-12.5-micron radiances) corresponding to the dates and times in Figures 7.47 – 7.48. Note that the map frame shifts from one date to the next so as to keep the system being analyzed more or less in the center of the domain.

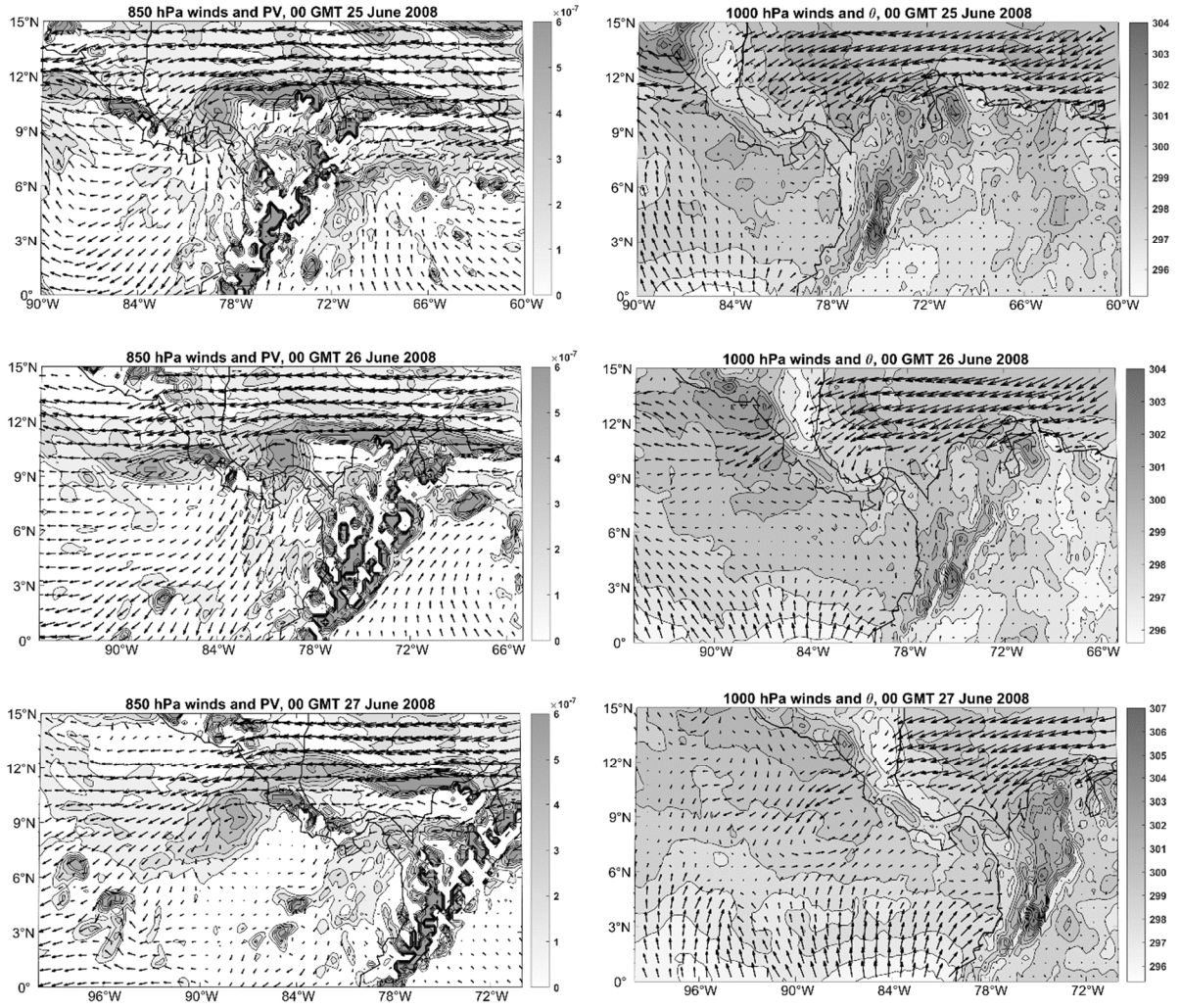

Figure 7.47: 850 hPa winds and potential vorticity (K Kg^{-1} m^2 s^{-1}; left column) and 1000 hPa winds and potential temperature (K; right column) at 00 GMT on June 25 – 27 2008, from ERA5 reanalyses. Note that map frame moves (more or less) with the easterly wave system being analyzed.

On June 25th (top row of Figure 7.47), a thin strip of high PV at 850 hPa is just beginning to roll up at its western end, just north of Panama, accompanied by a strong turning of the flow from easterly to northerly. This is likely a result of the mostly barotropic instability of the Low-Level Caribbean Jet. Note also a second mass of high PV along the Costa Rica-Nicaragua border, around 10ºN, 95ºW. The flow at 1000 hPa is not greatly different from climatology (Figure 7.44).

The roll up of the western end of the PV plume continues on June 26th, while the second plume has stretched westward into the eastern Pacific and is beginning to roll up, with a circulation beginning to develop underneath it at 1000 hPa.

By June 27th, the roll up of the western PV streamer has progressed, with a well-defined maximum near 10ºN, 89ºW, accompanied by a close circulation at 1000 hPa. The surface circulation also has a weak maximum of potential temperature owing to advection by the northerly flow that preceded the system. At this time there is little by way of thick, high clouds associated with the surface circulation on PV aloft (Figure 7.49).

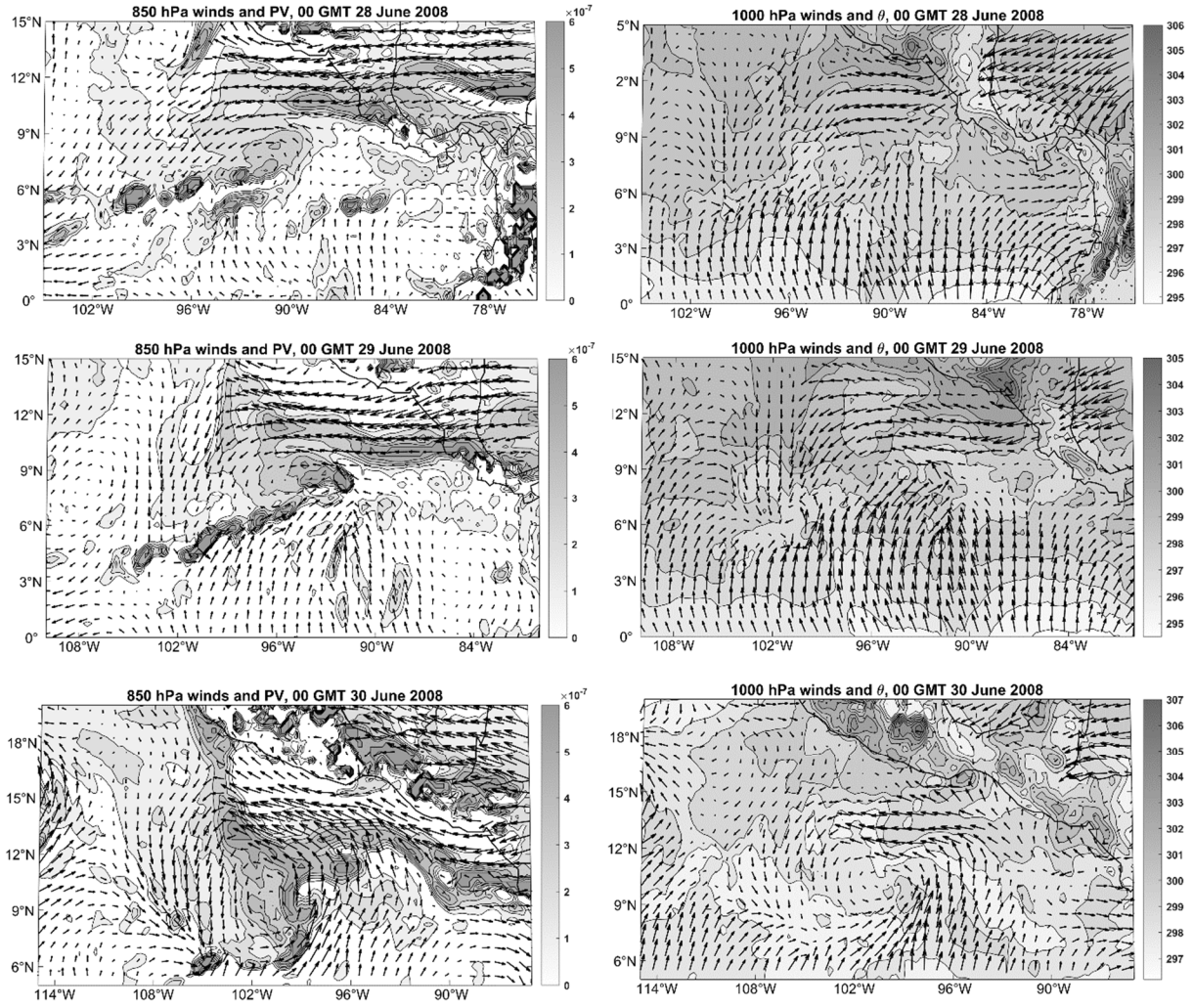

Figure 7.48: 850 hPa winds and potential vorticity (K Kg^{-1} m^2 s^{-1}; left column) and 1000 hPa winds and potential temperature (K; right column) at 00 GMT on June 28 – 30 2008, from ERA5 reanalyses. Note that map frame moves (more or less) with the easterly wave system being analyzed.

On June 28th the system is continuing to develop while moving west-northwestward. It has still not detached from the prominent PV streamer emanating from Central America and it appears to be ingesting high PV air associated with convection along the eastern Pacific ITCZ (high PV blobs west-southwest of the system in the upper left panel of Figure 7.48). The circulation at 1000 hPa is broadening and beginning to interact with the southerly airflow south of the ITZC, and the brightness temperature shows a cluster of thick high cloud co-located with the cyclonic system (Figure 7.49).

During the following two days, June 29th and 20th, the system remains attached to the strong pV streamer emanating from Central America and in fact does not become detached from it until July 2nd (not shown here). The apparent convectively produced, localized masses of high PV air continue to be ingested into the system, which intensifies while its canopy of thick, high cloud expands. This system went on to become Tropical Storm Douglas on July 2nd 2008.

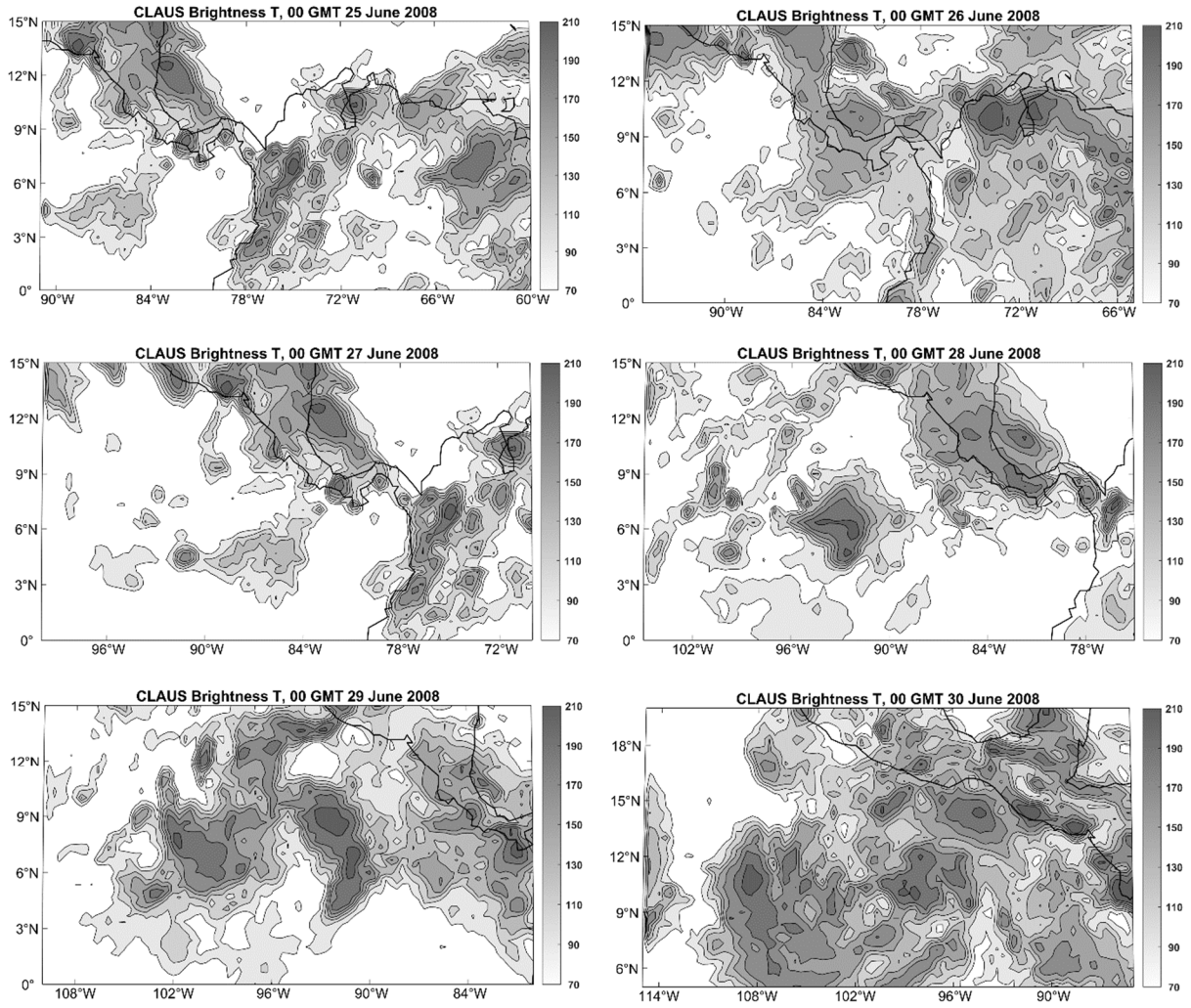

Figure 7.49: Cloud Archive User Data Service (CLAUS) brightness temperature (10.5-12.5-micron radiances) at 00 GMT on June 25 – 30 2008, read from upper left to lower right. Map frames are identical, at each date, to those used in Figures 7.47 – 7.48.

The evolution of this eastern North pacific easterly wave is complex, with two prominent, low-level PV streamers, the surface potential temperature gradient over the eastern Pacific, the ITCZ, and convectively produced PV anomalies all appearing to play some role. As with AEWs, wave dynamics do not appear to be very important after the initial role ups of the PV streamers, although, unlike the case of AEWs, Eady edge wave dynamics may play some role through June 29th. Perhaps more so than in the case of AEWs, diabatic processes seem influential from very early in the development of the disturbances and the relative roles of barotropic/baroclinic instability and diabatic PV generation my depend on the particular phase of low frequency, equatorially trapped disturbances *(*Rydbeck and Maloney E. D. 2014*)*.

The physics underlying intraseasonal and synoptic-scale variability in the tropics remains a fascinating and consequential research topic, drawing on processes peculiar to the tropics as well as variants on classical, mid-latitude dynamics.

References

Albrecht, R. I., Goodman, S. J., Buechler, D. E., Blakeslee, R. J., and Chistian, H. J., Where Are the Lightning Hotspots on Earth? *Bull Amer Meteor Soc*, **97**, 2051–2068.

Bony, S., and K. Emanuel, 2005: On the role of moist processes in tropical intraseasonal variability: cloud-radiation and moisture-convection feedbacks. *J Atmos Sci*, **62**, 2770–2789.

Brian Hoskins and Ian James, 2014: *Fluid Dynamics of the Mid-Latitude Atmosphere*. Wiley-Blackwell, 432 pp.

Charney, J. G., 1947: The dynamics of long waves in a westerly baroclinic current. *J Meteor*, **4**, 135–163.

——, and M. E. Stern, 1962: On the Stability of Internal Baroclinic Jets in a Rotating Atmosphere. *J. Atmospheric Sci.*, **19**, 159–172, https://doi.org/10.1175/1520-0469(1962)019<0159:otsoib>2.0.co;2.

Chavas, D. R., and K. A. Reed, 2019: Dynamical Aquaplanet Experiments with Uniform Thermal Forcing: System Dynamics and Implications for Tropical Cyclone Genesis and Size. *J. Atmospheric Sci.*, **76**, 2257–2274, https://doi.org/10.1175/JAS-D-19-0001.1.

Dominguez, C., J. M. Done, and C. L. Bruyère, 2020: Easterly wave contributions to seasonal rainfall over the tropical Americas in observations and a regional climate model. *Clim. Dyn.*, **54**, 191–209, https://doi.org/10.1007/s00382-019-04996-7.

Eady, E. T., 1949: Long waves and cyclone waves. *Tellus*, **1**, 33–52.

Farrell, B., 1984: Modal and Non-Modal Baroclinic Waves. *J. Atmospheric Sci.*, **41**, 668–673, https://doi.org/10.1175/1520-0469(1984)041<0668:MANMBW>2.0.CO;2.

Fjørtoft, R., 1950: Application of integral theorems in deriving criteria of stability for laminar flows and for the baroclinic circular vortex. *Geofys Publ*, **17**, 1–52.

Hayashi, Y., 1982: Space-time spectral analysis and its applications to atmospheric waves. *J. Meteorol. Soc. Jpn. Ser II*, **60**, 156–171, https://doi.org/10.2151/jmsj1965.60.1_156.

Hoskins, B. J., M. E. McIntyre, and A. W. Robertson, 1985: On the use and significance of isentropic potential vorticity maps. *Quart J Roy Meteor Soc*, **111**, 877–946.

Hung, M.-P., J.-L. Lin, W. Wang, D. Kim, T. Shinoda, and S. J. Weaver, 2013: MJO and Convectively Coupled Equatorial Waves Simulated by CMIP5 Climate Models. *J. Clim.*, **26**, 6185–6214, https://doi.org/10.1175/JCLI-D-12-00541.1.

Khairoutdinov, M. F., and D. A. Randall, 2003: Cloud resolving modeling of the ARM summer 1997 IOP: Model formulation, results, uncertainties and sensitivities. *J Atmos Sci*, **60**, 607–625.

Khairoutdinov, M. F., and K. Emanuel, 2018: Intraseasonal Variability in a Cloud-Permitting Near-Global Equatorial Aquaplanet Model. *J. Atmospheric Sci.*, **75**, 4337–4355, https://doi.org/10.1175/jas-d-18-0152.1.

Kiladis, G. N., C. D. Thorncroft, and N. M. J. Hall, 2006: Three-Dimensional Structure and Dynamics of African Easterly Waves. Part I: Observations. *J. Atmospheric Sci.*, **63**, 2212–2230, https://doi.org/10.1175/JAS3741.1.

——, M. C. Wheeler, P. T. Haertel, K. H. Straub, and P. E. Roundy, 2009: Convectively coupled equatorial waves. *Rev. Geophys.*, **47**, https://doi.org/10.1029/2008RG000266.

Kuang, Z., 2008: A Moisture-Stratiform Instability for Convectively Coupled Waves. *J. Atmospheric Sci.*, **65**, 834–854, https://doi.org/10.1175/2007JAS2444.1.

Madden, R., and P. R. Julian, 1971: Detection of a 40-50 day oscillation in the zonal wind in the tropical Pacific. *J Atmos Sci*, **28**, 702–708.

——, and ——, 1972: Description of global circulation cells in the tropics with a 40-50 day period. *J Atmos Sci*, **29**, 1109–1123.

Mapes, B. E., 2000: Convective inhibition, subgrid-scale triggering energy, and stratiform instability in a toy tropical wave model. *J Atmos Sci*, **57**, 1515–1535.

Rydbeck, A.V. and Maloney, E. D., 2014: Energetics of East Pacific Easterly Waves during Intraseasonal Events. *J Clim*, **27**, 7603–7621.

Wheeler, M., and G. N. Kiladis, 1999: Convectively coupled equatorial waves: Analysis of clouds and temperature in the wavenumber-frequency domain. *J Atmos Sci*, **56**, 374–399.

Wheeler, M., G. N. Kiladis, and P. J. Webster, 2000: Large-scale dynamical fields associated with convectively coupled equatorial waves. *J Atmos Sci*, **57**, 613–640.

Yano, J.-I., and K. A. Emanuel, 1991: An improved WISHE model of the equatorial atmosphere and its coupling with the stratosphere. *J Atmos Sci*, **48**, 377-389.